Size-dependent photochemistry of NO dimers adsorbed on alumina supported silver nanoparticles

Im Fachbereich Physik der Freien Universitäte Berlin eingereichte
Dissertation zur Erlangung des Akademischen Grades
DOKTOR RERUM NATURALIUM (Dr. rer. nat)

MAX-PLANCK-GESELLSCHAFT

Freie Universität Berlin

Daniel Mulugeta, M.Sc

May 2010

This work was done between March 2006 and May 2010 at the Chemical Physics Department of the Fritz-Haber-Institute of Max-Planck Society under the supervision of Professor Hans-Joachim Freund.

Berlin, May 2010

Erster Gutachter (Betreuer): Prof. Dr. Hans-Joachim Freund
Fritz-Haber-Institut der Max-Planck-Gesellschaft

Zweiter Gutachter: Prof. Dr. Martin Wolf
Freie Universität Berlin
Fritz-Haber-Institut der Max-Planck-Gesellschaft

Tag der mündlichen Prüfung: July 7, 2010

Abstract

This work presents detailed quantitative results on the influences of particle size and photon energy, including that of plasmon excitation, on a photochemical process at nanoparticle surfaces. As a test system NO dimer layers on alumina supported Ag nanoparticles (diameters 3 to 12 nm) are used. Mass selected time of flight (MS-TOF), resonance enhanced multiphoton ionization (REMPI) and temperature programmed desorption (TPD) techniques are used as methods. NO molecules dosed on silver surfaces at low temperatures (below 77 K) form dimers. Upon heating NO dimers dissociate into NO monomers or react to form N_2O and O. It is shown that the TPD peak temperatures for desorption arising from these reactions decrease with decreasing mean size of the Ag NPs and show a simple linear scaling law with (1/R).

Photodesorption cross sections (PCS) of NO from NO dimer-covered Ag NP surfaces also show significant size dependences. At 2.3 and 4.7 eV, the PCS increase with *1/R* from the value at Ag (111). This 1/R scaling is attributed to the increasing number of collisions of hot electrons that excite the adsorbates, as the surface to volume ratio (S/V) is proportional to *1/R*. At 3.5 eV in *p*-polarization, (*on-plasmon resonance*) the PCS increase more steeply and reach a maximum of $\sim 1.7 \times 10^{-16}$ cm^2 (~43 times enhancement compared to Ag (111)) at an Ag NP mean diameter of *D* ~ 5 nm, followed by a sharp decrease. The peaked behavior is attributable to the interplay of the size-dependences of the plasmon decay channels and the plasmon oscillator strength.

The desorbed molecules have nonthermal amounts of energy in rotational, vibrational and translational motion. The rotational and translational excitations are positively correlated while the vibrational excitation is strongly decoupled from them. The translational and internal energies of NO photodesorbed from Ag NPs are almost constant for all the investigated particle sizes at 2.3 and 3.5 eV in *p*-polarization. This suggests that the photodesorption *dynamics* of NO is not sensitive to the particle size even at the plasmon excitation at 3.5 eV. The desorption proceeds via substrate hot electron attachment to the adsorbate resonance state which forms a transient negative ion (TNI). However, at 4.7 eV an increase of the translational and internal energies of the photodesorbed NO molecules was observed at smaller Ag NPs. This extraordinary effect is explained by a proposed new mechanism: via formation of hot holes in the adsorbate (transient positive ion (TPI)) either by excitation of *d*-band holes at the Ag NP surface which subsequently are transferred to an adsorbate orbital or by direct charge transfer (CT) excitation from the adsorbate into the empty *s-p* orbitals of Ag NPs above the Fermi level. One possible reason why this mechanism results in more energetic desorbates is that the cations formed by hot hole attachment (TPI mechanism) are smaller than the anions formed by the TNI mechanism. Therefore, cations can approach the surface closer and with higher velocity and then rebounce with a higher energy. The emergence of this new channel for small particles is likely connected with the relative increase of surface atoms/adsorbate molecules with decreasing particle size.

Deutsche Kurzfassung

Diese Arbeit präsentiert detaillierte quantitative Ergebnisse zu den Einflüssen von Partikelgröße und Photonenergie, einschließlich der Plasmonenanregung, auf einen photochemischen Prozess auf Nanopartikeln. Als Testsystem dienen NO Dimer-Schichten auf Silber-Nanopartikeln (Durchmessern 3 bis 12 nm) die auf einen dünnen Aluminiumoxid-Film auf NiAl (110) aufgebracht sind. Verwendete Methoden sind Massenselektive Flugzeitmessungen (MS-TOF), resonanzverstärkte Multiphotonen-Ionisationsspektroskopie (REMPI) und Temperatur-programmierte Desorptions (TPD). NO Moleküle, die bei tiefen Temperaturen unterhalb von 77 K auf Silber-Oberflächen aufgebracht werden, bilden Dimere. Werden sie geheizt, dissoziieren NO Dimere in NO Monomere oder reagieren zu N_2O und O. Es wird gezeigt, dass die Temperaturmaxima der diesen Reaktionen entsprechenden TPD-Signale abnehmen wenn man die mittlere Größe der Ag Nanopartikel verringert, und ein einfaches lineares Skalierungsgesetz (1/R) befolgen.

Photodesorptionsquerschnitte (PCS) für NO von NO dimer-bedeckten Ag Nanopartikel-Oberflächen zeigen ebenfalls eine signifikante Größenabhängigkeit. Bei 2,3 und 4,7 eV steigen die PCS mit 1/R an ausgehend vom Wert für Ag (111). Dieses 1/R-Verhalten wird der zunehmenden Zahl von Kollisionen heißer Elektronen zugeschrieben, die die Adsorbate anregen können, da das Verhältnis von Oberfläche zu Volumen (S/V) proportional zu 1/R ist. Bei 3,5 eV in p-Polarisation (*bei Plasmonenresonanz*) steigen die PCS steiler und erreichen ein Maximum von $\approx 1{,}7 \times 10^{-16}$ cm^2 (≈ 43 fache Verstärkung verglichen mit Ag (111)) bei einem mittlerem Ag Nanopartikel-Durchmesser von $D \sim 5$ nm, gefolgt von einem scharfen Abfall. Dieses Extremalverhalten kann dem Wechselspiel der Größenabhängigkeiten der Kanäle für Plasmonenzerfall und der Plasmonen-Oszillatorstärke zugeschrieben werden.

Die desorbierten Moleküle haben nicht-thermische Energieverteilungen in Rotations-, Vibrations- und Translationsfreiheitsgraden. Während Rotations- und Translationsanregungen positiv korreliert sind, ist die Vibrationsanregung von diesen entkoppelt. Sowohl die Translationsenergien als auch die inneren Energien von NO waren für alle untersuchten Partikelgrößen bei 2,3 und 3,5 eV in p-Polarisation fast konstant. Dies legt nahe, dass die *Dynamik* der Photodesorption von NO nicht sensitiv auf die Partikelgröße ist, sogar bei Plasmonenanregung bei 3,5 eV. Die Desorption verläuft über den Einfang heißer Substratelektronen durch den Resonanzzustand des Adsorbats, was zu einem transienten negativen Ion (TNI) führt. Nur bei 4,7 eV wurde bei kleineren Ag Nanopartikeln ein Anwachsen der Translationsenergien und der inneren Energien der photodesorbierten NO Moleküle beobachtet. Dieser außergewöhnliche Effekt wird durch einen neu vorgeschlagenen Mechanismus erklärt nämlich über die Bildung heißer Löcher im Adsorbat (transiente positive Ionen (TPI)) entweder durch die Anregung von d-Band Löchern an der Oberfläche der Ag Nanopartikel mit folgendem Ubertrag auf ein Adsorbat-Orbital, oder durch eine direkte Ladungstransfer-Anregung aus dem Adsorbat in die leeren s-p-Orbitale der Ag Nanopartikel oberhalb des Ferminiveaus. Das Auftauchen diese neuen Kanals ist vermutlich mit der relativen Zunahme der Oberflächeatome/Adsorbatmoleküle mit abnehmender Teilchengröße zu erklären.

Table of content

Frequently used abbreviations

°C	Degrees centigrade
1/R	Inverse of the mean particle radius (= 2/*D*)
2PPE	Two-photon photoemission
AES	Auger electron spectroscopy
cw	Continuous wave
D	Nanoparticle mean diameter
DIET	Desorption induced by electronic transitions
DIMET	Desorption induced by multiple electronic transitions
DOF	Degrees of freedom
E_{des}	Desorption activation energy (adsorption energy)
F	Laser fluence
fs	Femtosecond (= 10^{-15} second)
FWHM	Full width at half maximum
HOMO	Highest occupied molecular orbital
HOPG	Highly ordered pyrolytic graphite
hv	Photon energy
IRAS	Infrared reflection absorption spectroscopy
K	Kelvin
KDP	Potassium dideuterium phosphate
LEED	Low energy electron diffraction
LITD	Laser induced thermal desorption
LUMO	Lowest unoccupied molecular orbital
MCP	Multichannel plate
MGR	Menzel-Gomer-Redhead
MNPs	Metal Nanoparticles

MS-TOF	Mass-selected time-of-flight
Nd-YAG	Neodym-doped yttrium-aluminum-garnet
nm	Nano meter (= 10^{-9} meter)
NP (NPs)	Nanoparticle (Nanoparticles)
ns	Nanosecond (= 10^{-9} second)
PCS	Photodesorption cross section
PES	Potential energy surface
PID	Photon induced desorption (Photoinduced desorption)
QMS	Quadrupole mass spectrometer
QMS-TOF	Quadrupole mass spectrometer time-of-flight
REMPI	Resonance enhanced multiphoton ionization
SMB	*Shifted* Maxwell-Boltzmann
STM	Scanning tunneling microscopy
T_{el}	Electron temperature
TNI	Transient negative ion
T_p	Desorption peak temperature
TPD	Temperature programmed desorption
TPI	Transient positive ion
T_{rot}	Rotational temperature
T_t	Translational temperature
T_{vib}	Vibrational temperature
UHV	Ultrahigh vacuum
UV	Ultraviolet
$\mathbf{v}$	Velocity
v	Vibrational level

Chapter 1

I. Introduction and motivation

Surface photochemistry is the basis of a wide variety of extremely important technological processes and applications. Therefore, developing a fundamental understanding of such processes presents opportunities for further exploitation in applications. The primary focuses of many researches are in understanding and controlling of elementary steps in the photo-induced processes of adsorbates in a well defined and controlled manner. For this purpose the use of lasers provides many advantages to initiate reactions as well as to detect the product molecules. A single photon of well defined energy absorbed by the adsorbate or the substrate can impart part or all of its energy to break the adsorbate substrate bond or the intermolecular bond. Hence by varying its energy, polarization, fluence and/or pulse duration, it can be possible to control the reaction efficiency, and excitation of the different degrees of freedom of the desorbate. State selective detection of the product molecules in terms of the various possible quantum states can give a wealth of information about the microscopic forces that lead to desorption or reaction. The presence of the surface acts as not only in arranging the molecules and modifying their electronic structure but also as source for selective excitation and relaxation channels for the excited molecules. Therefore, in surface photochemistry the surface plays a crucial role as it dictates different excitation and relaxation mechanisms.

Flat surfaces can be used as a useful reference however, they may not be ideal for practical applications of surface photochemistry as in heterogeneous catalysis. In such cases, nanostructures such as nanoparticles or thin films can provide many advantages which can not be found on flat surfaces. Therefore, understanding the chemical processes occurring on the NP surfaces and the correlation with their size could lead to an improved efficiency and performance in application. The surface chemistry on MNPs can be greatly different from that of the bulk materials. This is not only because NPs provide more surface area for reaction, but they can exhibit unique optical, electronic and catalytic properties. Especially the excitation of plasmons on MNPs may have a huge effect on the photochemistry of adsorbates on their surfaces. Plasmons are collective excitations of the metal electrons, which resonantly enhance the electric field at the surface. To study effects of plasmons, Ag NPs are an ideal candidate since their plasmon resonance energy is well separated from the intraband transition (*d* – *sp* transition).

Although much progress has been made with respect to the understanding of the optical and electronic properties of MNPs, the detailed knowledge regarding the photochemistry on their surfaces is rare. To date there have been only few investigations that address the effect of size and/or plasmon excitation on the photochemistry of adsorbates on MNP surfaces [Wat06 and ref. therein]. The work in this thesis is dedicated to investigate the effects of particle size, and photon energy, including the plasmon excitation on the photodesorption of NO from adsorbed NO dimers on Ag NPs. Results measured from single crystal Ag surface are also presented as a reference. Ag NPs of uniform density (diameter, *D,* between 3 and 12 nm) were grown by deposition of Ag atoms on alumina film on a NiAl (110) substrate at room temperature. Particular advantages of this system are that their preparation is well established, and that their optical, and electronic properties (in the size range we are interested in) are well characterized by the photon STM [Nil00], and two-photon photoemission [Eve05] measurements. These methods show their (1,0) mode Mie resonance excitation at ~3.6 eV. As an adsorbate NO is chosen which is commonly used in photochemistry studies especially because it is easy for state resolved measurements.

This thesis is organized as follows. It is divided into 6 chapters. The first chapter presents a general introduction about the properties of MNPs and photochemistry in general. In *Chapter 2* the technical aspects of various methods used in this thesis such as temperature programmed desorption (TPD), time-of-flight (TOF) mass spectrometry, and resonance-enhanced multiphoton ionization (REMPI), will be described. In addition, the measurement procedures, and data acquisition and analysis methods will be presented. *Chapter 3* deals with size effects on the adsorption and subsequent thermal and photo-induced reactions of NO on Ag NPs. In photodesorption experiments in addition to size effects, effects of photon energy, including plasmon excitation at 3.5 eV in *p*-polarization, on the desorption cross section of NO are investigated. *Chapter 4* reports the effects of particle size on the dynamics of NO desorption from Ag NP surfaces at $h\nu$ = 2.3, 3.5, and 4.7 eV nanosecond (ns) laser pulses. In these studies final state energy (translational and internal energy) distributions of photodesorbed NO molecules are measured and the possible mechanisms are discussed. *Chapter 5* focuses on femtosecond laser induced desorption dynamics of NO from NO dimer-covered Ag NPs and Ag (111) surfaces. In *Chapter 6* a short summary of the thesis will be presented.

II. Basic concepts

In this chapter the basic concepts and models which are relevant for the general understanding of the next chapters are presented. In the first section an overview about the properties of metal surfaces with the main emphasis on MNPs, will be presented. In the second and third sections the adsorption and photoreaction of adsorbates and the dynamics of photoinduced processes will be presented.

1.1. The substrate

In surface photochemistry, the substrate plays a major role. Unlike to gas phase chemistry, surface chemistry paves many ways for selective reactions. The presence of the surface is responsible for a wide range of physical and chemical phenomena, including excitation, relaxation, desorption and reactions. Therefore understanding the properties of the substrate is crucial to understand the adsorption and reactions of adsorbates on the surfaces. As the main topic in this thesis work is photochemistry on MNPs, understanding of the physical and chemical properties of the MNPs is important and will be presented in the first section of this chapter.

1.1.1. Metal nanoparticles (MNPs)

Metal nanoparticles have attracted great attention due to their potential to modulate physical and chemical properties [Rao02, Kre95]. Since size plays an important role in determining their physical and chemical properties, one of the most important things is studying these properties as a function of size. Here we will focus on those properties which are relevant for photochemistry.

i. Plasmon excitations in MNPs

One field of research which has attracted a lot of attention in the last decades is that of the optical properties of small MNPs, which are dominated by the so-called surface plasmon resonance [Kre95, Mai07]. The surface plasmon resonance is described as the coherent motion of conduction band electrons caused by the interaction with an external electromagnetic field. In a classical picture, the electric field of an incoming light wave induces a polarization of the electrons with respect to the ionic core of the NP. Ultimately, this polarization drives all the electrons to follow a dipole oscillation with the same phase. [Hil01, Kel03, Neg08].

The interaction of light with small spherical metal particles was initially studied by Faraday and theoretically explained by Gustav Mie in 1908 by solving the Maxwell equations. For this reason, the surface plasmon resonance in small metal particles is sometimes called Mie plasmon. The surface resonance of MNPs, ω_{res}, can be generally described by:

$$\omega_{res} = \frac{\omega_p}{\sqrt{\varepsilon_m + \varepsilon_1}}, \tag{1.1}$$

where ω_p is the bulk plasmon resonance, ε_m is the dielectric constant of the surrounding and ε_1 the dielectric constant of the metal.

The Mie theory resulted in a serious of multipole oscillations of extinction and scattering cross sections. For spherical particles (R << λ) of volume V_0, only dipole oscillation contributes and the Mie theory reduces to the expression:

$$\sigma_{ext} = 9\frac{\omega}{c}\varepsilon_m^{3/2}V_0\frac{\varepsilon_2(\omega)}{[\varepsilon_1(\omega)+2\varepsilon_m]^2+\varepsilon_2(\omega)^2}.,\tag{1.2}$$

where ω is the angular frequency of the incident light, and c is the speed of light. ε_m and $\varepsilon_1(\omega) + i\varepsilon_2(\omega)$ are the dielectric functions of the surrounding medium and the metal, respectively. For negligible damping $\left(\varepsilon_2(\omega), \frac{\partial\varepsilon_2}{\partial\omega} << 1,\right)$ the resonance occurs when the Froehlich condition $\varepsilon_1(\omega) = -2\varepsilon_m$ is met [Kre95].

Equation (1.2) is independent of the particle size. However, experimental studies show that plasmon oscillations are size dependent. Therefore, the size dependence of the plasmon oscillations is introduced into Mie's theory through modification of the material's dielectric function. This modification is introduced through a classical approach since electron-surface scattering must be enhanced in small particles (due to electron confinement).

$$\varepsilon_2 = \varepsilon_2^{bulk} + 2g \cdot v_f / D \tag{1.3}$$

Where v_f is the Fermi velocity of electrons, D is the particle diameter and the dimensionless size parameter g accounts for additional surface damping terms

The plasmon frequency of alkali MNPs, like K, Li exhibits a red shift with $N^{-1/3}$ due to the surface effects that weaken the plasmon oscillation. For noble metals like Ag, Cu or Au, which have completely filled *d* shell, the plasmon frequency is influenced by the core (the *d* electrons) polarization. Therefore, the plasmon frequency of noble MNPs show a blue shift with $N^{-1/3}$ (see a particular example Ag NPs/Al_2O_3/NiAl (110) in *Chapter 3*, figure 3.1). In metals like Hg, the surface effects and the core polarization counterbalance each other and there is no size dependence change of the plasmon frequency [Lie93, Rei04, Tig93].

For non-spherical MNPs, the single plasmon resonance absorption band of spherical MNPs splits into two ((1,0) and (1,1)) modes. The two modes can be excited with different relative strengths depending on the angle of incidence and the polarization of the incoming photons. The schematic view of such a splitting is shown in figure 1.1a). The absorption band at higher energy is caused by the oscillation of electrons perpendicular to the major axis (transversal plasmon), while the oscillation of electrons along the major axis (longitudinal plasmon) results to the lower energy absorption band. For a free NP, both the (1,1) and (1,0) mode of Mie resonance can be seen. However, when the nanoparticles are deposited on a conducting material there will be an electromagnetic coupling between the nanoparticle’s field and the substrate underneath that induces an image dipole which can couple destructively with the (1,1) mode and constructively with the (1,0) mode Mie plasmon resonance of NPs (see figure 1.2).

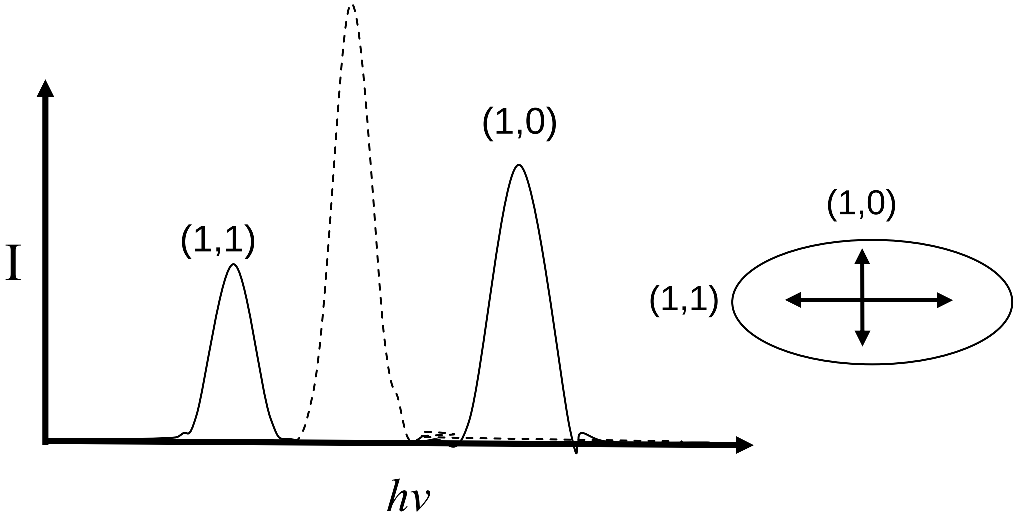

Figure 1.1.: Illustration of the absorption band of a spherical (dashed line) and non-spherical (solid line) NP. The single absorption band of the spherical NP is split into two modes, (1,1) and (1,0), for an oblate ellipsoid NP.

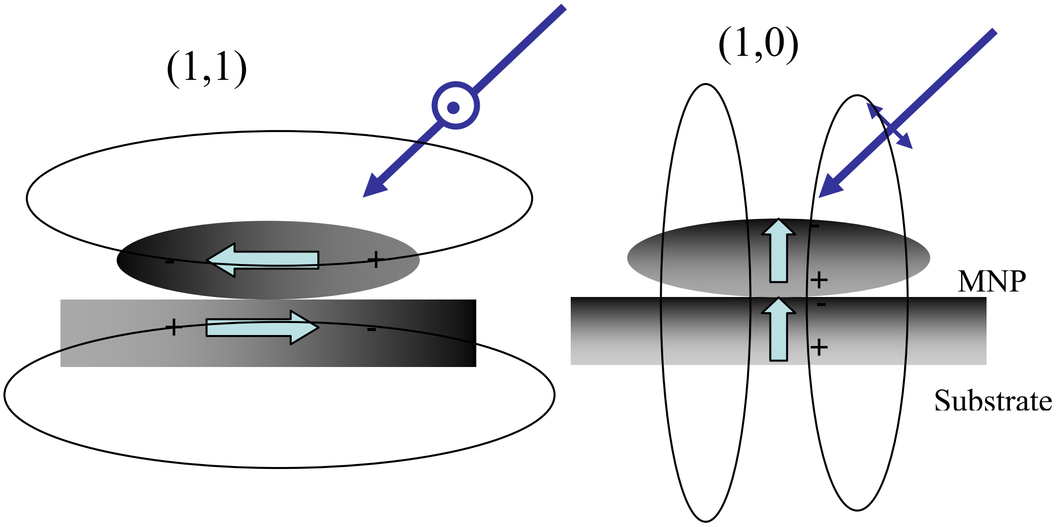

Figure 1.2.: Schematic view showing an electromagnetic interaction between the NP plasmon field and the induced image dipole of the conducting substrate. The (1,1) mode which can be excited by s-polarized light couples destructively, while the (1,0) mode which can be excited by *p*-polarized light couples constructively with the image dipole.

Surface plasmon excitation is accompanied by a pronounced enhancement of the electromagnetic field near the surface [Kre95, Kla98]. The field enhancement has been used in applications and is the base of many surface-enhanced spectroscopies and for photochemistry [Sti99, Kre95].

The lifetime of the plasmon is very short, in the order of fs. In this ultrashort time the plasmon decays in different ways depending on the size of the NPs [Sti00, Mol02, Mol03, Kre95, Bos02, Cha98, Gui04].

1) *Landau damping* – this is the decay of the plasmon into electron-hole pairs. Landau damping is dominant for small NPs.
2) *Radiation damping* – In the large NP size limit the plasmon resonance mainly decays into an external radiation field.
3) *Surface scattering* – when the size of the NP becomes smaller the coherent oscillation of plasmon electrons can be inelastically scattered at the surface. Such scattering strongly depends on the size of the NP.
4) *Chemical interface damping* - In this plasmon damping mechanism, the electrons lose their coherent motion due to dynamical tunneling into and out of an adsorbate or surface state [Hen03].

Furthermore, for very small MNPs the spill-out of conduction electrons decreases the density of conduction electrons which can decrease the plasmon frequency and strength.

ii. Electronic properties of MNPs

The energy levels, transport properties, and dynamics of excited electrons on metal surfaces [Aes96, Aes00, Chu06, Ken06, Bau02, Bau04, Bau05, Mer03, Mus06, Sei91, Wer89, Vij02] are important in surface chemistry. In MNPs these properties play a key role in many applications due to the possibility of tuning their behavior by changing the size.

Reducing the size of the nanoparticles has a pronounced effect on the energy level spacing [Hal86, Aiy94, Bau99]. In metals, due to the high density of energy levels of ~10^{23} cm^{-3}, such separation of energy levels is only observed at very small NPs (made of about 100 atoms or less). In addition, the density of states near the Fermi surface and the binding energy of the core levels usually shows a significant change with size. For example, XPS spectra from Ag and Pd clusters show a narrowing and positive shift of the *d*-band spectra with decreasing the NP size, which was explained based on final state effects [Hov01, Hov04, Bal07].

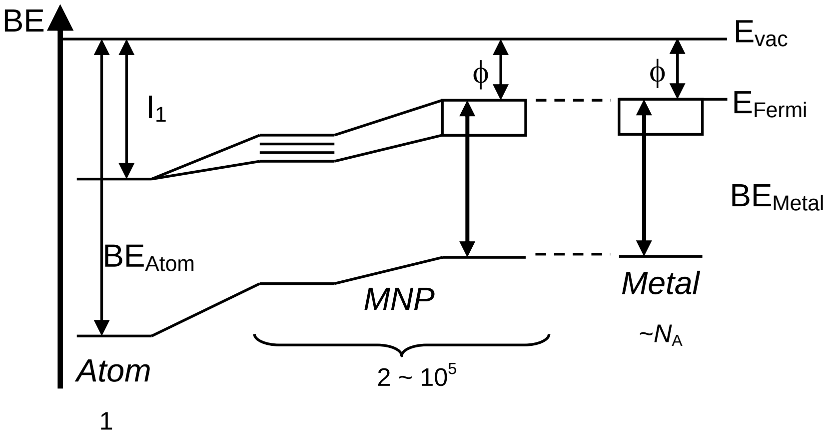

Figure 1.3.: Schematic illustration showing the evolution of the electronic band of a bulk metal from the orbitals of a single metal atom (after [Bau99]).

Another important size-dependent property of MNPs is the electron dynamics [Hal99, Fau96]. Understanding the dynamics of the hot electrons produced in the metal substrate by incoming photons is crucial since these electrons are responsible for the underlying photochemistry. Hot electrons excited by the incoming photons can decay in different ways with different time scale [Pet97, Ech00, Ech04]. The lifetime of hot electrons or hot holes in a free electron gas can be approximately derived from Landau's Fermi liquid theory:

$$\tau_{ee} = \tau_0 \frac{E_F^2}{(E - E_F)^2} \tag{1.4}$$

where E is the initial excitation energy, E_F is the Fermi energy, and the prefactor τ_0 is determined by the free electron density and approximately given by $\tau_0 = \frac{64}{\sqrt{3} \cdot \pi^{5/2}} \cdot \sqrt{\frac{m}{ne^2}}$,

In addition to the initial excitation photon energy (which is contained in equation 1.4), the lifetime of hot electrons depends also on the size of the MNPs. Time resolved fs experiments show a strong decrease of electron-electron and electron-phonon interaction for smaller MNPs, $D < 10$ nm [Arb03, Voi00, Del99, Voi01, Voi04] which was explained due to the confinement of both electrons and phonons in the nanoparticle scale. In addition, in noble metals the change of *s-d* screening is suggested to enhance the lifetime of hot electrons near the surface [Aes96, Aes00, Bas01, Gar03]. Moreover the dynamics of excited electrons depends on the available phase space above the Fermi level [Paw97].

In fs laser excitations, the photon energy is deposited into the electron system, and due to the small heat capacity of the electrons (compared to the lattice), the electron temperature, T_{el}, rises within the pulse width to high values. This results in a much slower increase of the phonon temperature (T_{ph}) compared to the electronic response [Mis95, Fri06]. The degree of excitation can be characterized by the two temperatures which are expressed in the so called *two temperature model* that states that T_{el} and T_{ph} evolve according to:

$$
\begin{aligned}
&C_{el}(T_{el})\frac{\partial T_e}{\partial t} = \kappa(T_{el})\frac{\partial^2 T_{el}}{\partial x^2} - g(T_{el} - T_{ph}) + A(x,t) \\
&C_{ph}(T_{ph})\frac{\partial T_{ph}}{\partial t} = g(T_{el} - T_{ph}),
\end{aligned}
\tag{1.5}
$$

where $A(x,t)$ is the energy deposited by the laser, C_{el} and C_{ph} are the heat capacities of the electrons and the lattice, respectively, and the constant g determines how quickly the electrons and phonons equilibrate with each other.

iii. Surface morphology / structure of MNPs

When the size of materials goes down to the nanometer scale, surface effects become dominant, and their morphologies may also change along with the size change [Lin07, Hen92]. Since the surface is very important for very small nanoparticles it is important to know the details of the surface morphology and structure in order to understand their interaction with the environment, for example with adsorbates. Unlike to single crystal surfaces, in metal nanoparticles different structures such as crystalline facets, edges, boundaries, etc can be simultaneously present [Cam97]. Thus, understanding the size-dependent morphology and the related property change is of great importance to understand the chemistry on their surfaces. For example, both the reactivity and selectivity of a nanocatalyst can be tailored by controlling the shape, as shape determines the number of atoms located at the edges or corners [Nar04].

1.2. Adsorption of reactant

In general there are two classes of adsorption of molecules on a surface; physisorption and chemisorptions. In physisorption the molecules are weakly bound to the surface mainly through van der Waals type interactions. There is a very small perturbation of the adsorbate and hence physisorbed molecules essentially retain their gas phase properties.

In contrast to physisorption, chemisorption involves significant interaction between the adsorbate and the substrate and therefore their properties are perturbed due to hybridization. In transition metals, the *d*-band is usually involved in the bonding. One of the most widely used models for molecular adsorption on transition metal surfaces is the *d*-band model of Hammer and Nørskov [Ham96] which relates the chemisorption energy to the position of the metallic *d*-band relative to the molecular orbitals of the adsorbate and to the coupling matrix elements and overlap integrals between the metal *d*-states and adsorbate states. Since the *d*-band is narrower than the *sp*-band, its interaction with the adsorbate can result in a splitting into bonding and anti-bonding states. This approach introduces a hybridization energy E_{d-hyb} for a weak coupling V_{ad} between the adsorbate states and the *d*-band of the metallic surface:

$$E_{d-hyb} = -\sum_a C(F_a, F_d)\frac{V_{ad}^2}{|\varepsilon_a - \varepsilon_d|} + D(F_a, F_d)\alpha S_a V_{ad}\ , \tag{1.6}$$

where $C(F_a, F_d)$ and $D(F_a, F_d)$ depend on the number of electrons of the adsorbate state and the *d*-band which are involved in the interaction, and V_{ad} denotes the strength of the coupling between the adsorbate state and the *d*-band.

If the position of the *d*-band is slightly shifted the hybridization energy E_{d-hyb} changes with the change of the *d*-band center:

$$\delta E_{d-hyb} = -\sum_a C(F_a, F_d)\left(\frac{V_{ad}}{\varepsilon_a - \varepsilon_d}\right)^2 \delta\varepsilon_d = \gamma\delta\varepsilon_d\ , \tag{1.7}$$

The above observations suggest that changes of the electronic structure of the substrate can change the adsorption and reaction properties of the adsorbates. As mentioned before, the adsorption and reaction of adsorbates depends also on the surface morphology. As the MNPs have different electronic properties and morphology compared to extended surfaces, the adsorption and reaction of molecules on MNPs are expected to be different from those of the extended surfaces. In addition, in MNPs effects like particle size, and support effects can be studied.

1.3. Photon induced process on the surface

Generally, the absorption of UV photons by either the adsorbate or the substrate can lead to bond breaking within the adsorbate or between the adsorbate and substrate. These processes consist of photon absorption by the adsorbate or substrate associated with transition to an electronically excited state followed by nuclear motion leading finally desorption or reaction.

1.3.1. Photoexcitation mechanisms

For the primary excitation process three alternatives have been discussed. First, the photochemical process may be initiated by direct excitation within the adsorbate. On the other hand, hot carriers generated by the absorbed light within the substrate may attach to the adsorbate resulting in an excited adsorbate. Alternatively this can lead to transiently heating of the surface and to thermal chemistry.

1. ***An adsorbate localized process***: commonly called direct excitation involving the direct absorption of a photon by an adsorbate molecule. The photon typically excites the molecule from a ground state to an excited state in a similar way to a gas phase photoexcitation (see figure 1.4). Generally surface photochemical processes initiated by direct photon absorption of the adsorbate exhibit a wavelength dependence that is qualitatively similar to absorption by the corresponding gas phase molecule [Bun93, Chu94, Wat96, Yin91, Per93, Kid99, Ric91].

2. ***A substrate mediated process***: commonly called indirect excitation involving the adsorption of a photon by the substrate and electronic energy transfer to the adsorbate-substrate bond. Photons of wavelength in the region of IR and shorter photon wavelengths are absorbed by creation of charge carriers (electrons and holes) in the solid. As has been demonstrated in many theories and experiments, these carriers can induce adsorbate reactions [Cav93, Har95, Har95[a]]. Photochemical processes driven by initial photon absorption by the surface or bulk have been commonly reported for metal and

semiconductor substrates [Ric88, Fuk93, Fuk93^{a}, Bun88, Bun89, Yin90]. The photochemical processes follow the absorbance properties of the substrate. Theoretical models that have been proposed by Gadzuk [Gad90], Zimmermann and Ho [Zim95] and by Nakamura and Yamashita [Nak06] allow for a substrate hot electron attachment mechanism. According to the above models, the hot-electron attachment model consists of three separate steps: (i) excitation of electrons in the bulk; (ii) transport of excited electrons to the surface, including secondary electron creation through electron-electron scattering; and (3) tunneling of hot electrons into the unoccupied orbital of the adsorbate (see figure 1.4). Usually, distinctions between the adsorbate-localized and the substrate mediated processes have been made based on the excitation photon energy and polarization dependences of the two mechanisms [Yin91, So91, Zhu91].

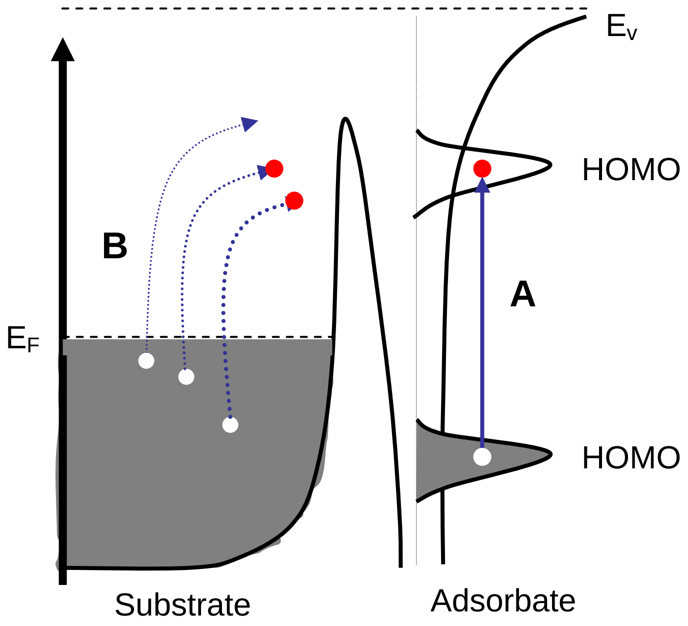

Figure 1.4.: Photo excitation mechanisms. **A** direct/ adsorbate localized and **B** indirect/ substrate mediated photoexcitation processes.

3. ***Laser-induced surface phonon excitation:*** photon irradiation can also induce thermally activated surface reactions by causing surface heating [Bar86]. Therefore in photon desorption studies, a thermal mechanism should also be considered.

1.3.2. Nuclear dynamics induced by photoexcitation

Having discussed the various photoexcitation mechanisms, the next question is what will happen after excitation of the molecule? One of the important points in surface chemistry is understanding each elementary step (including charge and energy transfer, the conversion of electronic energy to nuclear motion) that lead to desorption or reaction of adsorbate on the surface following excitation by photon irradiation. The information about the dynamical process on the surface can be obtained by monitoring the desorbed molecules. Experimental techniques such as time-of-flight (TOF) spectroscopy, laser induced fluorescence (LIF), and resonance enhanced multiphoton ionization (REMPI) are commonly used for studying the photodesorption dynamics of molecules from the surface.

Usually the photodesorption dynamics of adsorbed molecules is explained by a generalized and simplified model called the Menzel-Goemer-Redhead (MGR) model. The model was proposed independently by Menzel and Goemer [Men64] and Redhead [Red64] in 1964. Figure 1.5 a, shows a schematic one-dimensional PES illustrating the DIET process by the MGR model. According to this model, the desorption induced by electronic transition, DIET process starts with a Frank-Condon transition of the adsorbate from the ground state PES to an excited PES. During the lifetime of the adsorbate in the repulsive excited state PES, the electronic energy is converted to the nuclear motion. After a short but finite life time, τ, in the excited state PES, the adsorbate is quenched back to the ground state PES. Since the energy transfer increases with increasing τ, desorption could happen when the residence time of the molecule on the excited state PES is larger than a critical time, τ_c for desorption ($\tau > \tau_c$). If the energy gained by the adsorbate on the excited state PES is sufficient to overcome the barrier for desorption, the molecules can desorb with kinetic energy $E_k = E_k - D'$. Such information can be gained from time-of-flight (TOF) measurements.

Another commonly used model for DIET process is the Antoniewicz model [Ant80]. The Antoniewicz model assumes a charged excited state generated by charge transfer from the substrate to the adsorbate. The adsorbate may experience an attractive force*,* towards the surface, rather than the repulsion force proposed in the MGR model, due to the image charge produced on the surface.

In both models, the excess energy relative to the desorption barrier is distributed into the translational, rotational, and vibrational energies of the desorbed molecule. These models have been formulated in one dimension, but molecular desorption dynamics happens in a multi-dimensional configuration space, in which the internal motions of the molecule are also included.

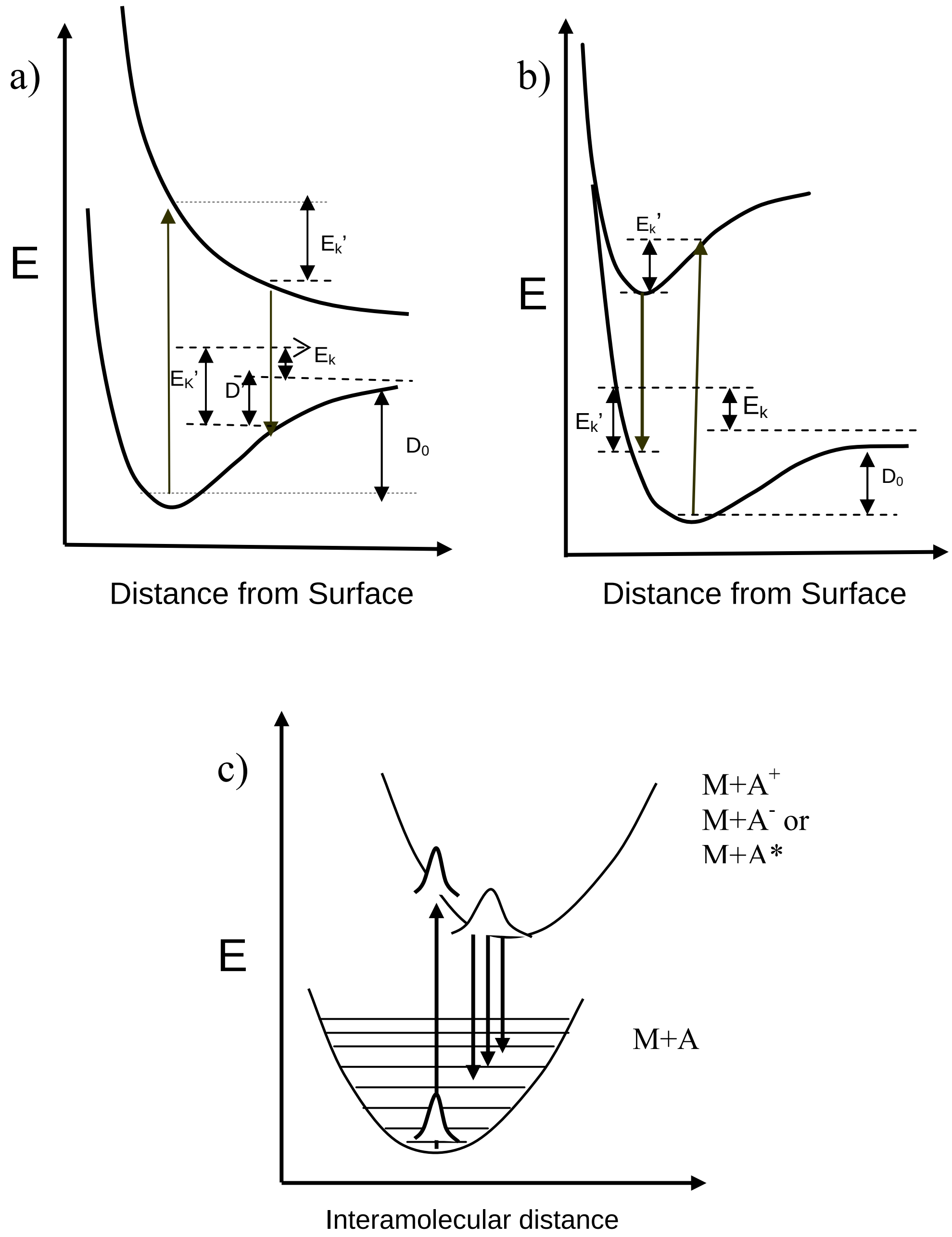

Figure 1.5.: Schematic illustration of a) MGR model, b) Antoniewicz model, and c) harmonic potential energy curves showing the excitation of internal vibrational modes in the same duration as the excitation and de-excitation processes in the MGR / Antonievicz models.

Theoretically, the rovibrational distributions of the desorbed molecules have been investigated using semiclasical [Gad90, Guo99], quantum dynamical [Saa06] and impulsive [Zim94[b]] models. For MGR-type photodesorption the vibrational excitation mechanism can be described in terms of two Frank-Condon transitions between a pair of displaced harmonic oscillators (see figure 1.5 c) [Gad90, Zim97]. The Franck-Condon transition projects the molecule from the vibrational ground state $|0\rangle$ of the ground state potential curve onto the slope of the excited state potential curve where the system evolves according to the excited state Hamiltonian H_e:

$$|\psi(t)\rangle = e^{-iH_e/\hbar}|0\rangle \qquad (1.8)$$

After a certain residence time t, another Frank-Condon transition projects the evolved wave function onto the vibrational states of the ground state. The probability of exciting the v^{th} vibrational state $|v\rangle$ is given by $|\langle v \mid \psi(t)\rangle|^2$.

$$P_v(t) = \left| \sum \langle v \mid n_e \rangle e^{-i\omega_e n_e t} \langle n_e \mid 0 \rangle \right|^2 \qquad (1.9)$$

The degree of vibrational excitation depends on the vibrational frequency multiplied by the lifetime of the intermediate state. However, the vibrational distributions predicted from the above model (assuming a charge $\rho = 1$ transfer) is very high compared to the experimental results. Therefore, an incomplete charge transfer from the substrate to the adsorbate was suggested, i.e., the adsorbate will have a fraction of charge [Guo97[a],Zim97]. However, such a fractional charge assumption may also result in a weak or even negligible image charge attraction which makes the Antoniewicz model questionable for photoinduced processes on metal surfaces.

The rotational excitation of the desorbed molecules is usually explained by the classical impulsive model [Zim95, Mur95]. In the impulsive model the excess energy, E_K, gained in the excitation/ de-excitation process (in the MGR/Antoniewicz models) is transferred to the molecule as a momentum, $\boldsymbol{P}$. After desorption the momentum $\boldsymbol{P}$ is converted into the linear momentum of the center of mass (which results in the translational motion) and into the rotational angular momentum of the nuclear motion ($\boldsymbol{L} = \boldsymbol{P} \text{ x } \boldsymbol{r} \sin\theta$), where θ is the tilt angle.

$$E_k = \frac{P^2}{2m_1} = E_t + E_r = \frac{P^2}{2M} + \frac{(P \times r \sin\theta)^2}{2I}, \tag{1.10}$$

where M is the total mass of the molecule, I is the momentum of inertia of the molecule, and θ is the tilt angle of the molecular axis of the desorbing molecule from the surface normal at the moment of bond breaking.

The above model explains not only the rotational excitation but also predicts a positive correlation between the translational and rotational excitations. Hasselbrink also proposed a classical model for the positive correlation between the rotational and translational distributions [Has95, Has90]. In addition, the role of the ground-state and excited-state PESs on the product translational/rotational correlation has been discussed [Che98, Guo97].

So far we have considered a single excitation/ de-excitation process which is appropriate for continuous wave (cw) and nanosecond (ns) laser pulse excitations that create low densities of charge carriers in the substrate. However, the photochemistry induced by an intense fs laser pulse can be different from cw and ns excitation. Compared to continuous wave or ns laser induced desorption, fs laser induced desorption shows some unique and interesting properties [Del95, Bus95, Eic96]. Most of the systems studied so far display similar characteristics such as: 1) significant enhancement of desorption yield, 2) nonlinear dependence of the yield, Y, on the laser fluence $\boldsymbol{F}$ ($Y = \boldsymbol{F}^n$ where n is reported in the range 3 – 7), 3) very short system response time (in the sub picosecond regime), 4) changed translational and internal energy distributions of desorbing molecules.

In a fs laser excitation of the metal, a very high electron temperature can be reached. Such high transient electron temperatures can create a new regime of energy transfer to the adsorbate. Two basic models have been applied to explain the femtosecond laser induced desorption process on metal surfaces: i) the mode of desorption induced by multiple electronic transition (DIMET) [Mis92, Gao95], and ii) the frictional model [[New91, Spr96, Fri06]. The DIMET process is characterized by a successive electron excitation of the adsorbate at a time interval less than the time for damping of energy in the molecule surface coordinate. Hence at such very high hot electron densities induced by an ultrashort light pulse, vibrational excitation rates can be faster than the rates of vibrational damping, and the resulting vibrational ladder climbing in the ground electronic state can lead to desorption. Another theoretical approach is electronic frictional coupling between the adsorbate and the thermalized hot electrons. In this model the adsorbate vibration leads to a motion along the reaction coordinate and therefore to an energetic shift of its resonance with respect to the Fermi level, E_F. Unoccupied states below E_F will force substrate electrons to scatter into the resonance, whereas electrons in states higher than E_F will scatter back into the substrate. Therefore this coupling results in a fluctuating force on the nuclear coordinates and can induce chemistry.

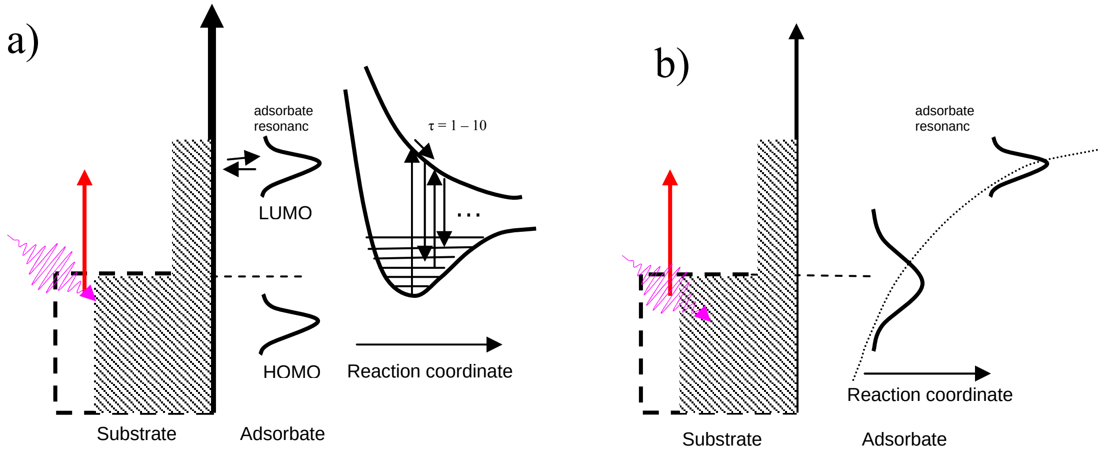

Figure 1.6.: Schematic view of a) the DIMET process, desorption process through multiple excitation/ de-excitation of the adsorbate, and b) the frictional coupling process showing an adiabatic coupling between the substrate hot electron that flows back and forth between the metal substrate and the low laying adsorbate levels.

Chapter 2

Experimental details

The purpose of this chapter is to provide information on the experimental apparatus and the techniques used in this study and also to provide an understanding of how the experiments were performed and analysed.

2.1. Vacuum system

Surface experiments, especially those that need a long measurement time, require ultra-high vacuum (UHV) conditions. The UHV condition is important to reduce contaminations buildup on the surface as well as to improve the signal to noise ratio in measurements as a result of decreased quantity of background gases.

The vacuum system used in this study consisted of two vertically connected cylindrical chambers of 40 cm diameter separated by a gate valve (see Figure 2. 1).

The upper chamber (preparation chamber) is equipped with: a LEED/Auger system (Specs ErLEED Digital) for surface characterization, a differentially pumped quadrupole mass spectrometer (QMS) (Hiden Analytical, HAL 301/3F) with a movable extension flange for thermal desorption measurements, an ion gun and leak valve for Ar^+ sputter cleaning, another leak valve for background gas dosing like O_2 during oxidization of NiAl (110) surface, a quartz microbalance (Caburn MDC) for monitoring the thickness of the metal film, and a triple electron beam metal evaporator (Omicron EFM-3) for metal atom deposition. This chamber is pumped by a turbo molecular pump (Varian Turbo V550) backed by a rotary pump (Pfeiffer-Vacuum).

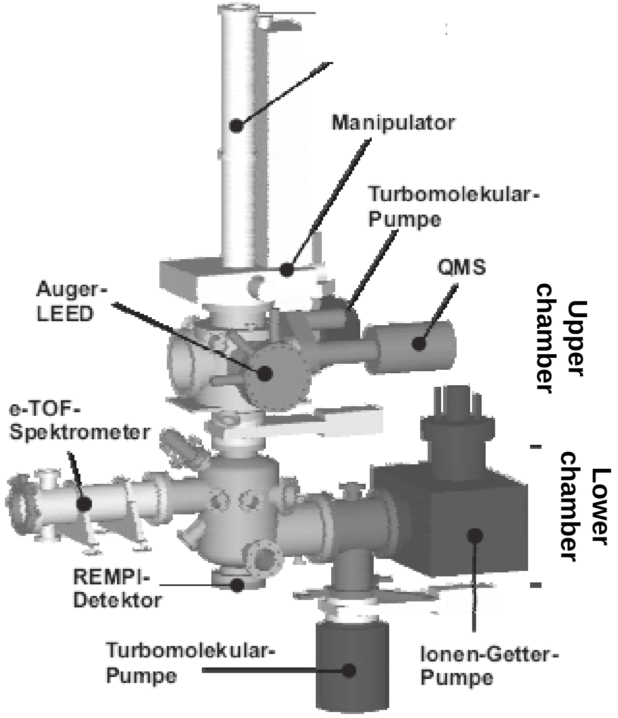

Figure 2.1.: The upper and lower vacuum chambers and the location of measurement equipments and pumps (from [Rak03])

The lower chamber (measurement chamber) is equipped with: a QMS with a liquid nitrogen cooled shroud for mass-selected time-of-flight (MS-TOF) measurements, a directional pulsed doser with a stainless tube inside the UHV for direct dosing of the adsorbate on the sample surface, a manual leak valve to introduce adsorbates to the chamber for background surface coverage, a REMPI detection system for state-resolved measurements, an electron-TOF spectrometer for 2PPE energy and time measurements of the photoelectrons (not used in this thesis work). For the introduction of the desorption and detection laser light, special fused silica glass windows, which have better transmittance than normal glass windows, were used. This chamber was pumped by a turbomolecular pump (Varian Turbo V550) backed by a rotary pump (Pfeiffer-Vacuum), a titanium sublimation pump (Varian Vacion plus 300) and an ion pump.

Following chamber bake out, a residual pressure of less than 3 x10^{-10} mbar can be achieved and during liquid helium sample cooling the chamber pressure decreased further to below 7 x 10^{-11} mbar. The base pressures in these chambers were measured by independent ion gauges located in the upper and lower chambers and the pressure in the forepumps were measured by Pirani gauges.

The crystal manipulator was placed vertically along the chambers' central axis. The manipulator consisted of a UHV *x*-*y*-*z*- stage and a rotary flange. The sample could be moved by $\pm$ 25 mm of translation in the *x*- and *y*- directions, 420 mm in the *z*- direction and 360 º rotations around the *z*- axis. In the *z*- direction the sample could be transferred from the preparation chamber to the measurement chamber or vise versa. These arrangements allowed the sample to be positioned appropriately for any given sample preparation or experimental measurement.

2.2. Sample manipulation, cleaning and preparation

i. Sample manipulation

The Ag single crystal and the NiAl (110) crystal were each 10 mm in diameter and 2 mm thick. The crystals were installed on two opposing sides of the manipulator. The crystals were spotwelded to a tantalum wire (diameter 0.25 mm) and connected to molybdenum rods which were in thermal contact with a liquid helium cryostat. A sapphire plate was located between the sample holder and the end of the cryostat. It was used for electrical isolation with good thermal contact at low temperatures, and for enhancing thermal isolation at higher temperature. Moreover, a copper heat shield surrounded the cryostat in order to reduce the thermal radiation from the environment i.e., the UHV chamber which was at room temperature.

For cooling the samples, liquid helium (LHe) was flowed continuously through the cryostat. After ~ 1 hr continuous LHe flow, the samples reached between 30 and 40 K. Heating was accomplished either by radiation heating (< 700 K) or by high voltage electron bombardment from a tantalum filament mounted behind the back of the crystal. The sample temperature was monitored by type-E chromium-constantan (NiCr - CuNi) thermocouples spotwelded to the sides of the crystals.

ii. Sample cleaning and preparation

When the Ag or NiAl crystals were newly polished or had been exposed to the atmosphere for a long time, several sputter/anneal cycles were needed to get a clean and well-ordered surface. The order and cleanness of the sample were checked by LEED and AES. However between the experiments only few sputter anneal cycles (1-3 cycles) were enough.

Daily preparations

It was necessary that the sample surfaces must be free from contaminants before an experiment was begun. The single crystal Ag was cleaned by 3 sputter/anneal cycles prior to each experiment. The sputtering was done at a crystal temperature of 523 K by Ar^+ ion bombardment (0.5 kV, 3 µA ion current, 20° incidence angle) for 20 minutes. Following the sputtering the sample was annealed to 725 K for another 20 minutes.

Ag nanoparticles (Ag NPs) were grown on thin alumina films on a NiAl (110) surface [Nil00]. Since thermal processing without and with photon irradiation of the NO dimer adlayers investigated here leads to irreversible changes of the Ag NPs, a new sample of the latter had to be prepared for each experiment. Hence, the daily preparation included cleaning the NiAl (110) crystal, preparing an oxide film on it depositing Ag atoms on the oxide films and annealing to form the Ag NPs. The NiAl (110) was cleaned by sputtering the surface with Ar^+ ions bombardment (1.5 kV, 5 µA ion current, 45 ° incidences) at a sample temperature of 723 K for 1 h followed by annealing at 1250 K for 5 minutes. The latter smoothes the surface and restores the original stoichiometry. A thin alumina film was prepared by oxidation of the clean NiAl (110) surface by exposing it to 4 x 10^{-6} mbar oxygen at 540 K for 15 minutes followed by annealing it at 1200 K for 2 minutes. The oxidation/annealing cycle was repeated three times in order to fill the open patches and produce a well ordered smooth structure [Jae91].

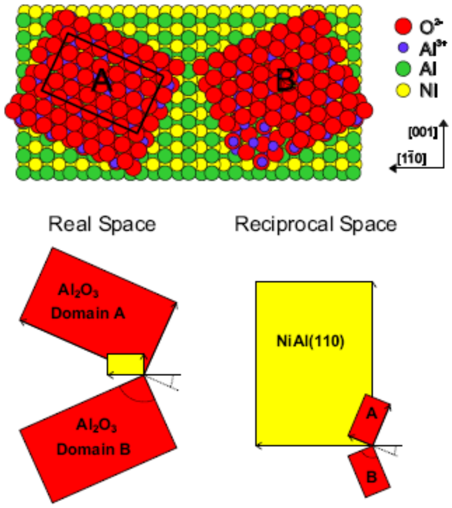

Figure 2.2.: Structures of Al_2O_3/NiAl (110) with rotational domains A and B and the corresponding unit cells in real and reciprocal space (from ref. [Eve06]).

The ultrathin alumina overlayer on NiAl (110) surfaces grows well ordered and two dimensional with a thickness of 5 Å. It is composed of two Al-O double layers which are oxygen terminated towards the vacuum. The Al_2O_3 grows in twin domain boundaries, denoted A and B (see figure 2.2), inclined by 24° against the [1-11] direction of the NiAl

(110) surface. The film grows commensurate along the [1-11] direction and incommensurate along [001] direction. The existence of the two reflection domains as well as a slight mismatch between the substrate and the film lead to a characteristic network of line defects. Interestingly the oxide films exhibit an excellent reproducibility in preparation. If the same procedure is used these networks of line defects (domain boundaries and step edges) on the oxide films are produced in nearly the same density; they play a central role in the growth of metal nanoparticles [Lib94, Kul03, Kre05 Ade98].

The silver nanoparticles were prepared by deposition of silver atoms (at an Ag atom flux of 1 Å/min) on the oxide film surface at room temperature. Silver atoms were evaporated from a molybdenum crucible of a triple electron beam metal evaporator (EFM-3) by electron bombardment. Prior to each deposition, the rate was calibrated by a quartz microbalance. The sample was biased at +850 V during Ag deposition in order to prevent bombardment of the sample by Ag^+ ions created in the evaporator which could destroy the shape of the already grown nanoparticles or could create new defect sites on the oxide films.

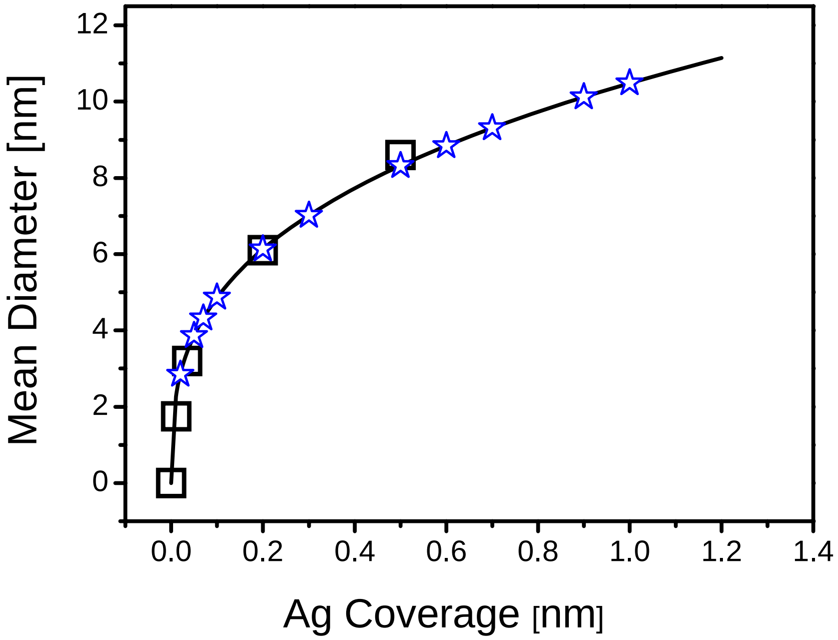

Figure 2.3.: Mean particle diameter as a function of Ag coverage. The solid line represents the cubic fit of the STM data (squares). Blue stars represent the mean diameters used in this work.

At room temperature silver atoms are very mobile on the alumina film. They preferentially nucleate at defects (domain boundaries or step edges). Oxides have lower surface free energy than metals and the metal-oxide adhesion energy is small; therefore silver prefers to grow in three-dimensional Volmer-Weber mode [Bau99]. According to the STM study [Nil00], Ag nanoparticles preferentially grow in an oblate spheroids shape of aspect ratio (diameter/hight) of ~1.7. The mean diameter of the nanoparticles can be varied by varying the amount of evaporated Ag, just by varying the deposition time keeping all other parameters constant. As the size of the nanoparticles changes there is only little change in the particle density and the aspect ratio. The mean diameter as a function of the amount of Ag coverage was obtained from STM images as shown in figure 2.3. The particle densities prepared by the above procedure are nearly constant, ~ $4\text{x}10^{11}$ cm^{-2}. Information about the nanoparticle sizes and densities have been obtained from previous separate STM studies [Nil00].

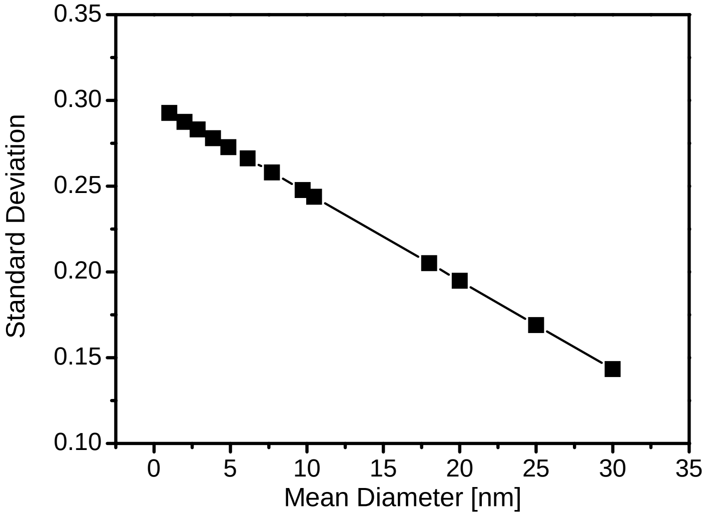

Figure 2.4.: The width of particle size distribution of Ag NPs on Al_2O_3/NiAl (110).

To obtain the size distribution some STM images were analyzed. The standard deviations as a function of the Ag NPs size at various mean diameters is shown in figure 2.4.

2.3 Gas handling and exposure

Several gases have been used in the experiments. Some, like Ar and O_2, were used for sample cleaning and preparation and others, like NO, N_2O etc were used for experimental purposes. These gases were taken from separate bottles and could be introduced to the chamber either by using a pulsed directional doser or a manual leak valve. The Ar gas line was separated from the other gas lines; all other gases used a common line. Since most of the measurements were done using NO as an adsorbate, I will focus on the purification and delivering of purified NO to the chamber.

The original purity of the NO gas used in this experiment was 99.9 %. However, NO may react on the inside wall of the bottle or the gas lines and form N_2O, NO_2 and other reaction products. Therefore, before each experiment, the NO gas delivered from the cylinder was purified by a freeze / pump / thaw procedure as follows. First NO was condensed at liquid nitrogen temperature (~ -191 ºC, the freezing point of NO is -163 ºC at 1 atm.) and the low boiling gases such as CO, O2, N2, etc were pumped off by a rotary pump. This procedure was repeated three times. And before admitting the gas to the UHV chamber, the high boiling impurity gases such as CO_2, NO_2, N_2O, HNO_3 etc were trapped by liquid nitrogen-ethanol mixture (~ -100 ºC) until the end of the measurement. At the end of the purification procedure, there was a pressure of ~ 1 mbar NO in the gas line.

The crystal surface was dosed with NO molecules by one of the following methods. The first method was using a directional pulse doser. With this doser we can achieve higher coverages in shorter times with smaller gas load and background pressure. The second method was by backfilling the chamber to a static pressure using a manual leak valve.

TPD and MS-TOF measurements were performed after covering the sample to saturation using a directional pulse doser, while for state-resolved measurements a manual leak valve was used. In the latter case the NO coverage should be maintained at constant value during the course of the measurement. The reason why we used the manual leak valve for dosing was due to the geometrical configuration of the directional pulse doser and the sample position during the REMPI measurement. Prior to gas exposure the sample was quickly heated to 300 K to remove impurities adsorbed during the cooling period.

2.4. Laser systems

The experiments described in this thesis were performed using three independent laser systems: the Nd-YAG nanosecond pulsed laser, a Ti: Sapphir femtosecond pulsed laser, and an excimer laser pumped dye laser system. The first two lasers were used for inducing desorption of molecules from the surface while the third laser system was used for the measurement of the final state distribution of photodesorbed molecules from the surface. In this section some basic principles on the generation and operation of these lasers will be described.

Nd-YAG laser

Most of the photodesorption measurements were performed by Nd-YAG (GCR 190) nanosecond laser pulses at a repetition rate of 10 Hz and pulse width of 5 ns. The laser medium is composed of Nd^{3+} ions trapped in a rod of yttrium aluminum garnet (YAG). Coherent radiation of 1064 nm wavelength is generated by creating a population inversion in the laser medium by optical pumping from a flash lamp. Moreover, the pulsed Nd-YAG laser was equipped with a Q-switch in order to achieve the highest possible output intensity [ManYG].

From the high intensity fundamental wavelength (1064 nm) output, it was possible to generate higher harmonics through a non-linear optical process by passing the beam through properly phase matched potassium dideuterium phosphate (KDP) crystals. The KDP crystals were housed and temperature stabilized in the harmonic generator. A first frequency doubling KDP crystal gives 532 nm (second harmonics). To produce 355 nm (third harmonics), the fundamental (1064 nm) and second harmonics (532 nm) were mixed in a second KDP crystal. 266 nm (fourth harmonics) could be generated by the third KDP crystal that generates the second harmonics of the second harmonics of the fundamental, i.e. the second harmonics of 532 nm. In order to maximize the output power the crystal positions had to be properly adjusted. The fundamental, second, third, and fourth harmonic beams were separated by using a pair of appropriate dichroic mirrors that selectively reflect one wavelength (the desired wavelength) while transmitting the others.

The desired laser output was then guided towards the chamber by using appropriate mirrors. Near the chamber, the beam was expanded three times using pairs of lenses. And then only the center (uniform) part of the Gaussian beam profile (5 mm diameter) was selected by using an iris and introduced to the chamber through a fused silica glass window.

Femtosecond laser system

The second desorption laser used was a regenerative amplified Ti:sapphire laser system which generates pulses of less than 100 fs width and maximum pulse energy of 0.8 mJ, at a maximum repetition rate of 1 kHz. Details about the generation and operation of the femtosecond laser system used in this study have been reported in previous theses works [Rak03, Eve06].

Detection (probe) laser

For state-resolved detection of desorbed molecules a continuously tunable laser source was needed. Generation of tunable UV laser light was achieved by an excimer laser-pumped dye laser. Because of their wide range wave length tunability, dye lasers are one of the most important types of lasers in electronic spectroscopy.

In this study a tunable dye laser system (Sirah Cobra-Stretch) containing an oscillator, a resonator, and a glancing incident grating etc., was used. The laser medium is an organic dye (coumarin-2) solved in an organic solvent (methanol). The dye laser is pumped by an excimer laser (Lambda physics LPX 140) operating with a XeCl gas mixture; it generates light pulses with energy of about 140 mJ at a wavelength of 308 nm and pulse width of 15 ns which are delivered to the dye cell containing dye solution. The oscillator serves as the laser cavity, while the amplifier amplifies the low powered beam extracted from the oscillator in the second dye cell.

The dye laser was also equipped with a frequency conversion unit (FCU) which was used for frequency doubling of the fundamental dye radiation (432-474 nm). The optical setup of the FCU consists of a BBO crystal at a cut angle of 57.4º and a compensator. Frequency doubling generates a wavelength between 216 and 237 nm [ManDY].

The beam emerging from the FCU contains both the second harmonic generator (SHG) and the fundamental beams. The wavelength separation was done by a pair of Pelline Brocas prisms. After wave length separation by the first prism the fundamental beam was guided on a ceramic dump, whereas the SHG beam passed close to the dump to the next Pelline Brocas prism which was used to compensate the angular and linear shifts induced by the first prism. The linewidth of the output beam was about 0.3 cm^{-1} at a pulse energy of 1.5 mJ.

The beam was directed towards the UHV chamber by three mirrors. To minimize the large fluctuations in the dye laser intensities during long range wavelength scans, we have used a six hole fast motorized filter wheel with five of the holes filled with fused silica neutral density metal filter mirrors of various optical density (0.03, 0.1, 0.2, 0.3, 0.4, 0.5). The motorized wheel was controlled by a personal computer (PC) which could adjust to the appropriate filter when there was a fluctuation on the probe laser. The motorized filter was also used to keep the laser power in the quadratic regime, i.e., at low laser power (see figure 2.12). Before entering the chamber, the beam was gently focused by a 250 mm focal length lens placed such that there was no saturation effect at the ionization point.

2.5. Experimental methods and data acquisitions

In this thesis the thermal and photochemistry of NO dimers adsorbed on Ag surfaces were investigated using different techniques. The techniques were, temperature programmed thermal desorption (TPD); mass-selected time-of-flight (MS-TOF) and resonance-enhanced multiphoton ionization (REMPI) detection of photodesorbed neutrals. In this section the experimental methods, the data acquisition procedures, and the data analysis processes will be described.

2.5.1. Temperature Programmed Desorption (TPD)

Temperature programmed (thermal) desorption is one of the most commonly used techniques to characterize the adsorption bond of adsorbed molecules on a surface. Many studies have been performed concerning the technical side of the experiment as well as the theoretical analysis of the recorded TPD spectra [Ehr61 ,Kin75, Men75, Mas96].

Experimentally, it consists of applying a linear ramp of the temperature, $\beta = dT/dt$, to the substrate which is covered by adsorbate, and recording the particles leaving the surface as a rise in pressure. Usually the latter is done mass-selectively by a quadrupole mass spectrometer (QMS).

An accurate analysis of TPD spectra is complicated and time consuming and requires extensive high quality data. In this way, it is possible to determine activation energies (E_{des}), pre-exponential factors (v), and order of desorption from a series of TPD spectra. This is simple only in special cases; usually it is a rather complicated problem because both the E_{des} and v are frequently independently coverage dependent [Nie07].

Traditionally, the analysis of TPD spectra is based on the Polanyi-Wigner [Kin75, de J90] equation of the desorption rate:

$$-{}^{dN_s}\!/_{dT} = v\ (N_s)^x\ \exp(-E_{des}/RT)\,, \tag{2.1}$$

where, x is the order of reaction, N_s is the population in state s, E_{des} is the activation energy of desorption, R is the gas constant, and v is the pre-exponential factor.

For first order kinetics with coverage-independent parameters Redhead [Red62] showed that E_{des} can be approximately determined from the desorption peak temperature T_{max} with the assumption of a “normal” pre-exponential factor:

$$E_{des} = RT_{\max}\left[\ln\left(\frac{vT_{\max}}{\beta}\right) - 3.46\right]\,, \tag{2.2}$$

where T_{max} is the peak maximum temperature, and β is the heating rate, dT/dt, E_{des} , R and v have the same meaning as in equation (2.1)

As mentioned, this equation is only applicable if E_{des} and v are coverage independent and it works only when there is a reliable value for the pre-exponential factor; frequently a value of 10^{-13} s^{-1} is assumed (1). If several peaks in the TPD spectra are observed which are either caused by different co-existing adsorption states or by coverage-dependent parameters, this formula does not apply. Therefore in many cases the analysis of TPD spectra remains qualitative. Nevertheless, the TPD spectra can still be used as fingerprints of the adsorbate layer.

In this thesis work, this technique was used for semi-quantitative characterization of NO dimer layers adsorbed on silver nanoparticles of varying mean size. Moreover, it has been used also to characterize the adsorbates or photoproducts which remained on the surface following photon irradiation. An important aspect is that the integral over the desorption traces represents the total amount of that molecular species which was desorbed, i.e which had been in the surface before starting the temperature rise.

---

(1) The *normal* prefactor is kT/h, so for low T desorption a lower value is appropriate.

The QMS analyzer is located in a differentially pumped stainless steal housing with a 2 mm diameter nozzle directed towards the center of the chamber. For TPD measurements the crystal was positioned at about 0.5 mm in front of the nozzle. This arrangement prevents detecting molecules from the surrounding of the sample. After positioning, the crystal was heated linearly by radiation from behind with a glowing filament while monitoring several mass fragments simultaneously with the QMS. The QMS ionizer operated at an emission current 269 μA and the secondary electron multiplier (SEM) voltage was 2400 V. During TPD measurements the sample was negatively biased at higher potential (-104 V) compared to the QMS ionizer to prevent electrons emitted from the QMS filament causing electron stimulated desorption or damage.

The QMS was run in the counting mode. The counts measured by the QMS were sent to the digital to analog converter (DAC) board. The amplified thermocouple voltage was sent to an analog to digital converter (ADC) board and converted to temperature. A labview program (developed by Prof. Kazuo Watanabe) was used to linearly increase the heating rate by controlling the filament current based on the feedback from the thermocouple. MASsoft software installed in the PC was run in multiple ion detection (MID) mode. It monitors a series of masses and auxiliary inputs (here: thermocouple signal) and plots the mass signal intensities and thermocouple temperature readings as a function of time. The TPD spectra, i.e. the mass signal intensities as a function of sample temperature can then be plotted.

2.5.2. Mass selected time-of-flight (MS-TOF) measurements

The basis of the TOF method is that from the measured time, t, required for a particle to travel a distance, l, one can determine the speed, v, of the particle.

$$v = \frac{l}{t} \tag{2.3}$$

If all the particles leave the surface at the same time, faster molecules will arrive earlier than slower ones. This principle is applicable in many systems like molecular beam studies and desorption studies to investigate the kinetic energy, KE, ($KE = \frac{1}{2}mv^2$ where m is the mass) of molecules in the gas phase.

A QMS with an electron impact ionizer is commonly used to detect neutral particles. QMS TOF experiments are performed by measuring the number density of mass selected particles in the ionization region as a function of their arrival time *t, S(t)*. The same principle is applicable for the laser spectroscopic technique REMPI to measure state resolved TOF spectra. One has to be careful that these detectors measure the number density, $\rho(r,t)$ in the space domain, not in time domain [Zim95]. Because of the smaller probability of faster molecules to be ionized and detected compared to the slower ones, the measured TOF spectra do not represent the TOF distribution. However, one can derive the TOF distributions, *I(t)* from the measured TOF spectra, *S(t)* using:

$$I(t) = \left(\frac{r}{t}\right)\rho(r,t) \propto \left(\frac{1}{t}\right)\cdot S(t) \tag{2.4}$$

Therefore the TOF distributions measured with density sensitive detectors like QMS and REMPI can be written as:

$$S(t) \propto \frac{1}{t^4}\exp\left(-b/_{t^2}\right), \tag{2.5}$$

with $b = mr^2/2kT$, the mean translational energy $<E> =2kT$, where k is the Boltzmann constant.

Once it has the form like equation (2.5), one can easily derive the velocity, *P(v)* or energy, *N(E)* distributions from it.

Generally the TOF distributions of photodesorbed molecules can be modeled, in analogy to supersonic molecular beams, using a slightly modified function known as *shifted* Maxwell Boltzmann distribution which can be interpreted as a thermal distribution at a temperature *T* superimposed on a *drift velocity* v_0 [Zim94]. The shifted Maxwell Boltzmann distribution can be written by adding the *drift velocity* v_0 in the exponential part of equation (2.5).

$$f(t) = \frac{a}{t^4}\exp\left(-b\left(\frac{l}{t} - v_0\right)^2\right), \tag{2.6}$$

This distribution will have a thermal distribution when v_0 is 0 (equation (2.5)), a broader distribution when v_0 is negative and narrower distribution when v_0 is positive.

It should also be noted that the measured TOF spectra represent the actual time of flight of the neutral particle to the ionizer plus the time taken for the ion to accelerate from the ionizer to the detector. Therefore, appropriate subtraction of the latter time is needed before fitting the measured TOF spectra.

The mass selected time of flight measurements (QMS-TOF) used in this study were carried out following photon induced desorption of NO from silver surfaces. The experimental setup is shown in figure 2.5. The desorbed molecules are detected by a quadruple mass spectrometer, at m/e = 30, according to their arrival time. The QMS signal was amplified by a preamplifier (ORTEC VT120) and sent to a discriminator (ORTEC 436 100MHz). The NIM pulses were counted with a multichannel scaler (FAST MCS 7882) at a dwell time of 0.8 µs. The data acquisition was synchronized with the laser pulse by programming the ADC board to wait for trigger pulses generated by the laser (detected by PMT1). The data acquisition starts when it receives an external trigger TTL pulse, when the shutter is opened. The acquired TOF spectrum is then plotted on the computer.

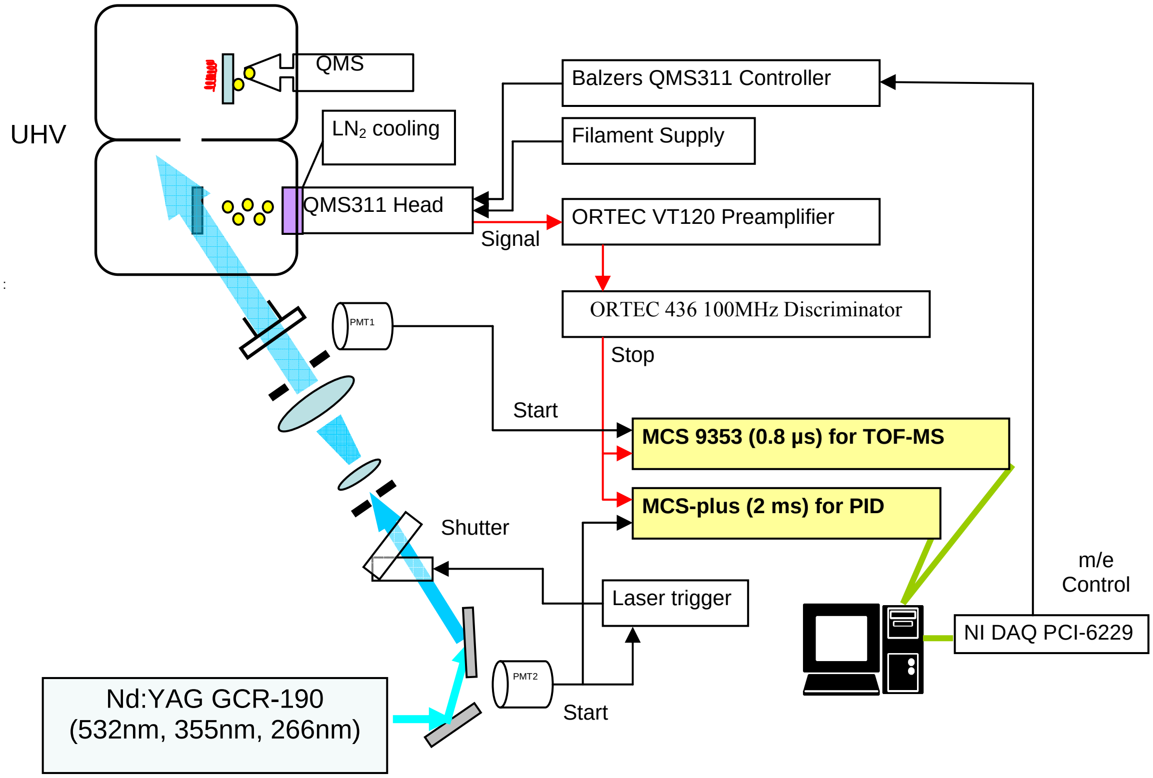

Figure 2.5.: Schematic view of the experimental setup of MS-TOF, PID, and TPD measurements.

i. Determination of translational energy

The main purpose of the TOF measurements was to investigate the translational energy of photodesorbed molecules initially adsorbed on Ag surfaces. We determine the mean translational temperature from the fitting of the measured TOF spectra by *shifted* Maxwell Boltzmann functions. Before the fitting, the ion drift time, t_0, in the QMS was determined and subtracted from the measured TOF spectra (see for example reference [Kim09]). The flight distance, *l*, was 19 cm, and *m/e* was 30. We guessed the initial fitting parameters "*a*" and "*b*" by visual inspection of the TOF spectra (peak position, t_m and peak height *M*) and assuming $v_0 = 0$. Depending on the nature of the TOF spectrum, the sum of two or three *shifted* Maxwell Boltzmann functions were used for fitting.

Figure 2.6 shows an example of a TOF spectrum fitted to the sum of two shifted Maxwell- Boltzmann function.

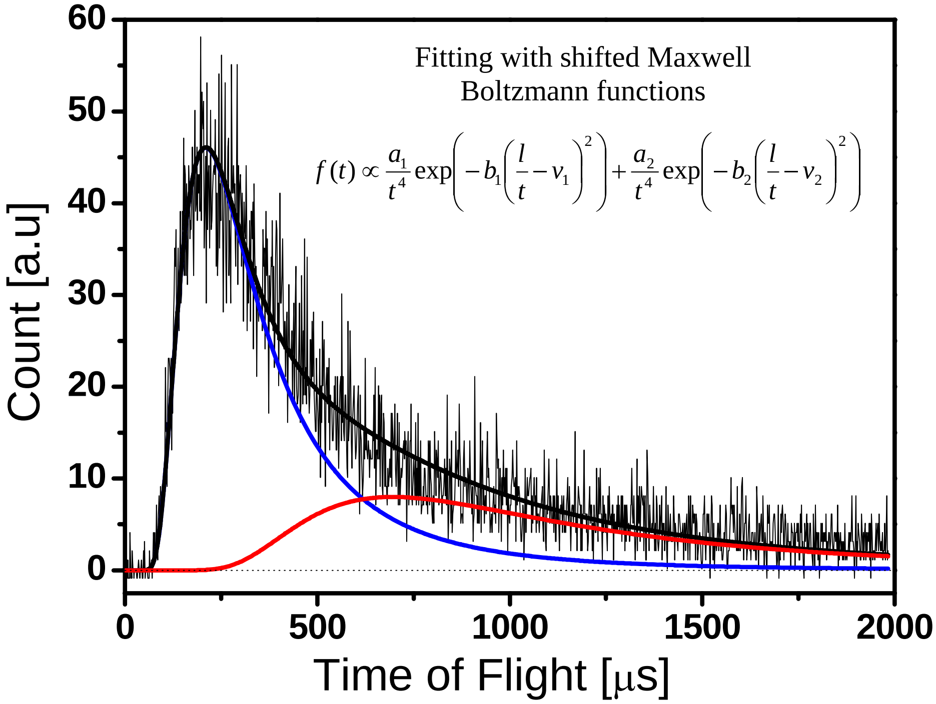

Figure 2.6.: TOF spectra collected along the surface normal for 3.5 eV photodesorption of NO from 8-nm Ag NPs with fits generating the sums of two *shifted* MB functions.

ii. Shot dependent photon-induced desorption (PID) yield

The photodesorption efficiency of adsorbed molecules on surfaces can be estimated from the coverage change as a function of the total number of photons arrived. However, this description is valid only:

- when the process is a one-photon photo removal process,
- when the NO desorption probability is coverage independent, and
- when desorption is the only photoinduced process.

The experimental setups for these measurements were exactly the same as those of the QMS-TOF measurements. The QMS signal was amplified by a preamplifier (ORTEC VT120) and sent to a discriminator (ORTEC 436 100MHz). The NIM pulses were counted with a multichannel scaler (MCS-plus) at a dwell time of 2 µs. In addition the laser pulses were counted and detected by a photomultiplier (PMT1). In this detection scheme the PC records the integrated QMS signal intensity as a function of total photons.

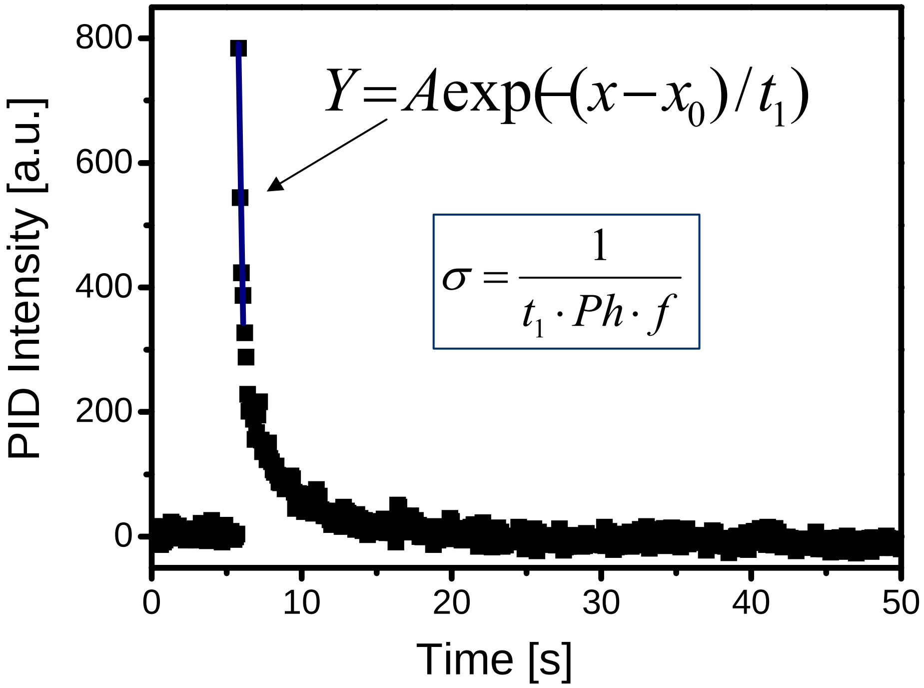

Figure 2.7.: PID spectra of NO desorbed along the surface normal from 8-nm Ag NPs with 3.5 eV in *p*-polarization. The desorption cross section was determined from equation (2.8) by fitting ~50 % of the decay with equation (2.7).

The decaying signal reflects the decreasing coverage of adsorbed NO dimers during laser irradiation. In fact, as mentioned above there are also other factors, other than NO desorption, which lead the signal to decay (like, formation of N_2O + O, change of adsorption site, etc). In our calculation of cross sections, however, we have focused only on the NO dimer dissociation and subsequent NO monomer desorption channel. This makes the cross section determination approximate. We calculated the cross sections from the decay constants of the exponential fittings of the first 50 % of the decay, in the range where the clearly predominant process determining the signal decrease is the decay of the dimer concentration. Justification of this procedure comes from the good adherence of that part of the signal decay to the semilog law.

$$Y = A\exp(-(x - x_0)/t_1), \tag{2.7}$$

where P_h is the irradiance (photons/cm^2), Y is the desorption signal and A is a constant.

$$\sigma = \frac{1}{t_1 \cdot Ph \cdot f} \tag{2.8}$$

where σ is the PSD cross section, t_1 is the time we got from the exponential fitting (equation 2.7), P_h is the irradiance, and f is the repetition rate of the laser.

Figure 2.7 shows an exponentially fitted PID spectrum.

2.5.3. State-resolved detection of NO via (1+1) REMPI

Resonance Enhanced Multiphoton Ionization (REMPI) is a laser spectroscopic technique which is used to detect molecules in their specific internal quantum states. It is a two step process in which in the first step the molecule is excited to an intermediate excited state by absorbing one or more photons, and in the second step the molecule absorbs another one (or more) photon(s) that lead(s) to ionization.

i. Spectroscopy of nitric oxide

NO is very suitable for REMPI analysis because a simple (1+1) scheme can be applied to it. This (1+1) REMPI technique was implemented here for the quantum state-resolved detection of photodesorbed NO. This is achieved by two photons of the same energy as follows: The first photon promotes NO from its ground state, $X^2\Pi$ to the first excited state, $A^2\Sigma$, and the second photon of the same energy ionizes the molecule by promoting it to the ground state of the NO^+ ions, $X^1\Sigma^+$.

Nitric oxide has an unpaired electron in its $2\pi^*$ orbital. So the molecule has a total spin $S = 1/2$ and $\Lambda=1$. The spin-orbit interaction leads to a partial lifting of the fourfold degeneracy of the ground state into two doubly degenerate states [Her50, Mal82, Zim95].

For the Hund's case (a), as shown in figure 2.8a, both the orbital angular momentum and the spin angular momentum are strongly coupled to the internuclear axis. Hund's case (a) is the reasonable description for low J'' values of the $X^2\Pi$ state. Based on case (a) the resulting projection of the total electronic angular momentum along the internuclear axis will have a value of $\Omega = 3/2$ or $1/2$, depending on the relative orientation of the spin and orbital angular momenta. Each spin-orbit doublet component, $2\Pi_{1/2}$ or $2\Pi_{3/2}$ (denoted as F_1 or F_2 respectively) are further split into two symmetry-adapted parity states, *e* and *f,* due to the very weak interaction between the orbital angular momenta and the nuclear rotation. Such splittings are called Λ-type doublings [Ale88].

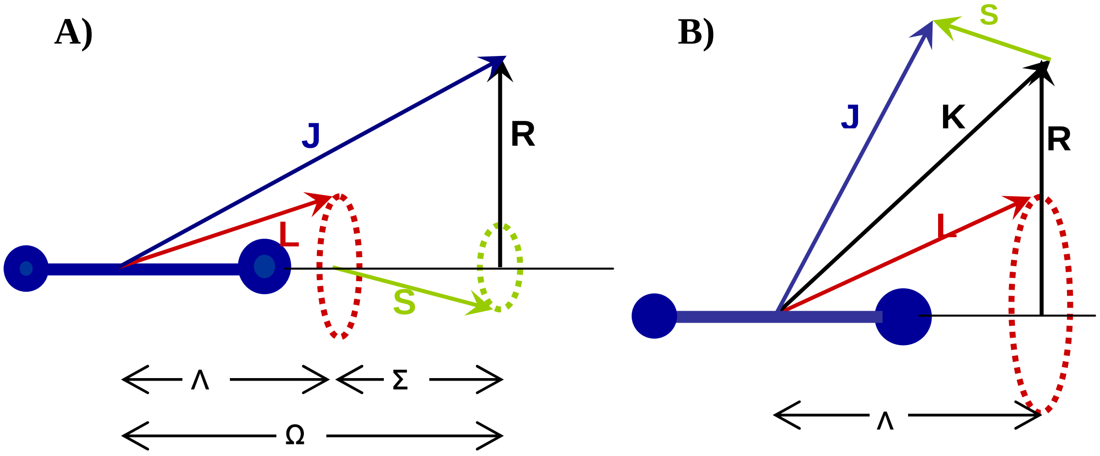

Figure 2.8.: Schematic view of A) Hund's Case (a), where the strong axial electric field along the internuclear axis causes the total electron orbital (L) and spin angular momenta (S) to process rapidly about the internuclear axis. The components of these angular momenta along the internuclear axis gives a quantum number Ω, and this couples with the rotational angular momentum of the molecule (R) to form a resultant, ***J*** and B) Hund's case (b) spin-orbit coupling is no longer strong enough to couple **S** to the internuclear axis and together with the rotational angular momentum **R** this forms a resultant **K**. The total angular momentum **J** is obtained from the vector addition **K** + **S** [Ell05].

For high *J* states, a progression to Hund's case (b) occurs. In Hund's case (b), shown in figure 2.8 b, the projection of total angular momentum couples to the nuclear angular momentum to give the angular momentum *K,* and then *K* couples to the total spin *S* to give the total angular momentum *J"*. The electronically excited state $A^2\Sigma$, used in our experiments for NO detection, is produced by excitation of the unpaired $2\pi^*$ electron to the Σ orbital which has $\Lambda = 0$. Therefore Hund's case (b) is relevant in the excited state $A^2\Sigma$. The excited electronic state $A^2\Sigma$ is also split into F_1 and F_2 components, corresponding to the *e* and *f* parity. The coupling of the spin and rotational angular momenta in Hund's case (b) results in the degeneracy of the two parity states in the $A^2\Sigma$ state.

The dipole selection rule for transitions between rotational, spin orbit and lambda doublet states for the $A^2\Sigma \leftarrow X^2\Pi$ electronic transition is $\Delta J = J' - J'' = 0, \pm 1$. However the dipole selection rule does not place any restrictions on the vibrational transitions (*v'*, *v"*).

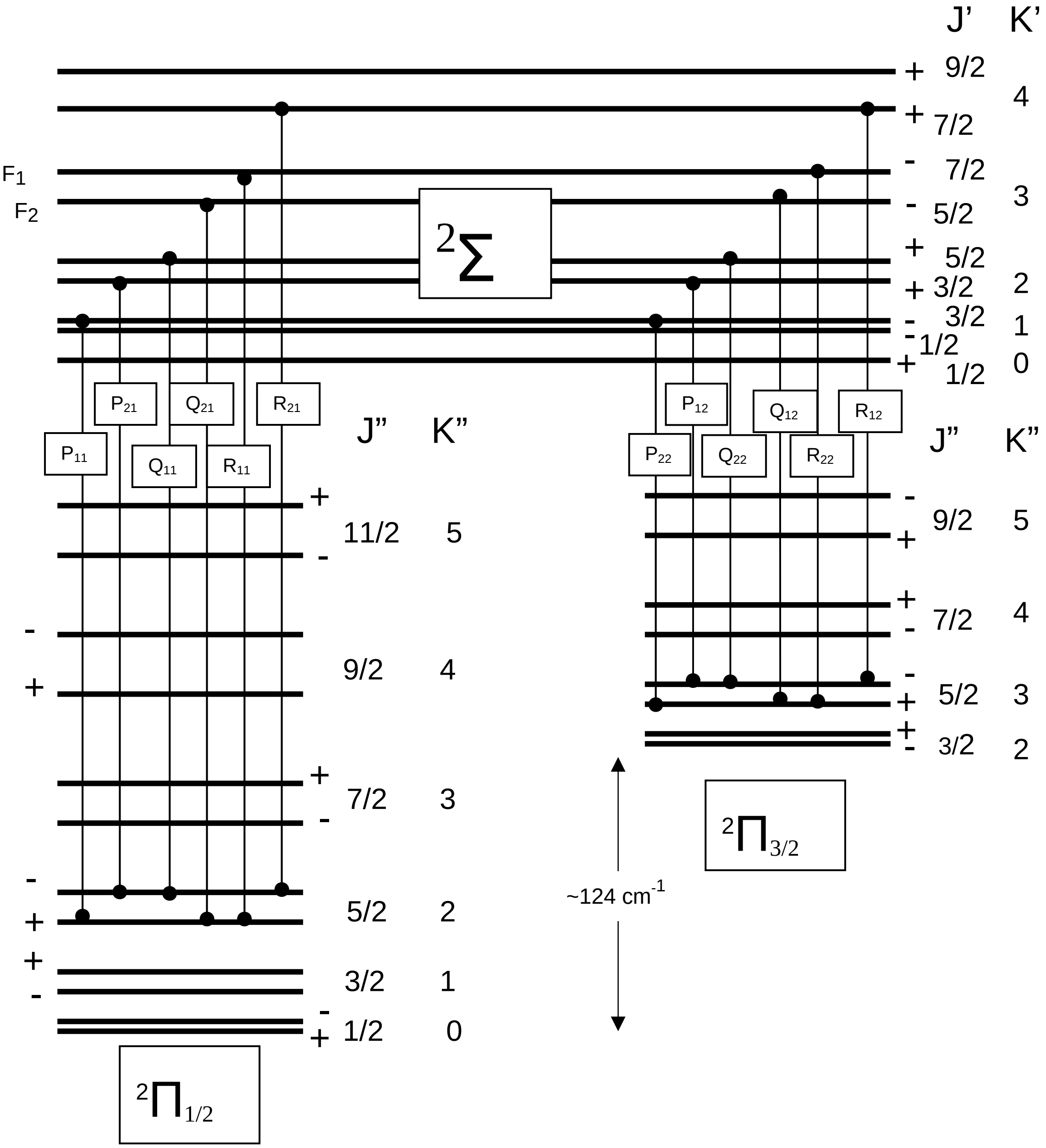

Figure 2.9.: Schematic of energy levels and transitions of NO [Her50].

The positions of the transition energies for *v* and *J* of the absorption spectrum of NO ground and first excited states can be calculated using the equations listed in Table 2.1.

Table 2.1: Formulae used to calculate the energy levels of transitions in NO [Gar82].

$X^2\Pi_{3/2,1/2}$	$T(v',J') = G(v') + F(v',J')$ $G(v') = 1904.405(v'+\tfrac{1}{2}) - 14.187(v'+\tfrac{1}{2})^2 + 0.0240(v'+\tfrac{1}{2})^3$ $F_{1,2} = B(v')\left[(J'+\tfrac{1}{2})^2 - 1 \mp \tfrac{1}{2}\sqrt{\lambda(v')^2 - 4\lambda(v') + 4(J'+\tfrac{1}{2})^2}\right]$ $\lambda(v') = \dfrac{A(v')}{B(v')}$ $A(v') = 123.26 - 0.1906(v'+\tfrac{1}{2}) - 0.0108(v'+\tfrac{1}{2})^3$ $B(v') = 1.70427 - 0.01728(v'+\tfrac{1}{2}) - 0.000037(v'+\tfrac{1}{2})^2$
$A^2\Sigma^+$	$T(v'',J'') = T_e + G(v'') + F_i(v'',J'')$ $T_e = 43906.37$ $G(v'') = 2374.307(v''+\tfrac{1}{2}) - 16.106(v''+\tfrac{1}{2})^2 - 0.04645(v''+\tfrac{1}{2})^3$ $F_1(v'',J'') = B(v'')(J''-\tfrac{1}{2})(J''+\tfrac{1}{2})$ $F2(v'',J'') = B(v'')(J''+\tfrac{1}{2})(J''+\tfrac{3}{2})$ $B(v'') = 1.99478 - 0.018328(v''+\tfrac{1}{2})$

The $A^2\Sigma \leftarrow X^2\Pi$ transition of NO has twelve rotational branches for each vibrational band (see figure 2.9). These branches are: the main branches, P_{11}, P_{22}, Q_{11}, Q_{22}, R_{11}, R_{22}, and the satellite branches, P_{12}, P_{21}, Q_{12}, Q_{21}, R_{12} and R_{21}. The letters P, Q and R correspond to $\Delta J = J'-J'' = -1, 0, 1$ respectively. The subscripts in the branches represent the total angular momentum, Ω, of the $A^2\Sigma$ and $X^2\Pi$ states, respectively. Main branches are from transitions $\Delta J = \Delta K$ and satellite branches are from $\Delta J \neq \Delta K$ transitions. The degeneracy of the two parity states in $A^2\Sigma^+$ states results in a complete overlap of transition energies of four satellite branches with four main branches: P_{21}+Q_{11}, Q_{21}+R_{11}, P_{22}+Q_{12}, and Q_{22}+R_{12}.

In this thesis work, we characterized the internal state population of NO photodesorbed from adsorbed NO dimers to obtain insight into the desorption mechanism.

The spectroscopic information of a REMPI measurement is carried in the first step of the transition $A^2\Sigma \leftarrow X^2\Pi$. As the laser wavelength scans across different rovibronic states of the $A^2\Sigma$ state, enhanced ion production is directly proportional to the corresponding transition probability. The absorption intensity of a given rovibronic transition, which is proportional to the ion signal measured by REMPI, is given by:

$$I = I_0 N_{v'',J} \left\langle v'/v'' \right\rangle^2 \left|\mathrm{Re}\right|^2 S_J\,, \tag{2.9}$$

where I_0 is the intensity of the incident radiation, $N_{v'',J}$ is the population in the given rotational and vibrational level, $<v'|v''>^2$ is the Franck-Condon Factor, $|Re|^2$ is the electronic transition probability, and S_J is the Honl-London factor. The overlapping branches start from the same levels of the ground states; therefore they will have the same initial state population. The only term that is different for the pair of overlapping branches in equation 2.9 is the Honl-London factor, S_J. Therefore during correction of the line intensities of the overlapping signals we have to divide it by the sum of S_J of the overlapping branches [Her50].

ii. Ion Detection

Following photodesorption, NO molecules drift into the probe laser path which is 27 mm away from the sample surface. They are then ionized in their quantum state by the probe laser, and the ion is accelerated towards the MCP by a repeller plate held at +1 kV.

$$NO\ X^2\Pi(v'',J'') \xrightarrow{\hbar\omega} NO\ A^2\Sigma(v',J') \xrightarrow{\hbar\omega} NO^+ + e^- \tag{2.10}$$

The ions then hit the MCP and are detected as ion current.

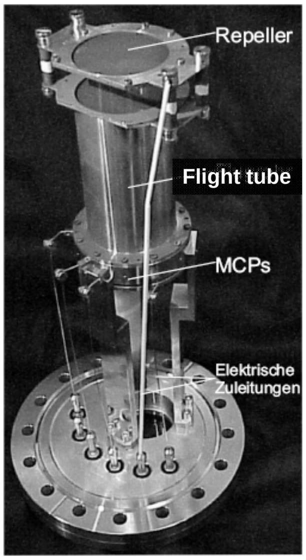

Figure 2.10.: the ionization and detection setup. It is composed of a repeller plate, a flight tube, and a microchannel plate (MCP) assembly (From ref. [Rak03].

iii. Data acquisition

For each data point the computer records the REMPI signal, the pump laser power and the probe laser power. The signal from the MCPs was amplified by two amplifiers (ORTEC VT120) and sent to the boxcar (SR 250). The boxcar was triggered by the desorption laser which was detected by the photo multiplier (PMT2). A small fraction of the pump and probe lasers were measured using the Ophir energy meter and the joule meter, respectively, throughout each probe laser scan. The output from Ophir was sent to the PC via USB (RS232) and the joule meter output was sent to another boxcar (SR 250). The last sample from the boxcar (ion signal) and the output from the probe laser power were sent to the ADC channels (National Instruments). The data was then transferred to the computer and stored for later analysis. After storing the data for the actual wave length, a TTL pulse was sent to the dye laser auto tracker to tune it to the next wavelength. For TOF measurements, the delay between the pump and probe pulses was controlled by a delay generator (DG 535) (see the experimental setup in figure 2.11).

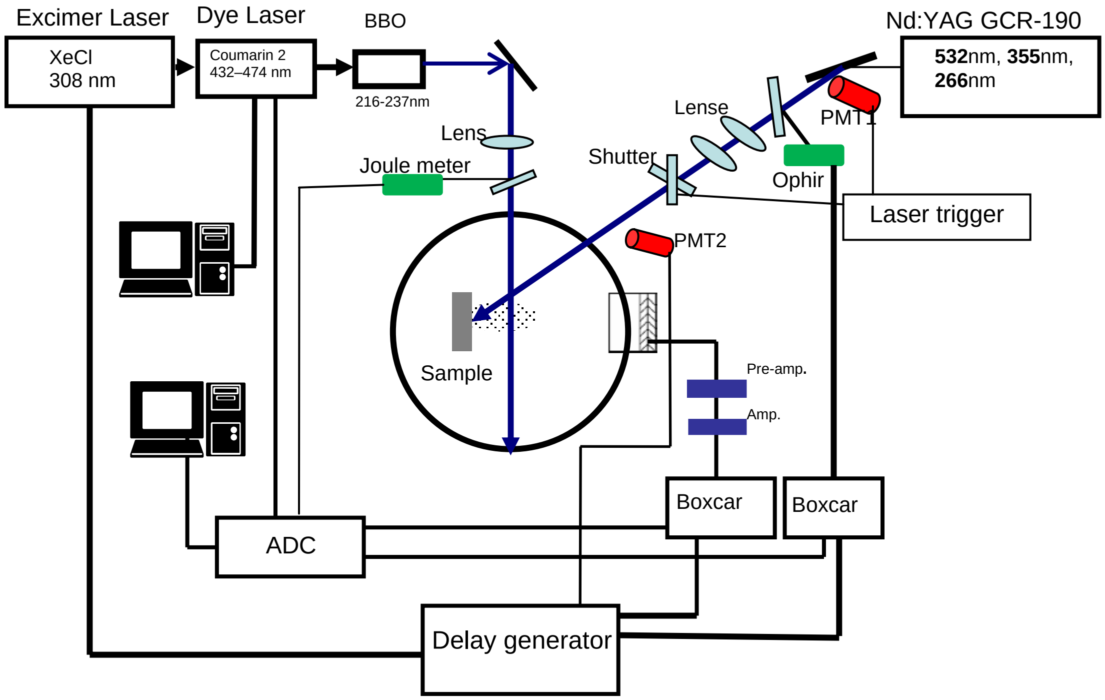

Figure 2.11: Schematic of experimental setup for REMPI measurements.

The experiments were performed by first recording the background (i.e., gas phase) NO REMPI signal, $I_{REMPI,off}$ for 20 shots (i.e., the shutter of PSD laser closed). Then, the shutter was opened so that the crystal was irradiated and the sum of desorption and background signals, $I_{REMPI,on}$ was recorded. After averaging $I_{REMPIoff}$ and $I_{REMPYon}$ separately for 2 to 5 cycles (depending on the measurement type), the averaged $\mathrm{I}_{\mathrm{REMPIoff}}$ signal was subtracted from the averaged $I_{REMPYon}$ signal and their difference *diff*(I_{REMPI}) was normalized by the pump and the probe laser intensities according to the power relation. The desorption yield of NO induced by nanosecond laser pulses from Ag surface is linear with the laser fluence. Therefore *diff*(I_{REMPI}) was normalized by dividing it by the pump laser intensity. However, due to the saturation effect of the REMPI transitions at higher probe laser powers [Jac86], the power dependence varies from linear to quadratic. In the REMPI spectrum measurements the probe laser intensity was kept in the quadratic region, see figure 2.12, (at low probe laser power) using the motorized filter wheel (FW-2000 Thorlabs). Therefore, *diff*(I_{REMPI}) was normalized by dividing by the square of the probe laser power. After completion of all these procedures, the pump-probe delay (TOF measurements) or the dye laser wavelength (internal state measurements) were changed to their next value to measure the next data point. A complete set of a labview program, developed by Prof. Kazuo Watanabe, was used for the REMPI measurements.

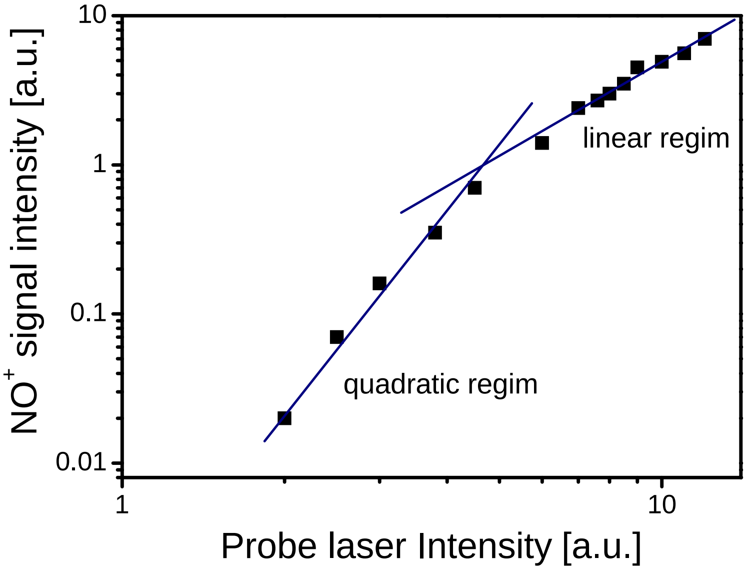

Figure 2.12.: Logarithmic plot of NO, in $v = 0$, $J'' = 11.5$, $\Omega = 1/2$ state, desorption signal as a function of the detection laser intensity.

iv. Determination of final state energy distributions

TOF spectra for individual internal quantum states were measured by varying the delay between the pump and probe lasers at a known rovibrational state. They were fitted to a *shifted* MB function, similar to those used for the QMS TOF spectra. Unlike the QMS TOF spectra, REMPI TOF spectra need no ion drift time subtraction. Moreover, unlike the internal state analysis (discussed below), the intensity of the TOF spectra need not be normalized to Honl-London factors (S_J) or Franck-Condon factors.

The translational energy can be measured by calculating the sum of flux weighted translational temperatures at each J and v levels.

To obtain the rotational population distributions for the $v = 0$ or $v = 1$ state, first we assigned the observed transitions in the measured REMPI spectrum based on the simulated spectrum. The simulated spectrum and the relevant Honl-London factors (S_J) could be taken over from work of a previous PhD student, Christoph Rakete. The determination of the rotational temperature was performed then by dividing each transition peak intensity (I_J) by the Honl-London factors and the degeneracy of the initial state $(2J+1)$. In the case of overlapping branches like, $P_{21}+Q_{11}$, $Q_{21}+R_{11}$, $P_{22}+Q_{12}$, $Q_{22}+R_{12}$ the experimental intensities were divided by the sum of the Honl-London factors of the overlapping branches. The resulting relative populations were then plotted in a Boltzmann plot i.e., $ln[I_J/((S_J).(2J+1))]$ *vs*. $J(J+1)$

If the plot is linear, the slope of the fitting result of the Boltzmann plot is inversely proportional to the equivalent rotational temperature of the molecule.

$$\ln\left(\frac{I_J(T)}{2J+1}\right) = -\frac{E_J}{k_B T}, \tag{2.12}$$

where, $E_J = B\,J(J+1)$ and B is a rotational constant

For the determination of rotational temperature, six different branches (three from spin 1/2 state and three from spin 3/2 state) namely: R_{21}, $Q_{21}+R_{11}$, $P_{21}+Q_{11}$, R_{22}, $Q_{22}+R_{12}$, $P_{22}+Q_{12}$ were analyzed. The rotational temperatures for each branches were determined independently and finally averaged.

To check the accuracy of our measurements, normalizations and analysis, we have performed a gas phase NO REMPI measurement and determined the rotational temperature from the Boltzmann plot. Figure 2.13 shows results of such measurements based on four different branches of the NO $A \leftarrow X$ spectrum for ambient NO gas at a pressure of $1\text{x}10^{-7}$ mbar NO at room temperature obtained using the above procedure. The measurement is clearly well described by a straight line, as expected for Boltzmann distribution and the slope is consistent with a temperature of 303 K which confirms the accuracy of our measurement, normalization and analysis procedures.

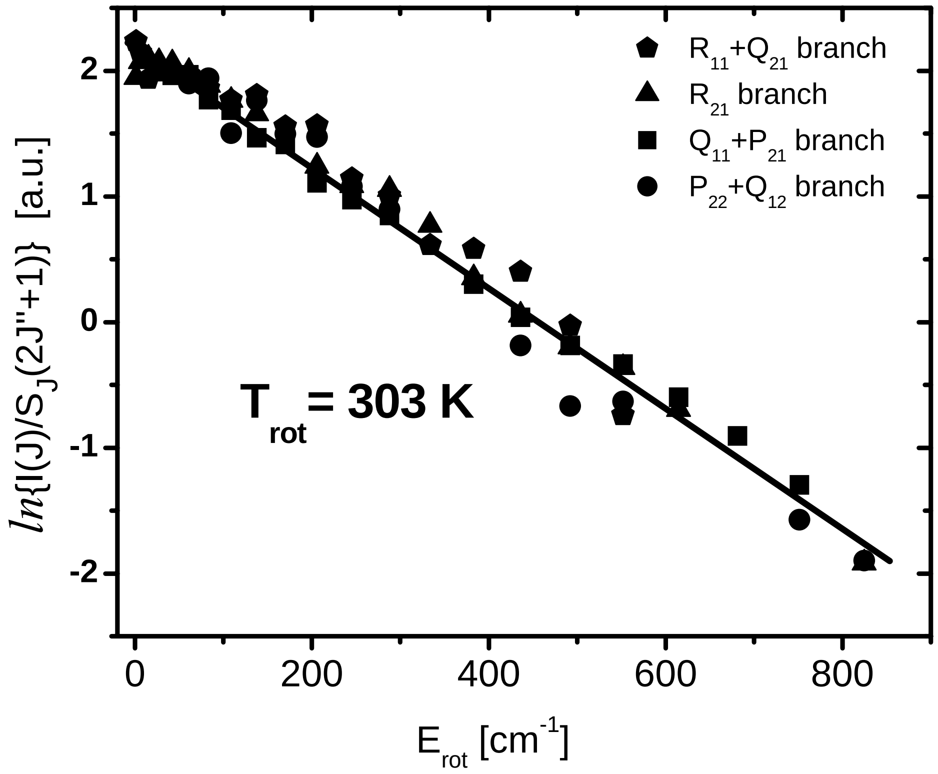

Figure 2.13.: Rotational energy distributions of ambient NO ($v = 0$) at a background pressure of ~1x10^{-7} mbar.

Chapter 3

Size effects on the adsorption and reaction of NO on Ag NPs

This chapter provides results concerning the effects of particle size on the adsorption and subsequent thermal and/or photon induced reaction kinetics of NO on alumina supported Ag NPs of diameter between 2 and 12 nm. The first section provides basic concepts on thermal and photoinduced reactions of molecules adsorbed on flat and particulate metal surfaces which are relevant for the understanding and interpretation of our results. The experimental results and their detailed discussions are presented afterwards. The adsorption energy and branching ratios of NO and N_2O formed from thermal reactions of NO dimers adsorbed on Ag NPs were found to vary with particle size. Furthermore, photoinduced reactions of NO dimers show complicated behavior with varying NP size and photon energy. Especially, for resonant excitation of Mie plasmons at 3.5 eV a strong enhancement of the PCS, maximal for an intermediate nanoparticle size, was observed. At non-resonant photon energies (2.3 and 4.7 eV) on the other hand, a moderate enhancement of PCS which scales linearly with 1/R was observed. We discuss these changes in terms of the size dependence of electronic and geometric effects, plasmon strength and decay paths, and the confinement effect. Finally, a summary of the results is presented at the end of the chapter.

Keywords: Ag NPs, (1 0) Mie plasmon, NO dimers, NO monomers, thermal reaction, photodesorption cross-section, TPD, MS-TOF.

3.1. Introduction

One of the desired goals of studying thermal and photochemistry of molecules adsorbed on metals is to inspect to what extent the presence of the substrate affects the adsorbate chemistry as compared to the gas phase chemistry. At small nanoparticles, due to their special physical and chemical properties, the chemistry of molecules is expected to differ from their bulk counterparts. However, very little is known about the adsorption and reaction of molecules at nanostructure surfaces. This section presents literature overviews which are relevant for understanding and interpretation of our experimental results on the size dependent thermal and photo reaction kinetics of NO adsorbed on Ag NPs.

3.1.1. Thermal chemistry of NO on metal surfaces

There is a vast amount of accumulated knowledge about the thermal chemistry of NO on well defined metal surfaces both from the point of view of a fundamental as well as technological approach. Fundamentally because NO is simpler for spectroscopic measurements, and technologically because it is a major component of air pollutants. Therefore, catalytic reduction is important, for example in the automobile three way catalyst.

Because of the presence of unpaired electrons in its $2\pi^*$ molecular orbital, NO adsorbs on metal surfaces by donating (or accepting) electron density to (or from) the surface. For this reason it shows a variety of adsorption structures and chemistry on the surface [End00]. For example, no reaction of NO with Ag (111) surface is observed at room temperature [Gat94]; however, it is more reactive at low temperatures. Spectroscopic studies have shown that at low surface temperature NO molecules tend to pair up and form NO dimers on Ag (111) surfaces [Bro95, Bro95[a], Lud93, Car01]. The driving force for the NO dimerization on the Ag (111) surfaces was demonstrated in a DFT calculation [Jig99]. The calculation shows that when NO adsorbs on the Ag (111) surface, it retains 90% of the spin density of the free molecule, i.e., it retains its unpaired electron in the $2\pi^*$ orbital. When two NO molecules are adsorbed in adjacent sites, the NO loses its spin density and an $(NO)_2$ dimer is formed. Hence, the presence of the unpaired electron in the $2\pi^*$ orbital of NO affects its chemistry and allows it to dimerise on a surface. NO dimers chemisorb on Ag (111) surfaces through charge transfer from 5σ in to the metal and back donation from the metal d band to the π type orbitals of the NO dimer, $7A_1$ [Jig99]. The orientation of a monolayer of NO dimers adsorbed on the Cu (111) surface has been investigated using the IRAS surface selection rule, suggesting that NO dimers are adsorbed in the "Ushaped" geometry with the N – N bond parallel to the surface [Kim02]. A similar orientation of NO dimers adsorbed on Ag (111) surfaces was found by Brown etal [Bro95] using RAIRS and NEXAFS. Furthermore, comparisons of the calculated geometry of NO dimers in the gas phase and on Ag surfaces showed an extension of the N – O bond and shortening of the N – N bond as a result of adsorption on the Ag (111) surface [Mat05].

The dimerization process has been suggested to be the precursor for N_2O formation upon heating [Car01]. Decomposition of NO dimers to metal-bound atomic oxygen and N_2O occurs at a temperature above 77 K on Ag (111) [Bro95, Car01, Lud93]. The peak desorption temperature of the reaction product, N_2O, is observed at ~ 120 K [Bro95]. An additional pathway for N_2O formation on single crystal Ag at 80 K was noted by So, et al. to be through dissociative chemisorptions of NO followed by surface mediated reaction between the surface bound N and NO [So89].

Due to their reduced dimensionality, MNPs exhibit striking structural and electronic properties, which deviate considerably from the corresponding bulk behavior. Particularly for MNPs of size below 10 nm, their geometrical and electronic properties depend strongly on the particle size. The chemical reactions occurring on their surfaces were shown to be also size dependent. For example, small Ag nanoparticles (100 to 300 atoms) are more active to dissociate molecular oxygen to atomic oxygen than their bulk counterparts in the temperature range 80 to 300 K [Rao92]. Moreover, unlike to bulk gold, Au nanoparticles show a significant size effect in their ability for the CO oxidation reaction [Val98]. Furthermore, an anomalously low adsorption energy of CO on very small Pd particles on Fe_3O_4 was observed [Sch07]. The strong modification of adsorption behavior of the small particles was explained based on strong interfacial interactions of small Pd particles with the Fe_3O_4 substrate. A recent direct calorimetric measurement of the heat of adsorption of CO on Pd NPs on Fe_3O_4 in the size range between 2 and 8 nm (and also on the Pd (111) surface) shows a decrease of the initial heat adsorption of CO with decreasing size [Fisxx]. These and other previous studies addressed various suggestions for the observed size dependent reactivity of nanoparticles. Some of them are for example; the presence of multiple low coordinated atoms, interfacial interaction with the support and corresponding charge transfer, and the special confinement that results in quantum size effects [Val98, Hei99, Che06, Zha07]. In addition, effects of the oxidation states of the metal atoms, influences of charge, and ionization potentials on the reactivity of MNPs have been presented. However, so far no systematic study was available on the adsorption and reaction of NO on such complex systems such as supported Ag NPs and therefore, little is known about how the nanoparticle size affects the interaction between NO and their surfaces. In this thesis work, effects of size on the adsorption and reaction of NO on supported Ag NPs have been studied by using TPD, as presented in section 3.3.1.

3.1.2. Photochemistry of NO on metal surfaces

Photoinduced chemical reactions on metal surfaces are among the most interesting effects in surface science [Dai95]. Photochemistry of molecules in the adsorbed state is often completely different from that found in the gas phase. In particular adsorbate photochemistry is observed at wavelengths where the free molecules are transparent. Previous studies on the photochemistry of molecules adsorbed on metal surfaces have shown that because of the rapid relaxation of the excitation energy in the molecule, photochemistry is induced through negative ion states accessed through substrate mediated molecular excitations, which result from photon absorption by the metal substrate. Despite of the rapid relaxation of the excitation energy, a number of molecules on metal surfaces have been found to show a variety of photochemical processes upon irradiation with photons.

The photoreaction of NO on Ag (111) surfaces has been studied theoretically [Nak06, Mat05, Rod90] and experimentally [Nat88, So91, Fra90, Kid96, Kid99, Kid00]. It is generally believed that photoreactions of NO are induced by hot electrons generated in the substrate, Ag (111), that are able to access the NO resonance ($2\pi^*$) state and ultimately cause reaction. The cross section of such photochemical processes depends on the generation of electrons resulting in photon absorption by the Ag substrate and the efficiency of these electrons to reach the Ag surface and tunnel into the NO resonance state. Therefore, the overall photoreaction efficiency depends on the excitation efficiency, the fraction of excited electrons reaching the surface, the tunneling and attachment probability of the excited electrons to the NO resonance state, and their lifetime in the resonance state [Pal92]. Enhancement of the photoreaction cross sections were observed by modifying the surface, e.g., by roughening the surface [Kid96, Kid00, Myl95, Gon84], compared to bulk single crystal surfaces. The origin of such enhancement was discussed based on plasmon excitation on the roughened surfaces which is not the case for smooth surfaces.

Owing to unique physical and chemical properties, photoinduced reactions occurring on MNPs surfaces are expected to differ from those found from bulk crystals. In MNPs, which are smaller than the mean free path of electrons at the Fermi edge, electronic excitations are confined. This confinement effect can lead to an enhancement of photoreactions on MNPs compared to those on surfaces of bulk materials [Zhd04]. For example, the photodesorption cross-section of NO molecules photodesorbed by ns UV light from amorphous or Pd NPs of diameter 0.5 – 8 nm on alumina surfaces increases with decreasing the particle size over at least 1 order of magnitude [Kam02, AlS06]. In addition, the excitation of the Mie plasmon, the collective motion of conduction band electrons of MNPs, has been implicated in enhancement of photochemical processes on MNPs. However, very few experimental studies regarding plasmon effects on photochemistry have been performed so far. Wettergren et al. [Wet05] observed both the effects of size and plasmon induced enhancement of NO photodesorption yield for rather large Ag NPs grown on HOPG substrates. In many cases the important parameter for plasmon induced enhancement of photochemistry is believed to be the field enhancement near the nanoparticle surface. However, recently a direct influence of plasmon excitation for non-thermal photodesorption of Xe on supported Ag NPs was reported [Wat06]. In small metal nanoparticles the electron relaxation rate is slower; this may also increase the reaction probability of adsorbates on their surfaces.

Mie plasmon on Ag NPs on Al_2O_3 films on NiAl (110)

According to STM results oblate shape Ag nanoparticles with aspect ratio of about 1.7 can be grown by deposition of Ag atoms on thin alumina films on a NiAl (110) substrate. Their optical properties have been examined by photon-STM [Nil00] and 2PPE [Eve05] measurements. In the former case electrons injected from an STM tip were used to excite a Mie plasmon on individual particles and the radiative de-excitation of the Mie plasmon was measured.

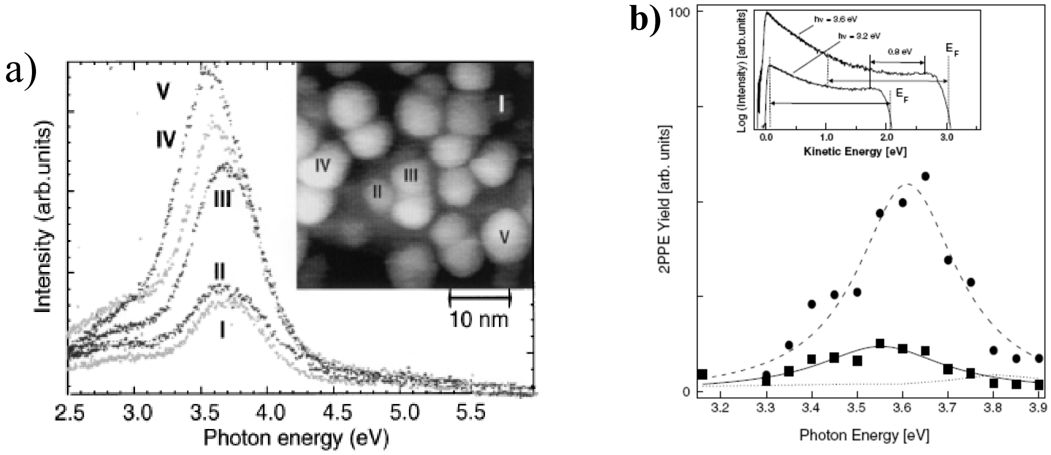

Figure 3.1.: (a) Photon emission spectra from single Ag NPs on Al_2O_3/NiAl (110) surface. Photon emission spectra of differently sized Ag nanoparticles are shown. The inset shows the corresponding STM image. (b) Photon energy dependence of the 2PPE yield of Ag NPs. The inset shows 2PPE spectra of Ag NPs of approximately 10 nm diameter at *hv* = 3.2 and 3.6 eV. The arrows indicate the width of integration and peak shift. Reprinted with permission from ref a) [Nil00] and b) [Eve05]. Copyright a) 2005 Elsevier b) 2000 APS.

As can be seen from figure 3.1a, the (1,0) Mie plasmon resonance energy of Ag NPs is peaked around 3.6 eV and slightly blue-shifted with decreasing size. The possible coupling of the Mie plasmon resonance to the next neighbor NP is not that much significant at the actual particle density of some 10^{-11} cm^{-2} of our nanoparticles [Dra02].

In the two-photon photoemission experiment, a first pulse excites an electron from below the Fermi level to an empty bulk or surface state, and the second pulse probes the transient dynamics in this state by exciting it above the vacuum level, where it can be emitted and detected. Figure 3.1b shows the photon energy dependent 2PPE yield of Ag NPs. The solid circles and solid squares represent total and partial integrations over the 2PPE yield, respectively. The solid and dashed curves indicate Lorentzian fits. The dotted curve shows the total 2PPE yield of Ag (111). At *hv* = 3.6 eV in *p*-polarization (*on-plasmon resonance*) the electron emission intensity from Ag nanoparticles is enhanced compared to at *hv* = 3.1 eV (which is in the foot of the resonance) [Eve05]. The results from the above measurements clearly show that the Mie plasmon resonance of Ag nanoparticles can be excited by 3.5 – 3.6 eV *p*- polarized photons.

In section 3.3.2, a detailed study on the effects of particle size and plasmon excitation on the photoreaction efficiency of NO dimers adsorbed on Ag NPs is presented.

3.2. Experimental setup

The experiments presented in this chapter were conducted in the UHV system described in Chapter 2. Roughly oblate hemispherical Ag nanoparticles with mean diameter (*D*) of 2 to 12 nm (standard deviation of at most 30 %) were prepared by deposition of Ag atoms on thin alumina films grown on NiAl (110) substrates at room temperature. A sub-monolayer of NO dimers was formed on Ag NPs by dosing NO to saturation coverage at 75 K sample temperature. After saturation the sample was cooled further down to 40 K to suppress thermally induced desorption during photodesorption measurements. Information on the effects of the nanoparticle size on the thermal reaction kinetics of the adsorbed NO dimers were obtained by using TPD. The QMS, in multiple acquisition mode, was set to measure the partial pressures of NO (m/e = 30), N_2O (m/e = 44), NO_2 (m/e = 46), N_2 (m/e = 28), N (m/e = 14), O_2 (m/e = 32), O (m/e = 16), C (m/e = 12), and H_2O (m/e = 18) with a linear heating ramp of 0.5 K/s. And for photodesorption measurements, 2.3, 3.5 or 4.7 eV *p*-polarized light from a pulsed Nd-YAG laser was directed onto the NO dimer-covered surface at a 45 ° angle off normal. The typical laser fluence was 1-2 mJ/cm^2 and the pulse repetition rate was 10 Hz. Photodesorbed molecules were detected along the surface normal by another QMS with a liquid nitrogen cooled shroud, at a sample-ionizer distance of 19 cm. The signals at m/e = 30 (NO) were recorded simultaneously by two multichannel scalers (MCS) with dwell times of 0.8 μs and 2 ms triggered by a laser pulse, to obtain the TOF distributions, which will be presented in *Chapter 4*, and shot dependences of the total PID signal, respectively. The shot dependent total PID yields were used to determine the desorption cross-sections of photodesorbed NO and will be presented later in this chapter.

3.3. Results and discussion

As mentioned above, so far there are no documented data about the adsorption characteristics of NO dimers on Ag NPs in the size regime we are interested in. Therefore results about the adsorption characteristics of NO dimers studied by TPD will be presented before the photodesorption results are discussed.

3.3.1. Thermal chemistry of NO on Ag NPs

The TPD experiments described in this section were performed to obtain some information regarding the adsorption characteristics of NO on various Ag NP sizes, in preparation for the laser experiments.

Figure 3.2 shows the typical thermal desorption spectra measured following saturation coverage of NO on 10 nm Ag NPs at 75 K and subsequently cooling down to 40 K. Two major desorbed species, namely NO (m/e = 30) and N_2O (m/e = 44) and their cracking patterns N, O, N_2, NO, etc appear in the spectra. NO (m/e = 30) desorbs at two major adsorption sites assigned as α- and β-, with desorption maximum at ~88 K and ~240 K respectively; whereas N_2O (m/e = 44) form a major desorption maximum at ~109 K. In addition, a small N_2 (m/e = 28) desorption, peaked ~140 K, was detected. As this temperature is far from that of the N_2O peak (~109 K) it cannot be a cracking fragment of N_2O at the QMS ionizer. It should be noted that, with the same experimental procedure, none of the above desorbed species was detected on bare alumina films. This rules out the possible contribution of desorbed species from the supporting alumina film.

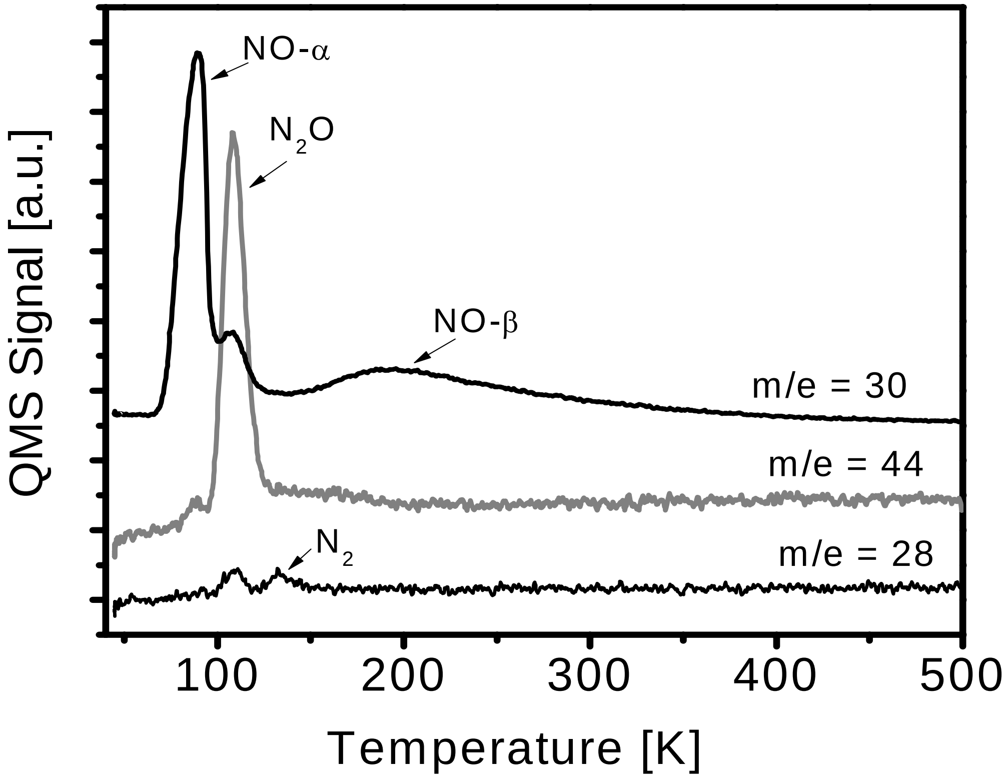

Figure 3.2.: TPD spectra from Ag NPs (*D* = 10 nm) dosed with NO to the saturation coverage at 75 K.

The presence of various species and multiple desorption peaks of NO indicate that the adsorption and reaction of NO on Ag NPs is a complicated process. In view of the dominating desorption maxima and their relative intensity distributions, the TPD spectra from Ag NPs partly resemble those from single crystal Ag (111). However, the spectra in Ag NPs are broader and the peak temperature positions are shifted to lower values compared to that of from Ag (111) surface.

On the basis of the Ag (111) studies, the following possible thermal reaction schemes for NO adsorbed on the Ag NPs surface have been proposed:

$$
\begin{aligned}
&NO_{(a)} + NO_{(a)} \underset{at\ low\ T}{\overset{on\ Ag\ NPs}{\rightarrow}} (NO)_{2\,(a)} \xrightarrow{heating} 2NO_{(g)or(a)} && \cdots Scheme-1 \\
&\qquad\qquad\qquad\qquad\quad \xrightarrow{heating} N_2O_{(a)or(g)} + O_{(a)} && \cdots Scheme-2 \quad (3.1) \\
&\qquad\qquad\qquad\qquad\quad \xrightarrow{heating} N_2O_{(a)or(g)} \rightarrow N_{2\,(a)} + O_{(a)} && \cdots Scheme-3 \\
&\qquad \xrightarrow{on\ Ag\ NPs} N_{(a)} + O_{(a)} + NO_{(a)} \xrightarrow{heating} N_2O_{(a)or(g)} + O_{(a)} && \cdots Scheme-4
\end{aligned}
$$

where, the subscripts *(a)* and *(g)* denote adsorbed and desorbed species respectively.

The low temperature (~88 K) NO desorption peak, labeled as NO-α, from Ag NP appears at lower temperature and with a similar profile to the corresponding low temperature desorption peak from Ag (111). This points to a common species i.e., originated from $(NO)_2$ dimer dissociation and monomer desorption (*schem-1)* competing with other reaction schemes mentioned in equation 3.1. In addition, a second NO desorption peak (NO-β), which shows a broad feature peaked at around 240 K, is observed. Pure NO monomers are unlikely as they should energetically be formed at low NO coverage at intermediate temperature and be weakly bound. The fact that we observed a NO desorption peak at higher temperature is more likely due to stabilization of monomers formed by dimer dissociation (*Schem-1*) by co-adsorbed $O_{(a)}$ formed from reaction *scheme-2*. When these O-stabilized monomers desorb as NO-β, the $O_{(a)}$ left behind probably dissolves in the Ag NPs, as no desorbing oxygen is observed (see below). The N_2O (m/e = 44) which has a desorption maximum at ~109 K is believed to be formed from the reaction of NO dimers (*scheme-2*) and stabilized by co-adsorbate $O_{(a)}$. It should be noted that this N_2O desorption peak temperature is larger than the desorption peak temperature observed for N_2O adsorbed on the clean Ag (111) surface (~85 K) and N_2O adsorbed on oxygen pre-adsorbed Ag (111) surface (~95 K) [Lud93]. The very small desorption signal at m/e = 28 (N_2) was observed at ~140 K, may arise from some partial dissociation of adsorbed $N_2O_{(a)}$ to $O_{(a)}$ and $N_{2(g)}$ (*Scheme-3*) during elevation of surface temperature. Efforts were made to detect O atoms. However, neither atomic nor molecular oxygen were detected in the gas phase in the temperature range between 40 and 700 K. As mentioned above, it is likely that O is dissolved in the Ag NPs upon heating.

The size dependence of desorption peak temperatures and integrated yields of the thermal reaction products of NO dimers on Ag NPs were further investigated; they are presented in the following.

i. Size dependent thermal chemistry of NO on Ag NPs

The absolute adsorbate coverage on the various Ag NP surfaces was estimated by calculating the total number of adsorbed N atoms from the integrated TPD peak areas. Cracking patterns of the desorbed molecules and the QMS relative sensitivity were also taken into account. Figure 3.3 shows the total number of adsorbed *N* atoms, which corresponds to the total initial adsorbate coverage, as a function of particle diameter, *D*. The variation of the surface coverage with particle diameter can be well fitted by a quadratic function. This quadratic relation between the total number of N atoms and surface area (~ R^2) of the Ag NPs suggests the proportionality of the initial saturation adsorbate coverage with the NPs surface area.

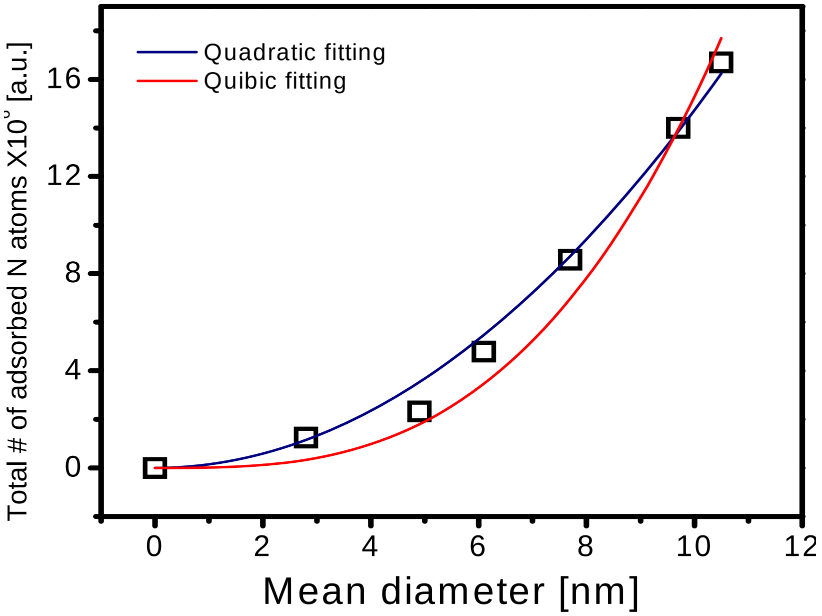

Figure 3.3.: The total number of adsorbed N atoms as a function of mean particle diameter. The solid lines are fittings of the data points with quadratic (blue) and cubic (red) laws.

Desorption energy and branching ratios of NO-α and N_2O

Desorption energy: Figure 3.4a depicts size dependent TPD results of m/e = 30 (NO-α) from Ag NPs exposed NO to saturation coverage at 75 K and subsequently cooled down to 40 K. The TPD results for the Ag (111) single crystal surface (dashed line) are also shown for comparison. The peak temperature, at which the desorption rate is maximum, continuously decreases with decreasing nanoparticle size (95 K for Ag (111), 89 K for D = 10.5 nm to 64 K for D = 2.8 nm Ag NPs). In addition the desorption of NO-α begins at around 65 K except for D = 2.8 nm which is 10 K lower. It should be noted that, at 75 K dosing temperature, the NO dimer coverage saturates as a sub-monolayer (roughly 90 % of a monolayer). Therefore, the possible reasons for the observed low temperature desorbed species could be due to post-dosing adsorption of residual NO gas in the time gap between dosing and TPD measurements (~20 min). This desorption signal below the dosing temperature could even be due to NO desorption from a small amount of second layer (2).

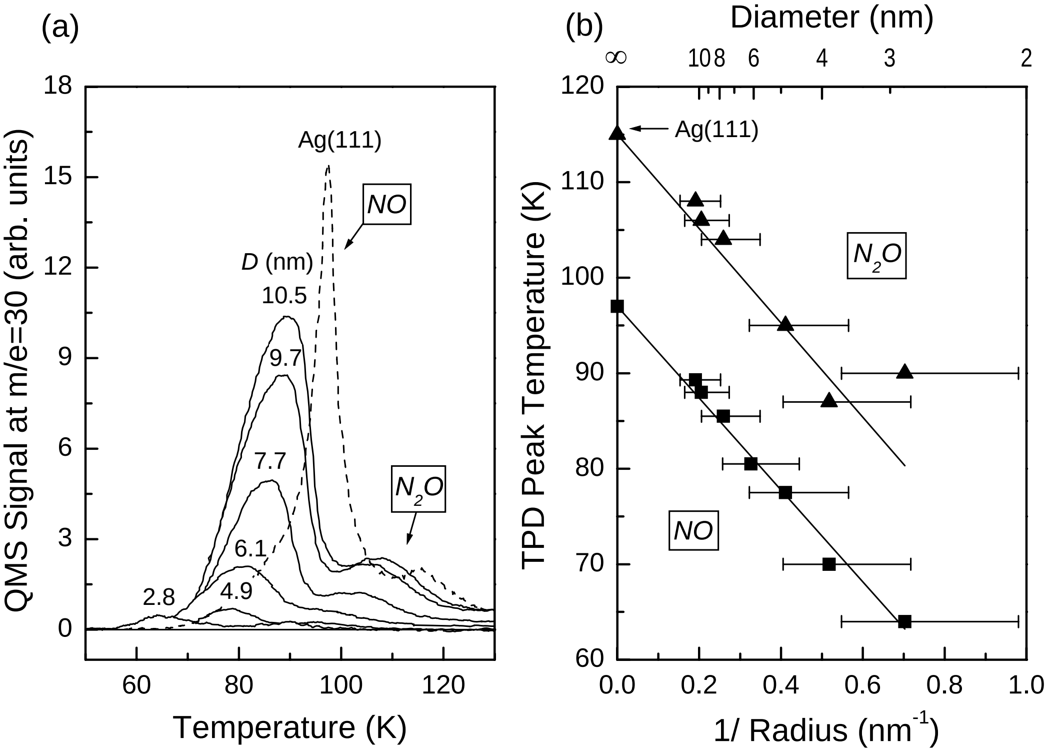

Figure 3.4.: a) TPD spectra of NO desorbed from Ag NPs of mean diameter between 2.8 and 10.5 nm dosed with NO to saturation coverage at 75 K at heating ramp 0.5 K/s. The TPD spectra measured from Ag (111) surface is also shown (dashed line) for comparison. b) Peak temperatures of NO (square) and N_2O (triangle) found in (a) are plotted as a function of (1/R).

---

(2) Since NO molecules are not mobile at low temperatures, a second layer can be formed before monolayer saturation has occurred.

Figure 3.4b shows plots of TPD peak temperatures of NO-α and N_2O as functions of 1/R including the data from Ag (111) (1/R = 0). The change of the peak desorption temperatures is almost linear with 1/R for both NO-α and N_2O species. In the simplest approximation, assuming order and pre-exponentials of desorption to be constant for varying particle size, the peak temperatures can be set proportional to the effective desorption energy.

But we in fact observe a complex process of NO dimers' dissociation and release of NO molecules into the gas phase, rather than simple desorption of adsorbed NO molecules. Therefore, the corresponding desorption energy, $E_{des,}$ will not be necessarily equal to the NO dimer or NO-α adsorption energy. Therefore, the observed change of peak temperature and the corresponding adsorption energy is linear only in the lowest approximation. On the other hand, the simple scaling for both species, dimer dissociation/monomer desorption and desorption of adsorbed N_2O, suggests the former is not a complicated process. Here we simply take the observed change of desorption peak temperature as a semi-quantitative indication for the adsorption energy for NO dimers (NO-α) and N_2O.

The possible origin for the observed results in our system, decrease of desorption energy with 1/R, can be discussed in terms of the electronic and geometric nature of the size effects of Ag NPs. It has been observed in many nanoparticle systems that the size induced modification of electronic and geometric structures could result in a size dependent reactivity of MNPs. In particular, the size induced modification of electronic structure due to quantum confinement of electrons results in a significant change on the reactivity of MNPs [Val98, Hei99, Zha07]. However, these effects are limited only to very small nanoparticle sizes and may not be observed in the NPs used in this work. According to the size dependent UV photoemission spectra by Apai et al. [Apa81], the onset of bulk Ag energy bands occurs at $D = \sim 2.2$ nm (~150 Ag atoms-Ag NPs) which is much smaller than the smallest Ag NP size used in this study ($D = \sim 2.8$ nm). Therefore, it is unlikely that these quantum size effects are observed in the size regime used in this work. Furthermore, according to XPS results, with reducing Ag nanoparticle size a shift of the *d*-band away from the Fermi level [Bal07] was found. Since NO dimer adsorption has some hybridization with the *d*-band, the shift may result in a weakened adsorption energy. The closer the *d*-band to the Fermi level, the larger the ability of the *d*-electrons to get involved in bonding through *d-sp* rehybridzation.

The size dependent work function or ionization potential of Ag NPs can change the way that they interact with the adsorbate. The work function of Ag NPs increases with decreasing size [Sch06]. Size dependent ionization potentials of isolated MNPs are also observed in many systems [Jor92]. In our system, since the molecules are weakly chemisorbed on the surface, some charge transfer between the adsorbate and the Ag NPs is expected. This charge transfer may behave similarly to the ionization potential/work function of the Ag NPs, which increases with decreasing the nanoparticle size. Therefore, the observed gradual decrease of the adsorption energy with 1/R could be connected to the size dependent change of the ionization potential/work function of the Ag NPs.

In addition, the possible size dependent van der Waals dispersion interaction between the adsorbate molecules and the Ag NPs should be considered. Previously the size dependent change of such interaction was suggested for the observed size dependent change of adsorption energy of methane physisorbed on Pd NPs [Wat99]. In our system, although NO dimers interact chemically with the substrate, van der Waal dispersion interaction could be still an important part of the adsorption energy. The density of electrons near the Fermi edge which is relevant for dispersion interaction changes with Ag NP size [Hov98]. Therefore, the observed weakening of the adsorption energy may be the result of such a reduction of electron population near the Fermi edge at smaller Ag NPs. Moreover, due to the smaller number of atoms present in smaller nanoparticles, the strength of the van der Waals interaction becomes smaller, since the latter sums essentially over all Ag atoms of the NPs. This leads to scaling with 1/R [Kre10]. Moreover, the possible change of the Ag surface states and the spill-out of the Ag surface *sp*-electrons with size of the NP may have their own contributions to the observed change of adsorption energy with particle size. The Ag surface states are expected to decrease with decreasing Ag NPs size. This may cause a weakening of the chemisorptive contribution of the adsorption energy which leads to the corresponding weakening of the adsorption energy of adsorbates. Furthermore, the increasing spill-out of the Ag surface *sp*-electrons for smaller NPs may produce a shift of the repulsive part of the surface potential to larger distance, and may reduce the adsorption strength of the molecules on their surface.

In addition to the size dependent electronic properties mentioned above, the surface geometric structure of Ag NPs may also play a role on the observed size dependence shift of adsorption energy. According to the STM results [Nil00], no significant change of the surface morphology of the Ag NPs was observed in the size regime used in this study. In addition, our TPD results showed neither significant change nor new adsorption states for both NO-α and N_2O with changing *D*. Furthermore, the onset temperature of NO-α desorption (~65 K) is independent of the Ag NP size except for the smallest Ag NP size, *D* = 2.8 nm, where it is about 10 K lower. However, in the latter case, the observed similarity of desorption onsets may be due to NO desorption from the second layer which is insensitive to the substrate (or particle size, *D*).

The desorption peaks from Ag NPs are substantially broader than those of Ag (111) surfaces. These may suggest the heterogenousity of the NP surfaces compared to the Ag (111) surface but the peak broadening may also arise from the inhomogenity of the NP size distributions. These arguments suggest an absence of significant size dependent geometrical changes of nanoparticles except possibly for the smallest size D = 2.8 nm (~600 Ag atoms).

On the other hand, unlike to NO-α, there is a gradual shift of the onset of the desorption temperature of N_2O to lower values with decreasing particle size. However, it should be noted that the adsorption energy of N_2O strongly depends on the nature of the co-adsorbates. For example on Ag (111) surface, the peak desorption temperature of N_2O formed from adsorbed NO dimers was observed at ~120 K [Bro95], however, N_2O adsorbed on clean Ag (111) surface desorbed at ~85 K and N_2O adsorbed on oxygen pre-adsorbed Ag (111) surface desorbed at ~95 K [Lud93]. This clearly suggests that the adsorption energy of N_2O on the Ag (111) surface strongly depends on the nature of the co-adsorbates. Therefore the observed shift of the onsets of desorption temperatures may not be due to the change of the surface morphology of Ag NPs with D since the possible changes of coverage (3) and/or adsorption structure of co-adsorbates, $O_{(a)}$ and NO-$\beta_{(a)}$, can also lead to shifts of N_2O desorption temperature.

However, the change of the bond length (Ag-Ag distance), with decreasing D can result in a significant change of adsorption energy of adsorbates on the NP surface as observed on CO/Pd clusters [Yud08]. On Ag NPs up to 2.7 % of lattice contraction, compared to bulk Ag, was reported at smaller nanoparticles, D = ~3.1 nm [Ber52]. Therefore, one possible reason for the observed decrease of adsorption energies of NO-α and N_2O with decreasing D can be the decrease of lattice constant with decreasing, D.

Geometrical confinement of reactions in a nanometer scale can affect also the nature of chemical reactions [San05]. In our system, despite the different nature of the desorption mechanism for NO-α and N_2O, both showed almost similar size dependences of the adsorption energy. This similarity may suggest the similarity of the reaction kinetics of both species. This could be due to geometrical confinement of reactions in the nanometer scale. In our case, desorption of both NO and N_2O may be more efficient on the boundaries than on top of the Ag NPs and this may lead to an increase of the overall desorption rate with decreasing NP size.

---

(3) But it should not always be true since the N_2O:O ratio should be 1. Therefore a change in oxygen coverage with respect to N_2O is not expected. But the relative distributions of N_2O and O could vary with size.

Branching ratios: As mentioned before, besides thermal desorption of NO molecules, additional thermal reaction products like N_2O and N_2 desorption are observed. The size dependent nature of these reactions can be seen in the relative product branching ratios of NO dimers. Branching ratios estimated from the ratios of integrated TPD peak areas, shows that the fraction of N_2O formation resulting from heating of the NO dimer covered surface increases by up to a factor of two with decreasing nanoparticle size. Moreover a relative decrease of NO-α species compared to NO-β species is observed with decreasing particle size.

From these observations it is clear that the activation energy for N_2O formation is lower for smaller nanoparticles. On Ag (111) surfaces, reaction of NO dimers to $N_2O + O$ starts above 77 K [Bro95, Car01, Lud93]. On smaller nanoparticles, these reactions may start at lower temperature, possibly even at or below 75 K, the preparation temperature. In addition during post-dosage cooling, some residual NO from the background may adsorb and form NO dimers and upon heating, during TPD measurements, additional N_2O and NO-β species could be formed. This can lead to the observed increased amount of N_2O and NO-β desorption, as compared to NO-α, at smaller nanoparticles. Therefore, the observed size dependent branching ratio of N_2O could arise from the size dependent N_2O formation temperature which decreases with decreasing size.

3.3.2. Photoreaction of NO dimers on Ag NPs

The NO desorption measurements were started after saturation coverage of NO at 75 K and subsequent cool-down to 40 K. The photodesorption was induced by irradiating the surface with 2.3, 3.5, or 4.7 eV photons. The desorbed NO molecules were monitored by a MS-TOF measurement during the laser irradiation. The remaining photoproducts on the surface were checked by TPD after finishing irradiation. Here the observations made on size dependent photon-induced reactions of NO dimers adsorbed on Ag NPs are presented.

i. Post-irradiation TPD

Irradiation of the NO dimer adsorbed on 8 nm Ag NPs with 2.3 eV photons (7000 shots of laser pulses, x 10^{15} photons/cm^2 per pulse) resulted in desorption of weakly bound NO-α species, leaving a small residual, as indicated by the loss of intensity from the comparison of pre- and post-irradiation TPD shown in figure 3.5. But, no further depletion of this species was observed upon prolonged irradiation. On the other hand, irradiation with 3.5 or 4.7 eV photons resulted in total depletion of the NO-α species. In addition, the NO-β species was also reduced (or totally depleted) by extended irradiation of the surface with 3.5 eV (or 4.7 eV) photons. As to N_2O, some reduction of the intensity (at 4.7 eV) and a slight shift of peak temperature to lower values (at 3.5 and 4.7 eV) has been observed on the post-irradiation TPD compared to the pre-irradiation TPD. This might arise from two reasons: the first can be the different kinetics or dynamics of the thermal and photo-induced reaction pathways for N_2O formation. Second, since the adsorption properies of N_2O strongly depend on the co-adsorbates, the reduction of co-adsorbates (NO-β $_{(a)}$ and/or O $_{(a)}$) due to photodesorption can result in weakening of N_2O adsorption. It is noteworthy that no desorption features representative of new possible photoreaction products are detected in the post-irradiation TPD. From the above observations, we concluded that the NO-α species is the most photoactive species to desorb from the surface.

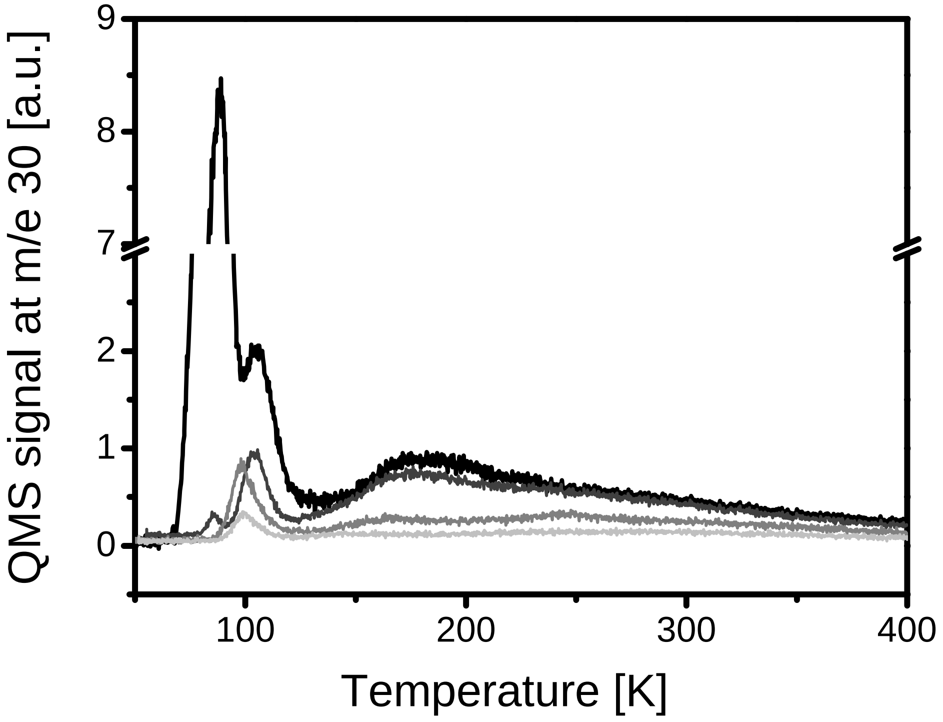

Figure 3.5.: Pre- and post irradiation TPD spectra of NO from 8-nm Ag NPs dosed with NO to saturation coverage at 75 K. Post irradiation TPD spectra are measured following irradiating the NO dimer saturated surface with 7000 shots of laser pulses at *hν* = 2.3 (dark gray), 3.5 eV (gray), 4.7 eV (light gray).

The photon induced desorption of NO is thought to occur via a substrate mediated mechanism so that the photochemical behavior is strongly affected by the MNP substrate and the negative ion state of the NO. A theoretical study by Nakamura and Yamashita [Nak06] showed that an empty negative ion state of NO dimers adsorbed on Ag (111) surface is around 2 eV above the Fermi level of Ag (111). In our case, one can estimate roughly the positions of the empty negative ion states of NO dimers adsorbed on Ag NPs based on the post-irradiation TPD results. A 2.3 eV photon energy can excite electrons which can sufficiently access the majority of the negative ion state of NO-α. On the other hand, 3.5 and 4.7 eV photon energies are sufficient to excite hot electrons with enough energy to access the TNI state of the NO-α species. From the above observations, the minimum photon energy required for excitation of electrons at the Fermi level to fully access the TNI state of NO dimers is estimated to be ~2.5 eV. The possible energy diagram of photoinduced electron transfer from near Fermi level Ag NP surfaces to the adsorbate $(NO)_2$ / NO-α and NO-β TNI states is shown in figure 3.6.

As mentioned above, it should be noted again that TPD is a destructive technique. The desorption species observed in post-irradiation TPD can be formed from thermal reactions of the remaining photoproducts on the surface when heated (during TPD measurements). Moreover, in this study we monitored only photodesorbed NO (m/e = 30) molecules, hence the possibility of new species formation and subsequent photodesorption from the surface could also have happened. In this study, we use post-irradiation TPD to identify the photo-active adsorption site(s)/species just by comparing the peak intensities with the pre-irradiation TPD spectra.

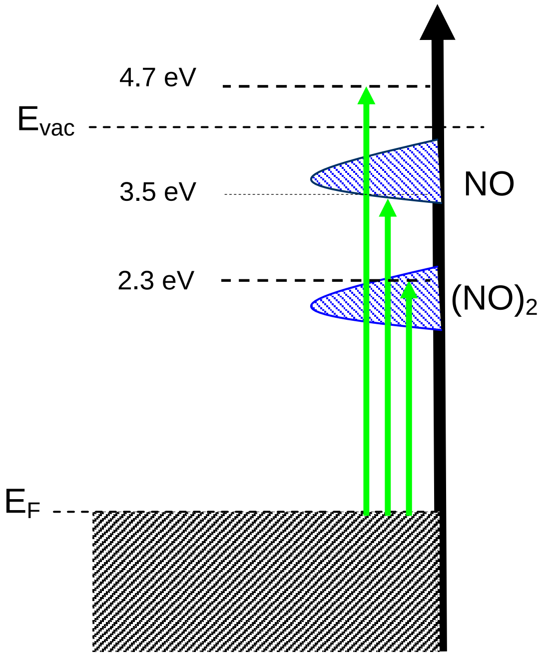

Figure 3.6.: Possible energy diagram for vertical electron transfer from near Fermi level Ag surfaces to adsorbate resonance state. The positions of the resonance states are estimated from the pot-irradiation TPD results.

ii. Size dependent photodesorption cross sections of NO-α

The depletion cross section for NO formed from the photodissociation of NO dimers has been determined. This process consists of photodissociation of NO dimers and release of NO molecules into the gas phase. Especially we are interested in the desorption cross section of NO-α species since they are the most photo-active species to desorb from the surface as judged from the post-irradiation TPD.

The photodesorption cross sections (PCS) of NO-α were determined from the decay of PID signal of m/e = 30 (NO) with time under continuous irradiation. The decaying signal reflects the decreasing coverage of the species which is the source of photodesorbed NO (most likely the dimer in the initial stages of decay) during laser irradiation and the cross sections can be determined from the decay constant, σ, by fitting the decaying signal with equation 3.2.

$$N = N_0 \, e^{-\sigma \cdot Ph} \quad , \tag{3.2}$$

where N_0, N, and Ph denote the adsorbates coverage before and after the desorption and the photon irradiance, respectively.

According to post-irradiation TPD, at photon energy 2.3 eV, only depletion of NO-α species was observed. Therefore, the cross-sections were determined by fitting the decaying signal with a single exponential function. On the other hand, at 3.5 and 4.7 eV photon energies, in addition to the desorption of NO-α species, desorption of NO-β species was observed. At these photon energies (3.5 and 4.7 eV), the semi-logarithmic plot, ln N/N_0 versus n_{ph}, of the decaying signal showed two distinct straight lines (see figure 3.7). The earlier, rapidly decaying signal, is ascribed to the depletion of dimers and the later, slow decaying signal, is ascribed to desorption of NO-β species. Hence, at these photon energies only the fast decaying part (~50 % of the decay) is used to obtain the PCS of NO-α.

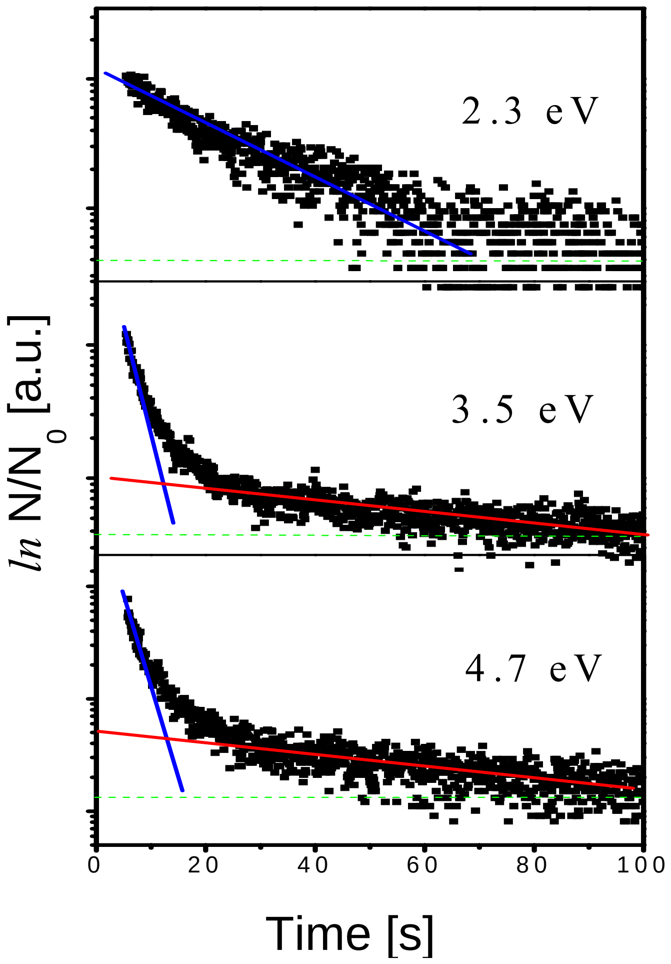

Figure 3.7.: Decay of PID signal upon irradiation of the NO dimer-covered Ag NP (*D* = 8 nm) with *hv* = 2.3 eV (top), 3.5 eV (middle), and 4.7 eV (bottom). The solid lines show a fitting of fast component, NO-α (blue line), and slow component, NO-β (red line).

The PCS of NO-α from NO dimers have been determined for various Ag nanoparticle sizes at $h\nu = 2.3$, 3.5, and 4.7 eV in *p*-polarization; they did show clear size and photon energy dependences. The data obtained are plotted as a function of 1/R in figure 3.8, including those of Ag (111) at 1/R = 0. The vertical error bar was estimated from the standard deviation of two or more measurements.

At 2.3 eV in *p*-polarization, the PCS increases from 5.4 x 10^{-19} cm^2 at Ag (111) to 2.9 x 10^{-18} cm^2 at $D = 11.1$ nm (1/R = 0.2 nm^{-1}) Ag NPs. The PCS increases monotonously with decreasing the Ag NPs mean diameter (D) up to the smallest nanoparticle particle D = 2.8 nm (1/R = 0.7 nm^{-1}). The PCS at D = 2.8 nm (1/R = 0.7 nm^{-1}) was ~ 6.5 x 10^{-18} cm^2 which is a ~12 fold enhancement compared to the Ag (111) result. Similarly at 4.7 eV (*p*-polarized), the PCS increases from ~1.6 x 10^{-17} cm^2 at Ag (111) to ~3.5 x 10^{-17} cm^2 at D = 11.1 nm Ag NPs (1/R = 0.2 nm^{-1}). And the PCS increases monotonously with decreasing D and becomes maximum (~9 x 10^{-17} cm^2) at the smallest particle size D = 2.8 nm (1/R = 0.7 nm^{-1}). Qualitatively similar size dependences of PCS i.e., an approximately linear scaling with the surface to volume ratio (1/R), was observed for both excitation photon energies. However, at 4.7 eV for a given size, the PCS was ~ 10 times higher than at 2.3 eV. This can be explained based on the effect of secondary hot electrons or primary hot electron cascades [Wei93].

On the other hand, at 3.5 eV (*p*-polarized), i.e., for plasmon excitation, the PCS increases from 4 x 10^{-18} cm^2 at Ag (111) to 2.1 x 10^{-17} cm^2 at 12 nm Ag NPs (1/R = 0.17 nm^{-1}), this corresponds to ~5 fold enhancement of PCS compared to Ag (111) results. Then the PCS increases dramatically with decreasing the Ag NP size up to D = 5 nm (1/R = 0.4 nm^{-1}). At D = 5 nm (1/R = 0.4 nm^{-1}) the PCS is ~1.7 x 10^{-16} cm^2 which is a ~43 fold enhancement compared to the Ag (111) result. However, with further decreasing of D below 5 nm, a fast decrease of the PCS is observed. At the smallest particle size, D = 2.8 nm (1/R = 0.7 nm^{-1}), the PCS is ~6.1 x 10^{-17} cm^2. This is about 15 fold enhanced compared to the Ag (111) result. At this photon energy unlike to the other photon energies, the expected 1/R trend is not observed over the entire size range. It should be noted that at 3.5 eV in *p*-polarization the Mie plasmon of Ag NPs is excited. Therefore, this unique trend observed at this photon energy and polarization should be related to Mie plasmon excitation. On the other hand, at largest and smallest nanoparticle sizes, the PCS enhancement factor is comparable to the observed PCS at similar D with non resonant photon energies, 2.3 and 4.7 eV excitations.

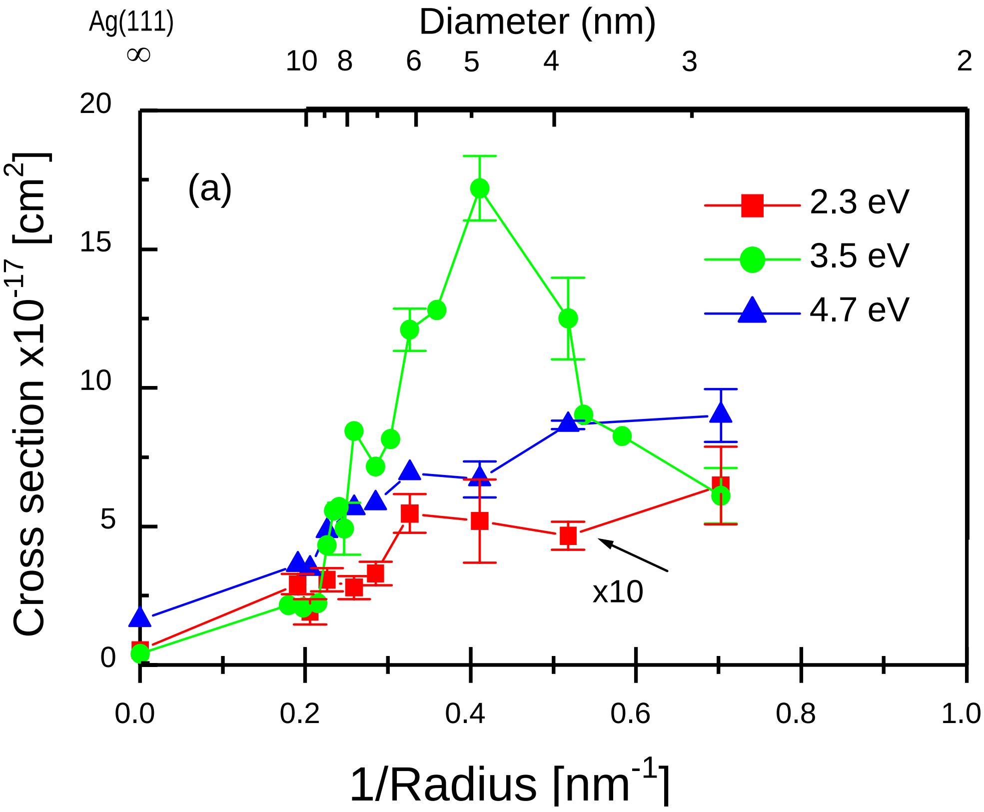

Figure 3.8.: The size dependence of photodepletion cross sections of NO photodesorbed from NO dimers on the Ag NPs. The data are plotted as a function of 1/*R* for excitation energies, *hv* = 2.3 eV (red squares), 3.5 eV (green circles), 4.7 eV (blue triangles). The data at 2.3 eV are multiplied by a factor of ten. The error bars were estimated from the standard deviation of two or more measurements.

As confirmed by post-irradiation-TPD the empty state (LUMO) of NO dimers must be around 2.5 eV above the Fermi level of Ag surfaces. As excitation into the LUMO is even possible at ~2.5 eV, direct excitation of NO dimers is not an important process besides the TNI mechanism. In addition, NO dimers in the gas phase have a continuous absorption band peaked at ~6 eV in the spectral region that leads to photodissociation (4) [Bil72, Mas75, Eas98]. At 5 eV, the photodissociation cross-section of NO dimers in the gas phase was found to be in the range of 1 to 5x10^{-19} cm^2. However, in our system the desorption cross-section at 4.7 eV is ~ 1.6 to 9 x 10^{-17} (depending on the Ag NP size) which is much higher (> 100 times) than the observed gas phase cross-sections.

---

(4) However the photo excitation spectrum of an adsorbed molecule may be modified from that observed in the gas phase due to hybridization of molecular orbitals with those of the substrate, and charge transfer excitation.

Thus, the large enhancement in the desorption cross-section of NO from Ag surfaces, compared to the gas phase cross-section also suggests that the substrate-mediated process plays a dominant role in the photodesorption process of NO from NO dimers adsorbed on Ag surfaces, in the photon energy range used in this study. Hence the contribution of a direct excitation mechanism is negligible even at the highest photon energy used, 4.7 eV, even though it can not be excluded principally. Therefore, the PCS is expected to scale with the yield of hot electrons within Ag NPs that reach the surface and can attach to the NO dimer's empty resonance state (LUMO).

2.3 and 4.7 eV photon energies are far from the Mie plasmon resonance energy of Ag NPs [Nil00]. The observed linear increase of PCS with $1/R$ can be explained by the confinement of the photoexcited electrons by the nanoparticle size and the insulating oxide film underneath. When the dimension of the NPs is smaller than the mean free path of the electrons near the Fermi edge (which is about 44 nm in Ag [Cro62]), hot electrons created within the NPs can scatter several times at the surface of the nanoparticles. Such multiple scattering effects are determined by the Fermi velocity of electrons (v_F) and the radius of the nanoparticles (R) i.e., the number of scattering is proportional to v_F/R. Therefore, the $1/R$ relation simply reflects the ratio of the surface scattering probability, which is proportional to the surface area $4\pi R^2$, and the number of electrons, which is proportional to the volume $(4/3)\pi R^3$ of the NPs of radius $R = D/2$. Therefore, these scattering events that scale linearly with $1/R$, increase the hot electron availability at the surface and correspondingly enhance the photoreaction efficiency of adsorbates on the NP surface. According to the transient negative ion (TNI) mechanism, adsorbed NO dimers are excited by hot electrons photogenerated within the Ag NPs. Therefore, the observed linear increase of PCS at 2.3 and 4.7 eV with $1/R$ can be ascribed to this confinement effect.

At 3.5 eV in *p*-polarization, the (1,0) Mie plasmon of Ag nanoparticles is excited resonantly [Nil00, Eve05]. Therefore, the observed anomalous size dependent behavior of PCS observed at $h\nu = 3.5$ eV in *p*-polarization must be related to the plasmon excitation. Such a collective electron density oscillation is de-excited very rapidly. The plasmon may decay in different ways or channels which depend on the size and shape of the NPs (see figure 3.9). For larger nanoparticles, $D > 20$ nm, plasmons decay mainly into photon emission (*radiation damping* of plasmons), whereas for $D \leq \sim 20$ nm Landau damping of the plasmon that leads to electron-hole pair creation becomes increasingly more effective and saturates at very small sizes, $1 < D < 4$ nm [Mol02]. In the latter case, the hot electrons produced in the plasmon decay can induce photochemistry of adsorbates on the NP surface. Hence, this is the first candidate for the observed rapid enhancement of PCS with reducing the nanoparticle size compared to non-resonant photon energies. On the other hand, when the nanoparticle size becomes smaller, the number of conduction electrons that effectively contribute to the surface plasmon resonance and promote the enhancement of local field is substantially reduced. Such effects were observed in Cu NPs deposited on thin alumina film [Req05]. In Cu NPs/Al_2O_3 films, a strong reduction of the field enhancement of the local field due to the increased fraction of Cu atoms present on the surface with respect to the total amount of atoms (i.e., increasing of the surface to volume ratio) was observed. The observed size dependent cross-section at 3.5 eV in *p*-polarization is therefore the net result of competition between at least the above mentioned two opposing size effects. The rapid increase of PCS down to $D = \sim 5$ nm ($1/R = \sim 0.4$ nm^{-1}) is attributed to the increasing contribution of Landau damping with decreasing *D*. On the other hand, the steep decrease of PCS below ~5 nm can be explained by the latter mechanism i.e., due to the reduced number of conduction electrons participating in the plasmon oscillation.

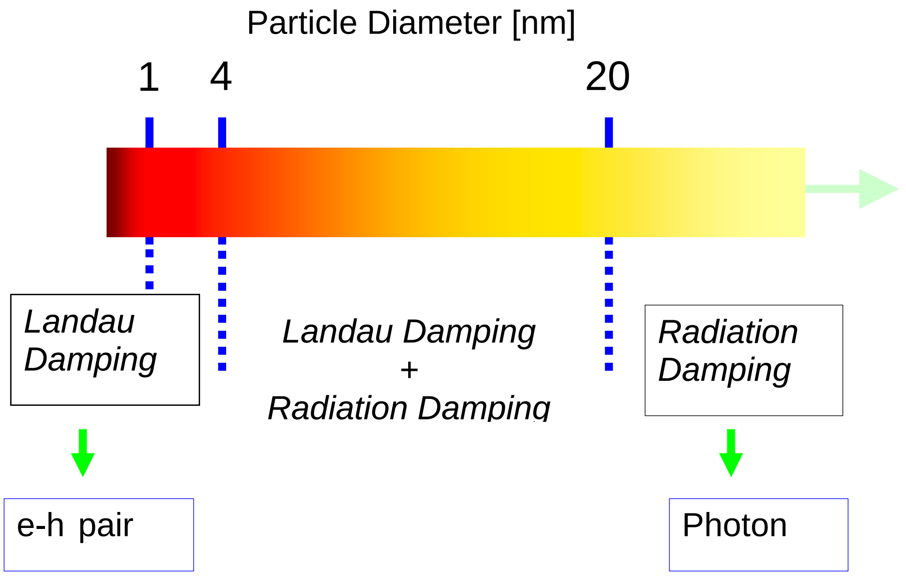

Figure 3.9.: Schematic view of size dependent plasmon decay channels.

As can be seen from the results, at the largest and smallest nanoparticle sizes, the observed enhancements of PCS at 3.5 eV are comparable to the enhancements observed at non-resonant excitations. This suggests that the effect of plasmons on the PCS enhancement is strongly quenched at these sizes. Therefore, at these particle sizes the observed enhancement could arise from the confinement effect similar to the non-resonant excitation energies.

The above interpretations contain only the most important contributions. In fact several other factors can also contribute to the observed size dependent PCS: *First*, the PCS should depend on the frequency of the surface plasmon resonance which is blue shifted with decreasing size. However, since the blue shift of the plasmon frequency is accompanied by broadening of the resonance [Nil00], the slight shift of the peak position with size does not have a significant influence on the excitation strength. *Second*, Landau damping decreases the field enhancement, this can partially compensate the decreased share of electron-hole pair production of plasmon decay with decreasing *D*. *Third*, since NO dimers interact chemically with the surface the electron density in the NPs may be modified, due to static charge transfer between the adsorbate and NPs, and this may result in a shift of the position of the surface plasmon resonance, usually red shift. *Fourth*, the presence of adsorbates can induce a new electronic state at the Ag NP surface, in our case the NO dimer resonance state. Then the oscillating electrons can tunnel into and out of such surface states, which results in the decay of plasmon resonance by the so called *chemical interface damping* (CID) and consequently reduce the field enhancement. But the oscillating electrons can induce photochemistry by exciting the molecule to its TNI state. In addition the spill-out and screening effects at the NP surface are also expected to vary with particle size and may have their own effect on the PCS [Mol02].

The size effects in the desorption cross-section are therefore a complicated function of different parameters. Careful and detailed theoretical analysis would be needed to unravel all the above mentioned contributions. Therefore, our interpretation is based only on the most dominant effects.

3.4. Summary

In summary, the thermal and photochemical properties of NO dimers adsorbed on Ag NPs of varied size on Al_2O_3/NiAl (110) substrates have been investigated. We have found size dependences with simple scaling as well as with peaked behavior or abrupt changes. The adsorption energy and branching ratios of NO and N_2O formed from thermal reactions of NO dimers adsorbed on Ag NPs were found to vary with particle size. The peak temperatures of thermal desorption of NO and N_2O from these layers decreased with decreasing size and show a simple linear scaling with ~1/R. The PCS of NO roughly increases with ~1/R for nonresonant excitation (photon energies 2.3 and 4.7 eV). This is explained by the confinement effect of hot charge carriers which leads to desorption via the transient ion state. However, for excitation in the plasmon resonance (3.5 eV, *p*-polarized) a strong peak at D = ~5 nm is observed which can be considered as the net result of competition between at least two opposing size effects. The rapid increase of PCS down to D = ~5 nm (1/R = ~ 0.4 nm^{-1}) is attributed to the increasing contribution of Landau damping with decreasing D. On the other hand, the steep decrease of PCS below ~5 nm can be explained due to the reduced number of conduction electrons participating in the plasmon oscillation (which scales with total number of atoms). Additional size effects are also likely to be involved.

Chapter 4

Photodesorption dynamics of NO from $(NO)_2$ on Ag NPs - *The effect of particle size*

This chapter will be concerned with the dynamics of nanosecond (ns) laser induced desorption of NO from NO dimers adsorbed on various size Ag NPs. The translational and internal state properties of NO desorbed by 2.3, 3.5, and 4.7 eV have been investigated by using QMS-TOF and (1+1) REMPI techniques to get some detailed insights about the desorption dynamics at various diameters, *D*. After a general introduction about some relevant points which are helpful for general understanding of photochemistry, the results found in this work will be presented and then a brief discussion will follow. Both rotationally and vibrationally hot molecules with a temperature well above the sample temperature are detected at two different velocities, 950 m/s and 1500 m/s. The translational and rotational excitations are positively correlated while the vibrational excitation is decoupled from the other two excitations. The translational and internal energy distributions of photodesorbed NO molecules at $h\nu = 2.3$ and 3.5 eV excitations are almost constant throughout the Ag NPs size which suggests a constant mechanism is operative throughout the size regime. This observation also suggests the photodesorption mechanism of NO is not changed by plasmon excitation at 3.5 eV. At 4.7 eV and smaller particle sizes a new desorption channel which results in energetic desorbates is observed. The possible mechanisms are discussed. The chapter concludes with a summary of the main points.

Keywords: Ag NPs, NO dimers, translational energy, internal energy, desorption dynamics

4.1. Introduction

Initiation and subsequent monitoring of elementary processes on surfaces is a key issue for thermal and photochemistry of molecules on metal surfaces for both fundamental and practical reasons since these processes are strongly related to material fabrication and catalysis. On a metal surface, the excitation and desorption processes involve basic process of excitation and relaxation of substrate electrons and adsorbates, and energy transfer among the various molecular and substrate degrees of freedom. Therefore, to describe the photo induced processes accurately, correct understanding of these fundamental issues is needed.

Photoinduced processes of adsorbates mainly NO and CO, on well defined single crystal surfaces have been extensively studied by various groups and the results have been exhaustively reviewed [Chu83, Zho91, Zim95, Has95]. Most of these results showed that the photodesorption proceeds by a nonthermal mechanism mediated via hot electrons created by photon absorption in the metal substrate. These processes are often described in the Menzel–Gomer–Redhead MGR model and its extensions [Men64, Red64, Ant80, Gad90]. Time- and state-resolved detection of desorbed molecules may provide information about the interaction potential energy surfaces (PES) involved and the dynamics occurring on these PESs. Besides the PESs involved, the lifetime of the excited intermediate state(s) determines the yield and the dynamics of the desorption process. Photodesorption of molecules from metal or semiconductors often lead to velocity distributions that resemble a thermal distribution with a translational temperature much higher than the sample temperature in most photodesorption measurements [Bun88, Bun89, Har95, Hog07]. Furthermore, rotational distributions of desorbates that can be described by Boltzmann distribution are often found [Nat88, Mas91, Mas92, Fuk93[b], Ric92]. Rotational excitation may happen due to the torque produced by the accelerating force on the molecule which is tilted. In addition in many systems a correlation between the rotational and translational excitations are observed [Mul92, Ric92, Fuk93, Bun89, Has90, Per93] which can be explained by the impulsive model proposed by Zimmermann and Ho [Zim95]. For photodesorbed diatomic molecules from metal surfaces, vibrational temperatures ranging from 850 – 1500 K are found [Fuk93[a], Bun89, Per93,]. On semiconductor and oxide surfaces, on the other hand, relatively higher vibrational temperatures in the range 1600 – 2900 K are found [Mul92, Men94, AlS94, Wil99]. The higher degree of vibrational excitation is believed to be due to the longer life time of molecules in the excited state PES. Photodissociation of adsorbed molecules also gives highly vibrationally excited molecules [Has90[a], Jac95, Chu94]. The dynamics of dissociation/desorption mechanism involves a complicated energy transfer between the different vibrational degrees of freedom therefore it can not be explained by a simple model used for intact molecules.

All of the available experimental data mentioned above are from flat surfaces. In metal nanoparticles these processes may be modified. However, despite of its potential importance, detailed experimental studies of photoinduced processes on metal nanoparticles are very rare [AlS06, Wat06]. As briefly introduced in *Chapter 3*, metal nanoparticles can offer many special properties which cannot be found on bulk material. Among others, plasmon excitation and confinement of electron excitation are some of them, and these properties are strongly dependent on the size of the NPs. Surface plasmons were already known to enhance the photoreactivity of adsorbates on roughened Ag surfaces [Kid96, Kid00, Myl95] and NPs [Wet05]. Apart from plasmon excitation, in MNPs confinement of the electrons within the nanometer size can increase the contribution of secondary hot electrons which correspondingly increases the efficiency of photoinduced process [Zhd04]. Furthermore, in small MNPs the lifetime of intermediate states can be dramatically influenced by quantum size effects. If the lifetime is very long, the desorption cross section can be increased since collisions of hot electrons with adsorbates are more frequent, and the molecule can gain more energy. The above mentioned properties are expected also to modify the initial excitation and energy dissipation processes which are important for the photodesorption dynamics of adsorbates on metal nanoparticles. Therefore one should be able to control the photochemistry of adsorbates by tuning the size of the MNPs.

Going beyond the macroscopic properties presented in *Chapter 3*, in this chapter the effect of particle size, plasmon excitation and photon energy on the microscopic processes (desorption dynamics) of NO from $(NO)_2$ dimers adsorbed on Ag NPs deposited on thin Al_2O_3 films on NiAl (110) substrate are presented. The dynamical information of the desorption process are extracted from the measured final state energy distributions of the desorbed NO molecules by using MS TOF and (1+1) REMPI techniques.

4.2. Experimental

The UHV system and the techniques for sample preparation have been discussed in *Chapter 2*. Quadrupole mass-selected time-of-flight (QMS-TOF) and resonance enhanced multiphoton ionization ((1+1)-REMPI) techniques are used to study the dynamics of photodesorbed NO molecules from Ag NPs of various sizes at $h\nu$ = 2.3, 3.5, or 4.7 eV excitation. The former is used to get the translational energy distributions of photodesorbed NO molecules averaged over the internal energy populations, while internal energies, i.e., rotational, vibrational, spin-orbit distributions, and state resolved translational energy distributions of the photodesorbed NO molecules are measured by the latter technique.

In the QMS-TOF measurements, a similar setup and measurement procedures as those used for the PID measurements as presented in *Chapter 3 section 3.2,* are used. State-resolved measurements of NO are performed by a (1+1) REMPI via the $A\ ^2\Sigma\ (v' = 0,1) \leftarrow X\ ^2\Pi\ (v'' = 0,1)$ transitions. Following a nanosecond laser (2.3, 3.5 or 4.7 eV) pulse onto Ag NPs of varied size and Ag (111) surfaces, desorbed NO molecules drift into the probe laser path which is 27 mm away from the sample surface. NO is then ionized in its quantum state by the probe laser and accelerated towards the multichannel plate (MCP) assembly by a repeller plate held at +1 kV. The ions then hit the MCP and are detected as ion current. Figure 4.1 shows a schematic diagram of the ion detection assembly. The probe laser spot size at the ionization region was ~ 2 mm in diameter. The sample temperature was kept at 60 K and the surface coverage was maintained by constantly dosing with a background NO pressure of 5×10^{-9} to 4×10^{-8} mbar (depending on the laser energy, fluence, polarization and PCS of NO) during the course of the measurement to compensate for the loss of adsorbed NO by desorption. The REMPI signal was obtained after subtracting the contribution of the background NO gas of known temperature.

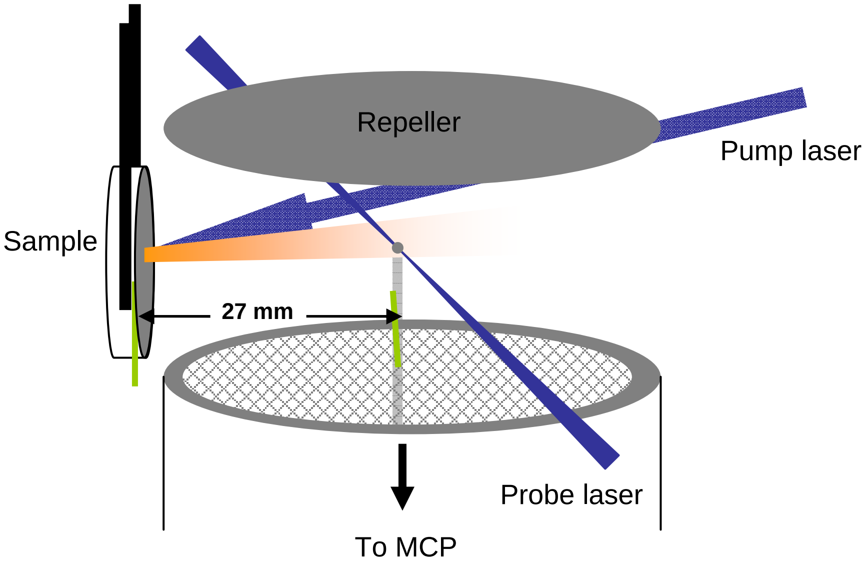

Figure 4.1.: Schematic drawing of the 1+1 REMPI detection system

4.3. Results

The dynamical information about the desorption process can be obtained from the desorbed molecules themselves. Such information can be extracted from the measured final state energy distributions i.e., translational, rotational, vibrational, and spin-orbit energy distributions, of the desorbed molecules. Here, the obtained results on the size dependence of translational and internal energy distributions of the NO molecules desorbed by nanosecond laser pulses, and their correlations are presented. To make clearer the terms *fast* and *slow* components used in this chapter from the similar terms used in *Chapter 3*, some specifications and further expressions are given below. In *Chapter 3*, the *fast* component represented the NO-α species and the *slow* component represented NO-β species and these terms were used to express the efficiency of desorption. In this chapter the same terms are used to express the kinetic energy/velocity of photodesorbed NO-α species. Therefore, in this chapter the *fast* component represents photodesorbed NO-α species that have higher kinetic energy/faster velocity and the *slow* component represents photodesorbed NO-α species with lower kinetic energy. In addition thermal components are also observed which are believed to come from scattered molecules or due to laser heating of the sample surface.

4.3.1. Translational energy distributions

In this section, the translational energy distributions of photodesorbed NO molecules measured by QMS and (1+1) REMPI techniques will be presented. The former technique is insensitive to the internal energy excitations and measures the translational energy of NO averaged over the internal energies, while the latter technique measures the rovibrationally resolved translational energy of desorbed NO molecules.

a) Mass-selected time-of-flight

The size dependence of translational energies of photodesorbed NO molecules were obtained from the measured TOF spectra. The translational temperature of NO-α was calculated by fitting the TOF spectra accumulated from 1 to 100 - 200 laser shots (representative of desorption from NO dimers, see above) to a sum of *shifted* Maxwell-Boltzmann distributions. Depending on the nature of the TOF spectrum, the sum of two or three *shifted* Maxwell Boltzmann functions were used for fitting. The results found at various particle sizes are plotted as a function of the inverse of the particle radius (1/R) including results from Ag (111) at 1/R = 0, for three different excitation photon energies (see in figure 4.1).

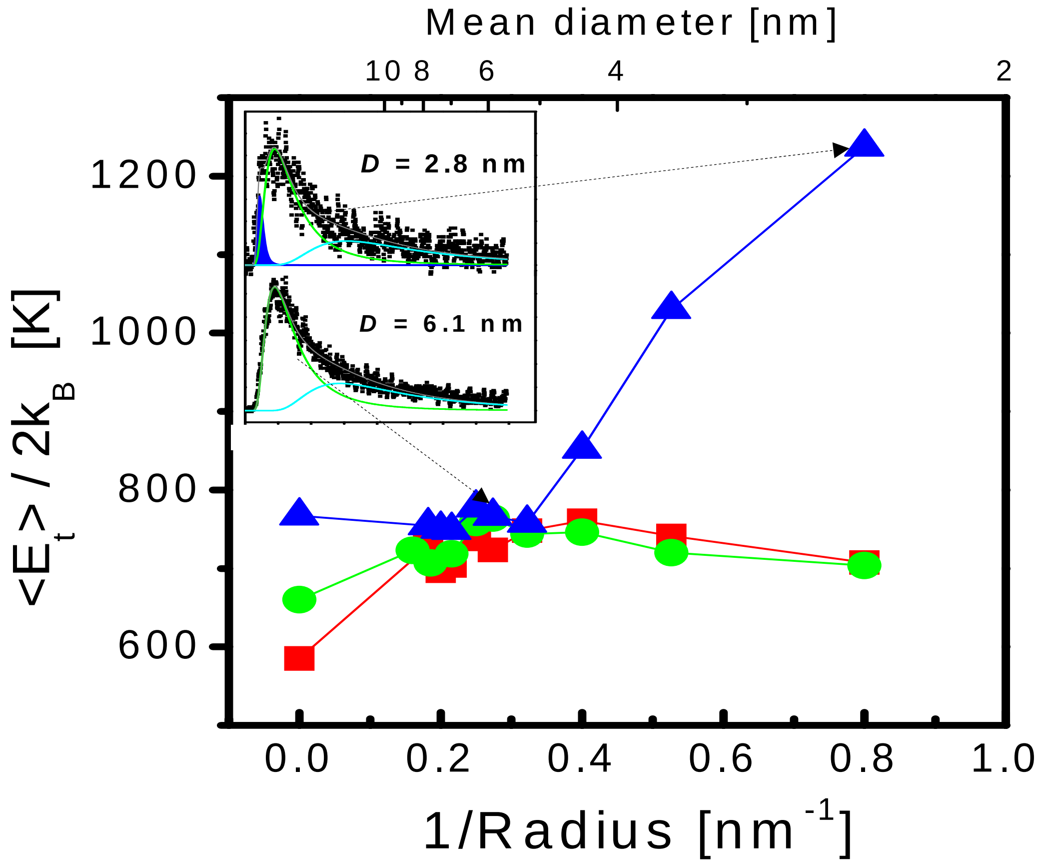

Figure 4.2.: Mean translational energy as a function of 1/R of NO photodesorbed from NO dimers adsorbed on Ag NPs at 2.3 eV (red square), 3.5 eV (green circle), 4.7 eV (blue triangle). The values at 1/R = 0 correspond to data measured on Ag (111). The inset represents the TOF spectra at 2.8 and 6.1 nm particle diameter for 4.7 eV photons fitted with a sum of three (for *D* = 2.8 nm) and two (for *D* = 6.1 nm) SMB distributions.

As can be clearly seen from figure 4.2, the translational temperature of photodesorbed NO at $h\nu = 2.3$ and 3.5 eV (*p*-polarization) is almost constant at 700 -750 K throughout the nanoparticle size and including Ag (111). At 4.7 eV the translational temperature is almost constant at ~750 K down to $D = 6.1$ nm (1/R = 0.3 nm^{-1}). However, it increases almost linearly for $D \leq 6.1$ nm up to the value 1200 K at $D = 2.8$ nm (1/R = 0.7 nm^{-1}). The analysis of the TOF spectra measured for $D = 6.1$ nm shows evidence for a bimodality of the *non-thermal* component (see figure 4.2). The *slow* component still has the same shape as the spectra obtained at 4.7 eV for $D \geq 6.1$ nm while the remaining *fast* component can be fitted by a second *shifted* Maxwell-Boltzmann function.

The relative contribution of the *fast* component with respect to the s*low* component in the TOF spectrum increases with decreasing D below 6.1. The translational temperature of the former increases from ~ 2100 K to ~ 2700 K and the ratio of desorption flux $\mathbf{J}$, $\mathbf{J}_{\text{fast}}/(\mathbf{J}_{\text{slow}} + \mathbf{J}_{\text{fast}})$, increases from ~ 5 % to ~ 12 % with decreasing D from 4.9 nm to 2.8 nm. This anomalous size dependence of translational temperature occurring only at 4.7 eV for small D suggests the emergence of a new photodesorption channel with different dynamics leading to much faster desorbates as will be discussed in detail in *section 4.5*.

b) State-resolved spectra

The translational energy distributions for each internal state (i.e., rotational, vibrational, and spin-orbit states) are obtained by fitting the REMPI-TOF spectra, measured at a known rovibrational and spin-orbit state, with a *shifted* Maxwell-Boltzmann distribution.

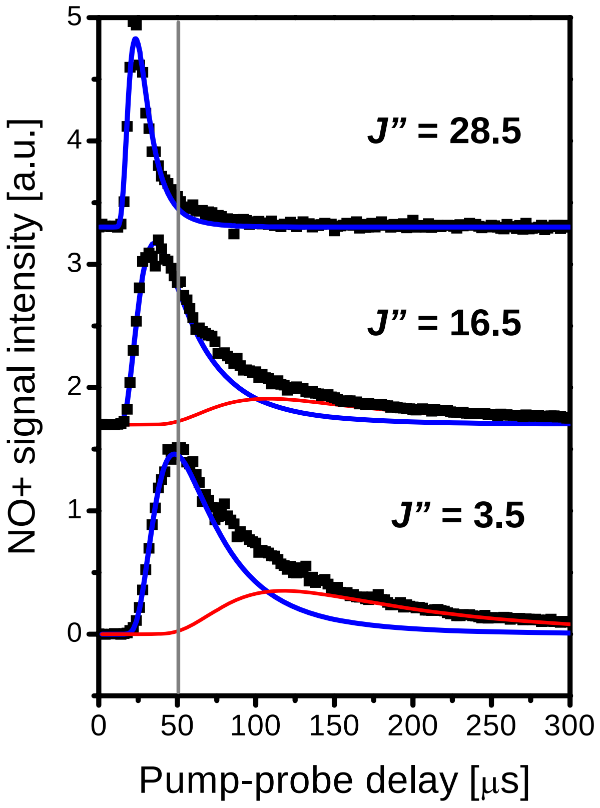

Figure 4.3.: Rotational energy state dependence of TOF spectra for desorbed NO ($v = 0$, $\Omega = 1/2$) from 8-nm Ag NPs at $h\nu = 2.3$ eV. The solid lines are the fit to the *shifted* Maxwellian distribution.

Figure 4.3 shows a series of TOF spectra of photodesorbed NO, in $v = 0$ and $\Omega = 1/2$ and designated *J”* states, measured from 8 nm Ag NPs at $h\nu = 2.3$ eV (*p*-polarized) excitation. The corresponding data were measured also for 3.5 and 4.7 eV excitation energies (not shown) and a similar trend was observed.

The TOF spectra of the desorbed NO molecules show a bimodal distribution at low rotational states. The faster component that has translational temperature well above the sample temperature is ascribed to the photochemical desorption channel. The second component, which has a temperature as low as the sample temperature (60 K), is considered to be due to *thermal* desorption and/or scattered molecules (5). The contribution of the thermal component decreases quickly with increasing rotational energy states, *J”*, and disappears for higher *J”* states. The faster component in the TOF spectra shifts to earlier pump-probe delay with increasing rotational energy states, *J”*. In addition the TOF spectra of the faster component are substantially broader for low *J”* states and become narrower with increasing *J”*.

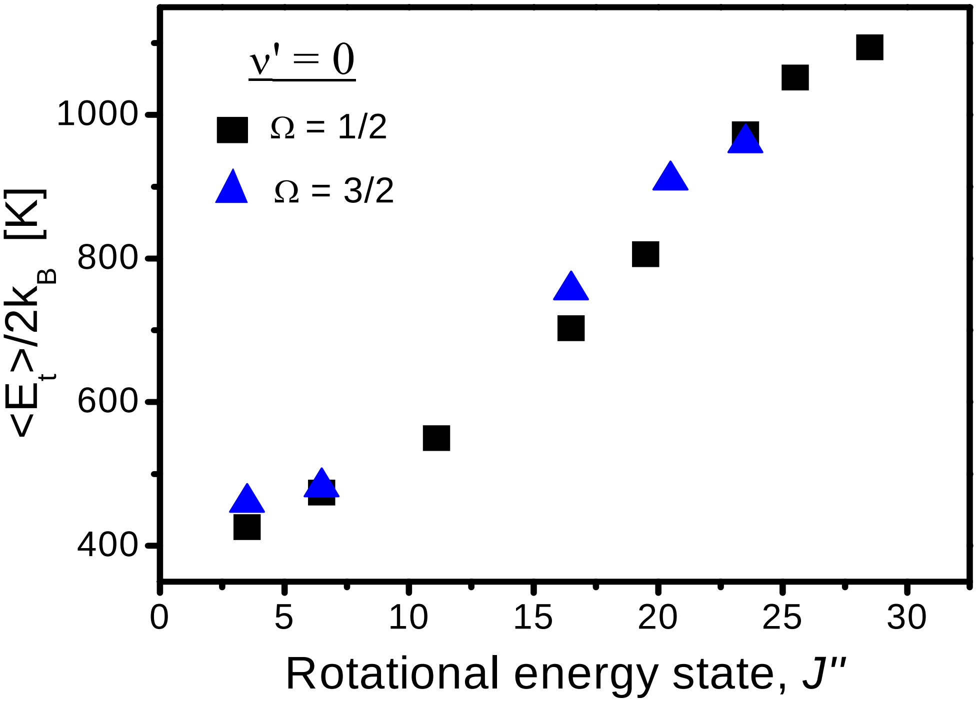

Figure 4.4.: Mean translational temperatures of NO desorbed with 3.5 eV (p-polarized) from Ag (111) surfaces for the two spin-orbit doublets, $\Omega = 1/2$ (black square), $\Omega = 3/2$ (blue triangle) at a given rotational energy state, *J”*.

Unlike to the *J”* dependence of the translational energy, no dependence of translational energy of desorbed NO on vibrational excitation is observed (see section 4.3.4). In addition, similar translational energies of photodesorbed NO (v = 0, *J”* = 3.5 – 28.5) for both spin-orbit states of the NO ($X^2\Pi$) doublet are found (see figure 4.4).

To check the effect of plasmon excitation on the translational energy distribution of the desorbed molecules, we have performed state resolved TOF measurements of photodesorbed NO from Ag NPs at hv = 3.5 eV in *p*- and *s*-polarizations. Table 4.1 shows the translational temperature of photodesorbed NO (v = 0, Ω = 1/2 state and various rotational energy states, *J”*) measured from 5 nm Ag NPs. The results show quite similar values of translational temperature (at a given rovibrational and spin-orbit state) for both polarizations. This result is in agreement with our observation of similar translational temperatures at 3.5 eV (on plasmon resonance) and 2.3 eV (off plasmon resonance) in the QMS-TOF measurements.

Table 4.1: Comparisons between the translational temperature of NO (v = 0, Ω = 1/2) photodesorbed with 3.5 eV in *p*-polarization (on plasmon resonance) and in *s*-polarization (off plasmon resonance) from 5-nm Ag NPs.

	v = 0, Ω = 1/2			
	J” = 3.5	*J”* = 16.5	*J”* = 23.5	*J”* = 28.5
T_t at hv = 3.5 eV, *p*-pol.	304 K	640 K	1111 K	1345 K
T_t at hv = 3.5 eV, *s*-pol.	291 K	577 K	1056 K	1262 K

---

(5) Due to the smaller distance, the contribution of scattered NO will be smaller in REMPI than QMS-TOF, but cannot be excluded even there. On the other hand, the background NO pressure necessary during REMPI measurements to maintain the dimer coverage will lead to scattering in the gas phase (see following section).

4.3.2. Internal state energy distributions

To obtain a better understanding of the underlying mechanism of NO photodesorption we have extended the above translational energy measurements to internal state energy (rotational, vibrational, and spin-orbit energy) distribution measurements.

a) Rotational energy distributions

The rotational energy distributions of photodesorbed NO in the $v = 0$ and $v = 1$ states were obtained from the REMPI spectrum measured by scanning the wavelength of the probe laser through the corresponding rotational band at a fixed pump-probe delay. Figure 4.5 shows a typical REMPI spectrum measured from photodesorbed NO $v = 0$ state at pump-probe delay of 29 µs (corresponding to 950 m/s), from 8 nm Ag NPs with 3.5 eV excitation.

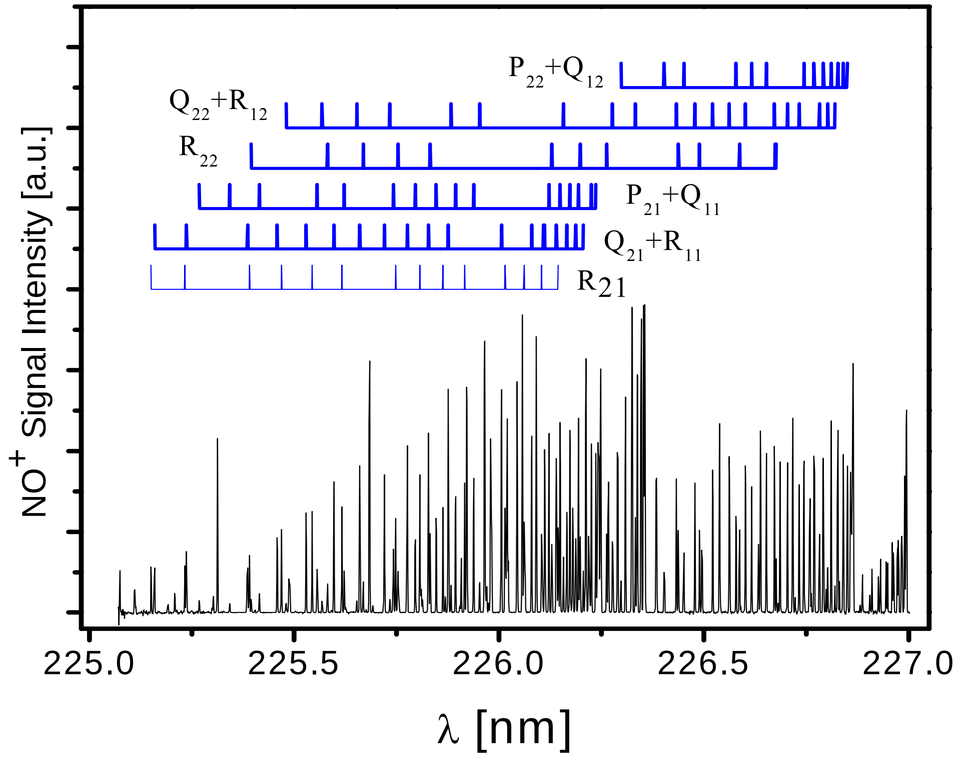

Figure 4.5.: (1+1) REMPI spectrum of NO ($v = 0$, pump-probe delay = 29 µs) desorbed with 3.5 eV in *p*-polarization from 8-nm Ag NPs on Al_2O_3/NiAl (110).

Figure 4.6 shows the Boltzmann plot of photodesorbed NO (v = 0, pump-probe delay = 29 μs corresponding to a velocity of 950 m/s), characterized by a single straight line in the given units (i.e. thermal rotational distribution), and yielding a rotational temperature T_{rot} = 485 ± 50 K. The contributions from the two spin-orbit states ($X^2\Pi_{1/2}$ and $X^2\Pi_{3/2}$), which are energetically separated by about 124 cm^{-1}, fall along the same line in the Boltzmann plots. When the rotational populations in the two spin-orbit states are fitted separately, they gave almost the same rotational temperature, which suggests the spin-orbit excitation is in equilibrium with the rotational excitation. In such cases, the abscissa in the Boltzmann plot can be represented by the sum of the rotational and the spin-orbit energy.

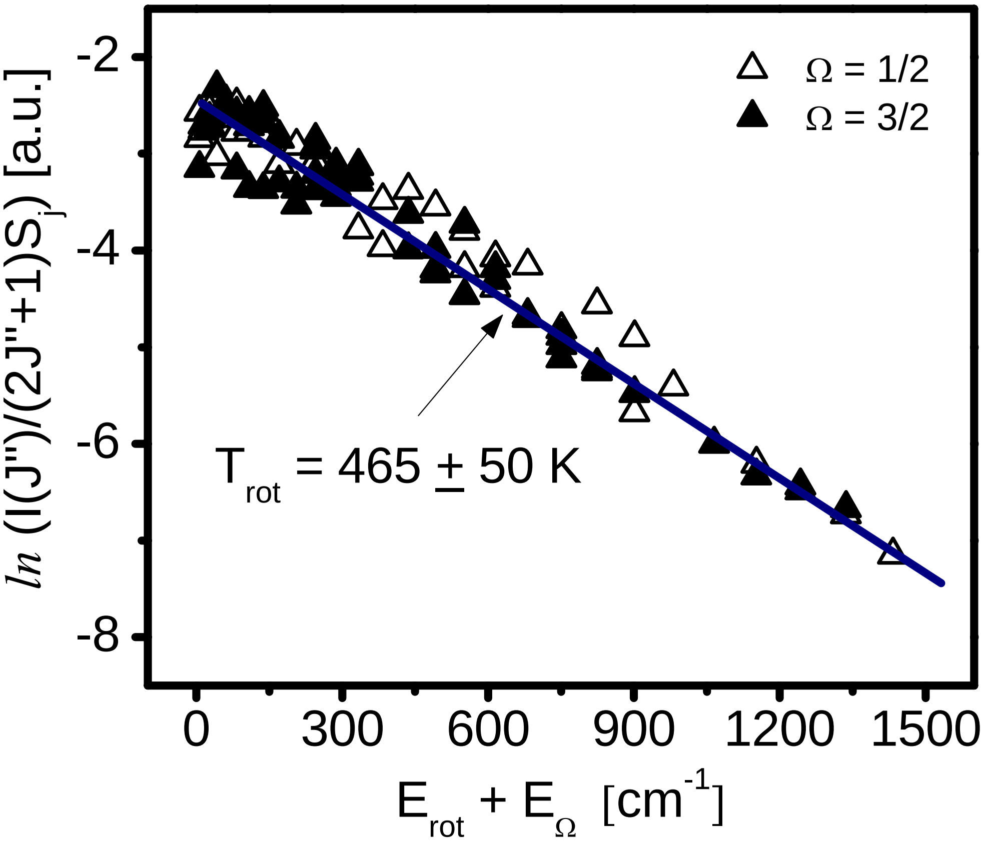

Figure 4.6.: Boltzmann plot of the rotational distribution of NO (v = 0, velocity = 950 m/s) desorbed with 3.5 eV p-polarized photons from 8-nm Ag NPs. Open triangle: Ω = 1/2, filled triangle: Ω = 3/2.

Confirming the results of the above TOF measurements, the delay time-dependent spectra of photodesorbed NO measured from *smaller* Ag NPs at *hv* = 4.7 eV excitation exhibit a faster component compared to results measured for larger particles and lower photon energies. To characterize the internal energy distributions of the *fast* and *slow* components separately, we have performed REMPI measurements at two different pump-probe laser delays which are representative of the two components. Figure 4.7 shows a TOF spectrum of photodesorbed NO (v = 0, J'' = 25.5, Ω = 1/2 state) measured from 4 nm Ag NPs at *hv* = 4.7 eV excitation.

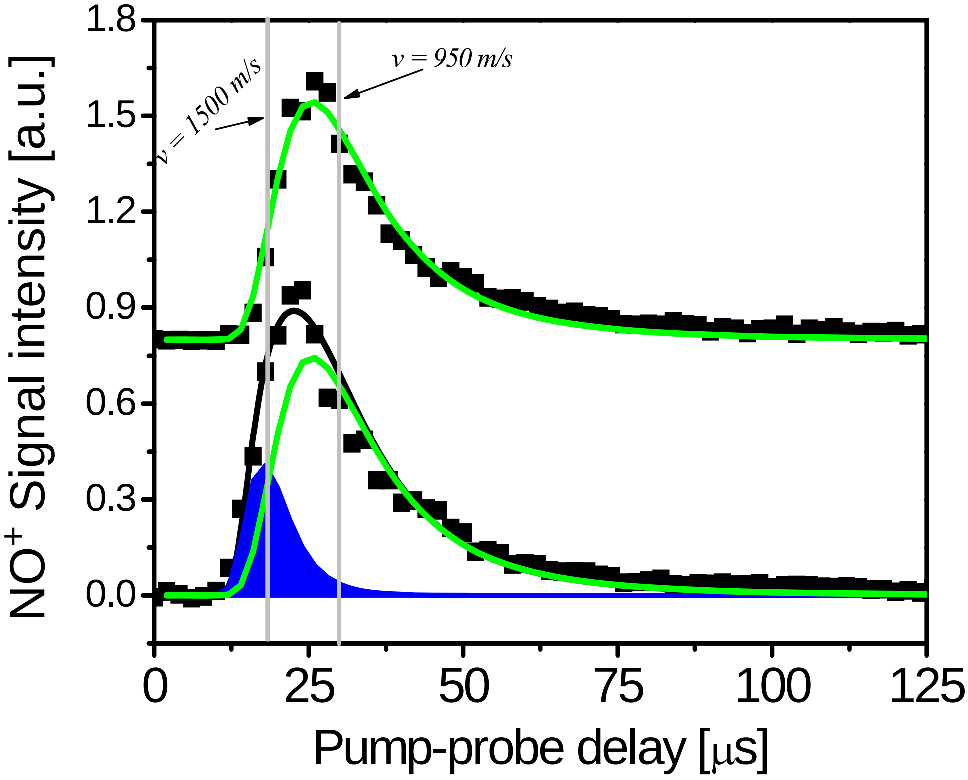

Figure 4.7.: TOF spectra of photodesorbed NO (v = 0, J'' = 25.5, Ω = 1/2 state) measured from 4-nm Ag NPs at *hv* = 4.7 eV excitation. The lower spectrum is fitted with a sum of two *shifted* Maxwell-Boltzmann (SMB) functions, one with a similar shape as the corresponding TOF spectrum measured from 8-nm Ag NPs (upper spectrum), and the remaining fast component is fitted with the second SMB function (blue area). The vertical gray lines on the TOF spectrum show the velocity for which rotational and vibrational distributions were obtained.

The spectrum is fitted with a sum of two *shifted* Maxwell-Boltzmann (SMB) functions, one with a similar shape as the corresponding TOF spectrum measured from 8 nm Ag NPs, and the remaining fast component is fitted with the second SMB function. The vertical gray lines on the TOF spectrum denote a particular velocity for which rotational and vibrational distributions were obtained.

Therefore, the REMPI signal at a pump-probe laser delay of 29 μs (*velocity* = 950 m/s) is dominated by the internal state population distribution of the slow component while the internal state population distribution of the faster component was determined by measuring the REMPI spectrum at a faster pump-probe delay, 19 μs (i.e., molecules which have velocity of ~1500 m/s). At a pump-probe laser delay 19 μs, only molecules photodesorbed from 4 nm Ag NPs at *hv* = 4.7 eV excitation have a sufficient signal-to-noise ratio to derive the rotational temperature.

The rotational temperatures of photodesorbed NO measured at various Ag NP sizes and Ag (111) with *hv* = 2.3, 3.5 and 4.7 eV excitations are shown in Table 4.1. At *hv* = 2.3, 3.5, and 4.7 eV, the rotational temperature of photodesorbed NO (*velocity* = 950 m/s) is almost constant at 450 ± 50 K throughout the nanoparticle size. However, those molecules desorbed with a *velocity* = 1500 m/s from *D* = 4 nm Ag NPs at *hv* = 4.7 eV excitation have a clearly higher rotational temperature, ~620 K. The rotational temperature of photodesorbed NO molecules at *hv* = 3.5 eV (*p*-polarized) is about ~480 K the rotational temperature at the same photon energy but in *s*-polarization is about ~490 K. This again confirms the insignificance of plasmon excitation on the rotational energy distributions of photodesorbed NO.

An average rotational energy of the photodesorbed NO, at a specific vibrational state, can be obtained by calculating a weighted average sum up to a rotational energy level *J"* = 28.5:

$$\left\langle E_{rot}(v)\right\rangle = \frac{1}{N(v)}\sum_{J} N_{rot}(v,J)E_{rot}(v,J), \qquad (4.1)$$

where N_{rot} denotes the population of the rotational level with energy E_{rot}.

Their contribution to the total rotational energy has to be weighted by the respective vibration population for $v = 0$, and $v = 1$ states. The results are summarized in Table 4.3 below. It should be noted that the true rotational energy is expected to be slightly higher, due to populations of rotational states above *J"* = 28.5. Moreover, due to correlations between rotational and translational energies the measured rotational energy at a fixed pump-probe delay may not represent the total average rotational energy of the fast or slow component.

b) Vibrational energy distributions

In order to get the degree of vibrational excitation of the photodesorbed NO, the REMPI spectra are measured by tuning the probe laser over the NO γ-bands at fixed pump-probe laser delays of 29 µs or 19 µs. This yields the vibrational population distribution of the *slow* or the *fast* component, respectively. At the pump-probe laser delay of 19 µs, only molecules photodesorbed at $h\nu$ = 4.7 eV excitation from D = 4 nm Ag NPs have a sufficient signal to calculate the vibrational population.

The vibrational temperatures are determined by comparing the signal intensities in v = 1 and v = 0 states with similar J'', after intensity normalization with Franck-Condon factors and assuming a Boltzmann distribution for the vibrational populations. Here, we assume equal detection efficiencies for v = 0 and v = 1 states and we use Frank-Condon factors of 0.17 and 0.11 for the (0,0) and (1,1) NO γ-band transitions, respectively.

The vibrational temperatures of photodesorbed NO measured at various Ag NPs including results from Ag (111) at $h\nu$ = 2.3, 3.5 and 4.7 eV excitations are shown in Table 4.2. At $h\nu$ = 2.3 and 3.5 eV excitations the vibrational level v = 1 is populated with ~ 2 - 3 % of the photodesorbed molecules, which corresponds to a vibrational temperature of T_{vib} = ~700 - 780 K and does not significantly change with particle size, D. On the other hand, at 4.7 eV the vibrational level v = 1 is populated with ~14 % (T_{vib} = ~1390 K) for the slow (*velocities* 950 m/s) and ~17 % (T_{vib} = ~1550 K) for the fast (*velocity* = 1500 m/s) components of photodesorbed NO. At 3.5 eV *p*-polarized the vibrational level v = 1 is populated with ~1.6 % (T_{vib} = ~660 K) and at the same photon energy but in *s*-polarization the vibrational level v = 1 is populated with ~2 % (T_{vib} = ~710 K). This observation again suggests, plasmon excitation at 3.5 eV in *p*-polarization has no significant influence on the vibrational excitation of the photodesorbed molecules.

The average vibrational energy of photodesorbed NO can be calculated by using the following equation:

$$\langle E_v \rangle = \frac{1}{N} \sum_v N_v(v) E_v(v) , \qquad (4.2)$$

where $E_v(v)$ is the vibrational state energy and $N_v(v)$ is the population of the corresponding vibrational level (v = 0 or v = 1). The average vibrational energies for the fast and slow components are summarized in Table 4.2.

Table 4.2: Summary of the rotational and vibrational temperatures of NO photodesorbed with 2.3, 3.5, and 4.7 eV from Ag surfaces.

hv [eV]	*polarization*	*substrate*	*velocity [m/s]*	T_{rot} *[K]*	T_{vib} *[K]*
2.3	*p*	Ag (111)	950	~425	~780
	p	4 nm Ag NPs	950	~405	~692
	p	8 nm Ag NPs	950	~462	~667
	s	8 nm Ag NPs	950	~460	~670
	p	11 nm Ag NPs	950	~452	~697
3.5	*p*	Ag (111)	950	~438	~797
	p	4 nm Ag NPs	950	~370	~687
	p	8 nm Ag NPs	950	~485	~655
	s	8 nm Ag NPs	950	~490	~700
	p	11 nm Ag NPs	950	~470	~670
4.7	*p*	Ag (111)	950	~432	~788
	p	4 nm Ag NPs	950	~400	~1390
	p	4 nm Ag NPs	1500	~620	~1540
	p	8 nm Ag NPs	950	~440	~686
	p	11 nm Ag NPs	950	~474	~726

c) Spin-orbit energy distributions

The REMPI spectra obtained from a wavelength scan can also probe the populations in the two spin-orbit states of the ground state of NO. In addition, it can also provide the populations in the two lambda doublet states within each spin-orbit state. The former can be determined by comparing the peak heights (after normalizing with the Honl-London factors) for transitions originating from the two spin orbit states, $X^2\Pi_{1/2}$ and $X^2\Pi_{3/2}$ which are separated by 124 cm^{-1}. Here we took the populations of the R_{21} and P_{21}+Q_{11} branches for the spin-orbit $\Pi_{1/2}$ state, and of the P_{12} and Q_{22}+R_{12} branches for the spin-orbit $\Pi_{3/2}$ state. Thus, the relative peak intensities for these transitions can be taken as the relative populations of the two spin-orbit states. Figure 4.8 shows the individual population ratios in the spin-orbit $\Pi_{1/2}$ and $\Pi_{3/2}$ states as a function of *J”* of NO desorbed from 8 nm Ag NPs at *hv* = 3.5 eV excitation. As can be seen from figure 4.8 the two spin-orbit states are equally populated.

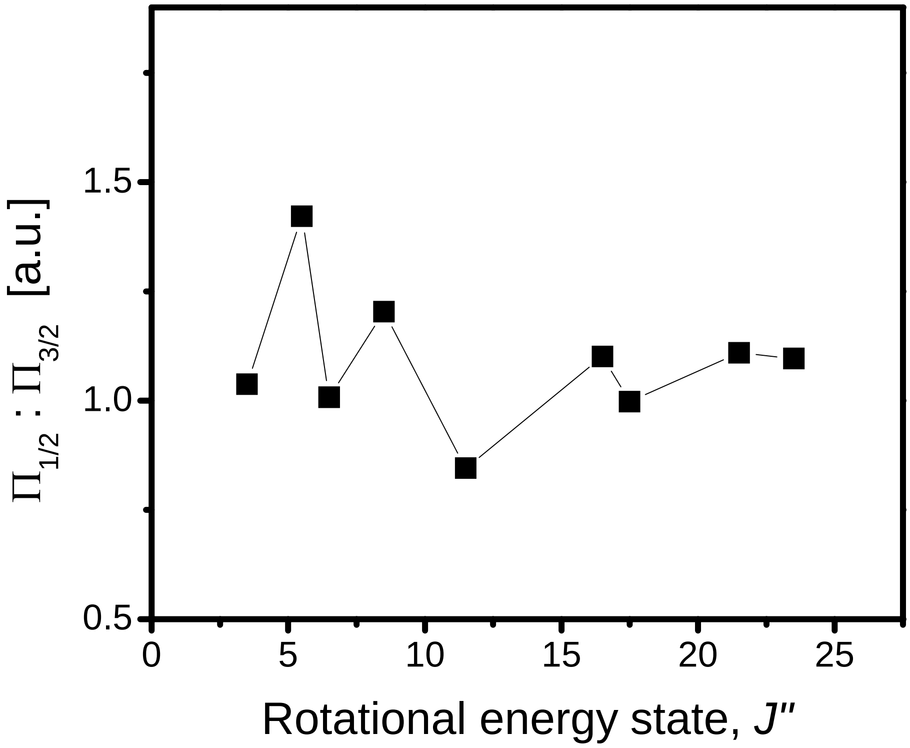

Figure 4.8.: Population ratios in the spin-orbit $\Pi_{1/2}$ and $\Pi_{3/2}$ states of NO desorbed from 8-nm Ag NPs at *hv* = 3.5 eV as a function of *J”*.

4.3.3. Energy partitioning into the different degrees of freedom

The amount of energy partitioned into the different degrees of freedom (DOF) will tell us the fraction of the initial excitation energy that goes to the excitation of translational, rotational, vibrational and electronic degrees of freedom. From the energy provided by the photon, *hv,* a part will be dissipated in dimer dissociation and subsequent breaking of the adsorption bond (E_{ads}). The remainder will be available for excitations of translational and internal DOF of the desorbed NO. From the TPD results presented in *Chapter 3* E_{ads} is very small compared to the excitation photon energies (*hv* = 2.3, 3.5, or 4.7 eV) and can be neglected. Therefore we can consider 2.3, 3.5, and 4.7 eV as the initial available energy for NO dimer excitation.

The total energy in the translational and internal DOF of the desorbed NO molecules are determined from the translational and internal energy distributions presented above (Section 4.3.1 and Section 4.3.2). The average translational energies of photodesorbed NO molecules are obtained from the QMS-TOF measurements. Since these measurements are already averaged over the internal quantum states, no further averaging is necessary. The average rotational and vibrational energies are determined using equations (4.1) and (4.2), respectively. The results found are summarized in Table 4.3 below.

Table 4.3: The translational, vibrational, and rotational energy contents in the photodesorbed NO from slow and fast channels (all values are given in eV).

Species	$\langle E_{tran} \rangle$	$\langle E_{rot} \rangle$	$\langle E_{vib} \rangle$	$\langle E_{tot} \rangle$
Slow @ 2.3 & 3.5 eV	0.125	0.04	0.006	0.17
Slow @ 4.7 eV	0.126	0.039	0.035	0.20
Fast @ 4.7 eV	0.414	0.055	0.042	0.51

Where, $\langle E_{tra} \rangle$, $\langle E_{rot} \rangle$, and $\langle E_{vib} \rangle$ are the average translational, rotational and vibrational energies, respectively.

As can be seen from the above table, a significant part of the released energy is found as translational energy, E_{tra}. The total energy which goes to the different DOF of desorbing NO can then be obtained from the sum of the contributions of all DOF:

$$\langle E_{tot} \rangle = \langle E_{tra} \rangle + \langle E_{rot} \rangle + \langle E_{vib} \rangle + \langle E_{ele} \rangle , \qquad (4.3)$$

where, $<E_{\mathrm{tot}}>$, and $<E_{\mathrm{ele}}>$ are the average total and electronic energies, respectively.

Hence, ~0.17 eV (for the slow component) and 0.51 eV (for the fast component) is released into the desorbing NO molecules which is much smaller than the energy provided by the photon. In metal/adsorbate systems the major fraction of the excitation energy is lost (and transferred to the substrate) due to the short lifetime ($10^{-16} – 10^{-13}$ s) of electronic excitations. This could be due to some part of the excitation energy dissipated into the substrate by the repulsion after neutralization, but mainly by the electron jumping back.

4.3.4. Correlations between the different DOF

So far the results from individual final state energy distributions of the desorbed NO have been presented. However, more information about the dynamics of the desorption process can be obtained from the correlations among the final state energy distributions of the photodesorbed NO molecules.

As shown in section 4.3.1.b, the TOF spectra of photodesorbed NO shifted to the fast pump-probe delay and became narrower with increasing rotational states *J”*. The translational temperature, obtained from fitting of these spectra with SMB functions, therefore increases with increasing rotational excitation, *J”*. Such a positive correlation between the translational and rotational excitations has been observed before from many other systems. It indicates the coupling of the translational and rotational excitation during the desorption process.

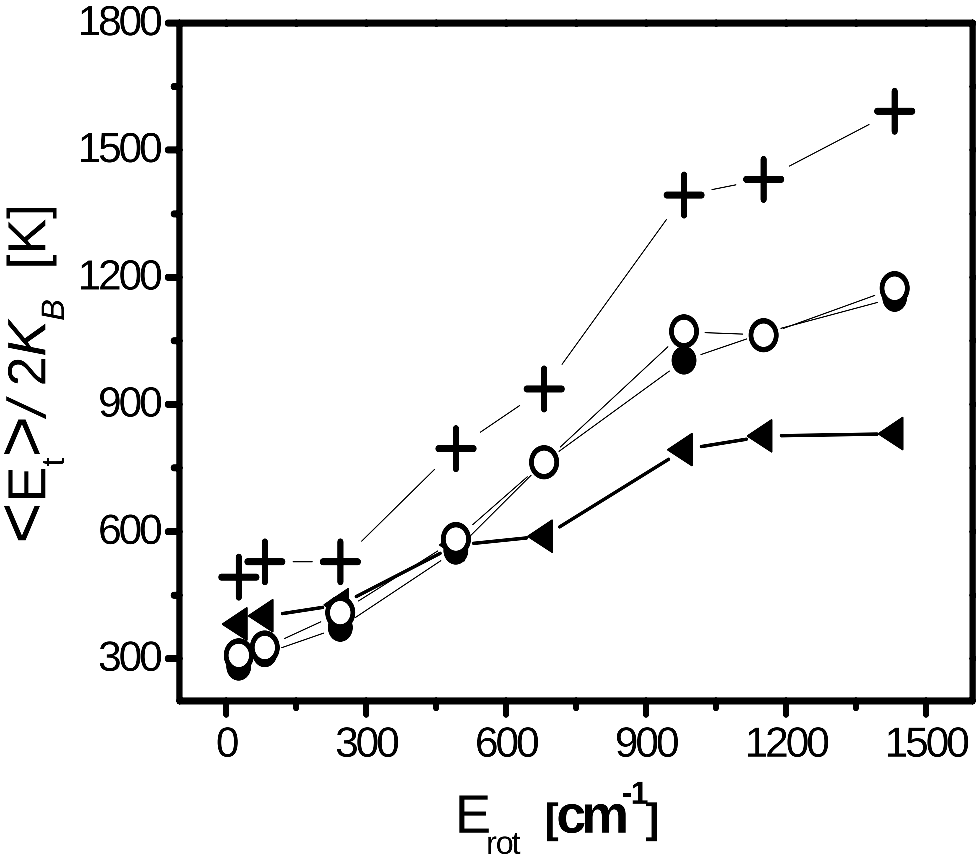

Figure 4.9.: Correlations between mean translational energy, plotted as a function of rotational energy of the particular rotational state of NO $v = 0$, $\Omega = 1/2$, desorbed with 4.7 eV from 4 nm Ag NPs (plus sign), 8-nm Ag NPs (solid circle), 11-nm Ag NPs (open circle), Ag (111) (solid triangle).

Correlations between the translational and rotational temperatures can be used to measure the degree of excitation in the adsorbate-substrate and the degree of tilting of the adsorbate on the surface immediately prior to desorption. To look at the size effects on these correlations we have compared translational-rotational correlations of photodesorbed NO at $h\nu = 4.7$ eV excitation measured from 4, 8, and 10 nm Ag NPs and Ag (111) (see figure 4.9). In all cases a positive correlation between the translational and rotational DOF of the photodesorbed NO is observed. In fact, the correlation is stronger for NO photodesorbed from Ag NPs as compared to that of from Ag (111), and it is strongest for the smallest Ag NPs, $D = 4$ nm.

On the other hand, the translational and rotational energies do not show any significant change between the $v = 0$ and $v = 1$ states. Figure 4.10b shows the TOF spectra, measured from 8-nm Ag NPs at $h\nu = 3.5$ eV (*p*-polarized), for the two vibrational states at $J''=25.5$ and $\Omega = 1/2$ state. From fitting the TOF spectra with SMB functions we deduce a translational temperature of 1028 K and 1058 K for the $v = 0$ and $v = 1$ states, respectively. Thus, the translational temperature of photodesorbed NO in the first vibrational excited state ($v = 1$) is very similar to that found for the ground vibrational state ($v = 0$). Similarly, the rotational distributions of photodesorbed NO are remarkably similar for both vibrational states. Figure 10a shows the Boltzmann plots of photodesorbed NO molecules from 8-nm Ag NPs at $h\nu = 3.5$ eV (*p*-polarization) for the vibrational states $v = 0$ and $v = 1$. The calculated rotational temperatures for $v = 0$, and $v = 1$ states, from the slopes of Boltzmann plots, are 485 and 497 K respectively.

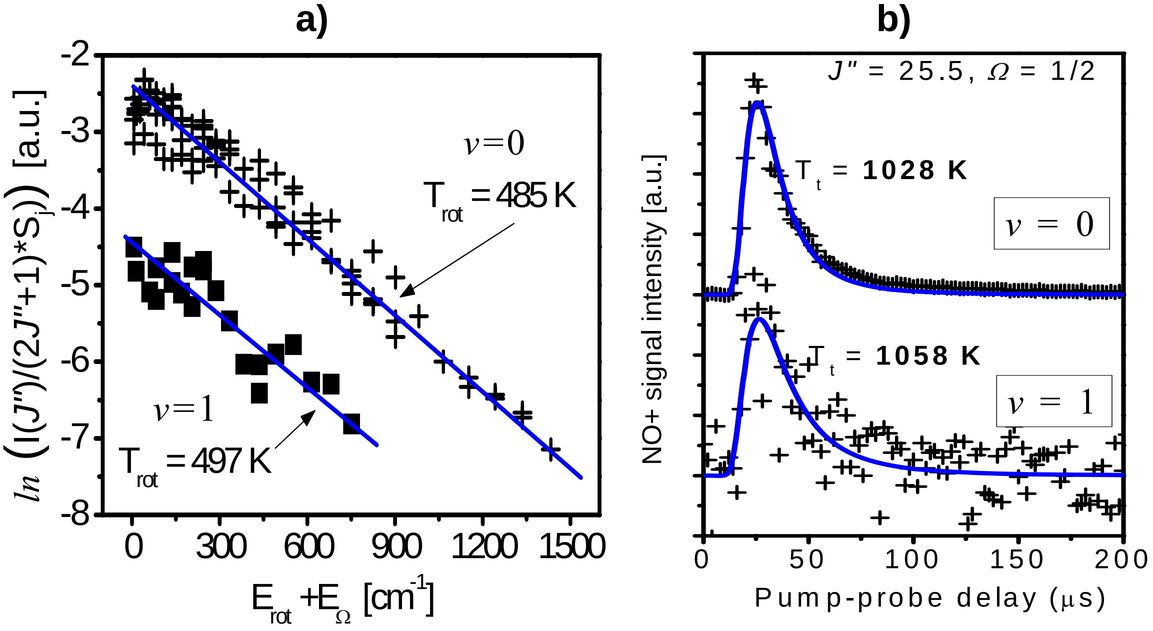

Figure 4.10.: Correlations between a) rotational and vibrational b) translational and vibrational excitations of photodesorbed NO with 3.5 eV in *p*-polarization from 8-nm Ag NPs on Al_2O_3/NiAl (110).

These observations suggest that the vibrational excitation mechanism is strongly decoupled from the rotational and translational degrees of freedom during the desorption process. The above coupling or decoupling behaviors are observed regardless of particle size (including Ag (111)), photon energy, or polarization although their nature or strength may vary as observed in figure 4.9.

4.4. Discussion

4.4.1. Photoexcitation mechanism(s)

Before discussing the photodesorption dynamics, let's recall the photoexcitation mechanism(s) proposed before (in *Chapter 3*). As briefly presented in *Chapter 1*, the photoexcitation of molecules adsorbed on surfaces can be divided into three: i) direct excitation of the adsorbate, ii) indirect excitation of adsorbates i.e., photons absorbed by the substrate create electron-hole pairs that can excite the adsorbate or the adsorbate-substrate complex, and iii) excitation of phonons which leads to laser-induced thermal desorption (LITD). Previous polarization and angle resolved measurements confirmed that the observed photochemistry of NO from NO dimers on the Ag (111) surface is induced by the substrate-mediated hot electron attachment mechanism. Thus it is believed that photodesorption takes place via a transient negative ion (TNI) state produced by photoelectron attachment from the substrate [Yin91, Kid99, Nak06]. For the present system, NO dimers which are weakly chemisorbed on Ag surfaces, the results in *Chapter 3* have provided evidence that the substrate mediated mechanism is the most probable mechanism for initial excitation of NO dimers adsorbed on Ag NPs. Excitation of phonons, which may result in LITD is unlikely for the photon fluence used in this work (< 2 mJ/cm^2/ laser pulse), but can not be excluded for the slow components.

Therefore, the discussions of the photodesorption dynamics of NO from $(NO)_2$ dimers on Ag NPs will be presented based on a substrate mediated process, i.e., photodesorption takes place via transient negative or positive ion (TNI or TPI) states of NO dimers formed by charge carrier attachment from the substrate (here Ag NPs). However, the possibility of a direct excitation channel is also conceivable at $h\nu = 4.7$ eV.

4.4.2. Photodesorption dynamics

The photodesorption dynamics of NO from single crystal metal surfaces has been studied intensively using state resolved detection methods [Ric88, Bun89, Fuk93^b, Mur95], albeit mostly for adsorbed NO monomers. Most of the results from these studies essentially possess many similar features in the final state energy distributions of the desorbing NO molecules. In many cases, the reported rotational distributions resemble Boltzmann (thermal) distributions at temperatures well above the surface temperature. The translational and rotational energies of the desorbing NO molecules show positive correlations. The vibrational excitation is decoupled from other excitations [Bun89]. We have also performed similar measurements on NO dimers adsorbed on single crystal Ag (111) surfaces for comparison. As will be shown below, the results of the present work (on Ag NPs) show many similarities with the NO photodesorption results on single crystal metal surfaces. In our system, the adsorbate is the NO dimer instead of the NO monomer, attachment of substrate hot charge carriers to chemisorbed NO dimers initiates both the photodissociation of NO dimers to monomers and the desorption of monomers. Hence the dynamics of NO desorption from NO dimers adsorbed on Ag surfaces is more complicated due to the parallel breaking of the N – N and NO – surface bonds. For complicated mechanisms of this sort, where little is known about the excited state PES, it is not possible to determine the exact origin of energy dissipation and product state distributions. Therefore we can at present only discuss the qualitative relationships between the observed energy disposal and the proposed mechanisms. Theoretical analysis would be necessary to accomplish more, which is not available at present but will hopefully be stimulated by our detailed results.

In general, photodesorption of adsorbed molecules from metal and semiconductor surfaces is discussed in the MGR model [Men64] and Antoniewicz [Ant80] models, the latter amplified by Ho and Zimmerman [Zim95]. The adsorbed NO dimer molecule is photoexcited from the electronic ground state PES to the excited state PES. The excited ionic or neutral adsorbate accelerates towards or away from the surface depending on whether the excited state is more or less tightly bound than the ground state. During the motion on the excited state potential (at most a few femtosecond for metal substrates [Avo89, Dai95]) the molecule gains kinetic energy, E_K, (due to its acceleration) and changes its position. When the excited undissociated / partially dissociated NO dimer returns back to the neutral state (i.e. to the ground state potential), it will find itself displaced from its equilibrium position and will experience a kick which leads to increased kinetic energy. Finally the molecule will desorb with a kinetic (translational) energy which is the difference between the total energy gained in the excitation/de-excitation process and the remaining potential barrier at the point of relaxation on the ground state PES. The energy gained by the molecule during this excitation/de-excitation sequence strongly depends on the nature of the threedimensional PESs and the lifetime, τ_t, of the molecule in the excited state PES. Therefore any change of the PESs (ground and/or excited state) and/or lifetime of the molecule in the excited state will result in a corresponding change in the final kinetic energy of the photodesorbed molecules. Experimentally, these energies can be determined by measuring the TOF spectra of the desorbing molecules.

In a similar manner, the rovibrational energies of desorbing molecules from metal surfaces are commonly explained in the above mentioned models. Electronic de-excitation of the dimer to increasingly repulsive regions of the ground state PES leads not only to acceleration of the center of mass of the desorbate (excitations of the translational DOF) but also to excitation of rotational DOF of the desorbing NO molecules. On Ag surfaces NO adsorbs as a dimer bonded with the N – N axis in the surface plane and an < NNO bond angle of $\alpha = 120^\circ$ [Bro95]. Therefore, one possible source for rotational excitation in the NO can be the force applied on the dimer after the NO dimer is transferred to the ground PES, giving rise to torque.

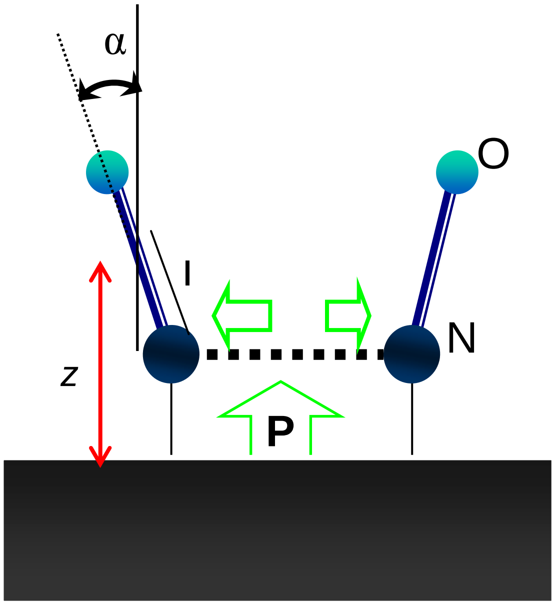

Figure 4.11.: Schematic diagram of impulsive model for NO rotational excitation. Momentum transfer from the substrate and impulsive rupture of N – N bond of the NO dimer can lead rotationally excited NO.

Another possible source of rotational excitation of NO can be the impulsive rupture of the weak N-N bond in a 120° tilted ON – NO configuration of the NO dimer after it is de-excited to the ground state PES (see figure 4.12). However, the latter can happen only if the N – N dissociation force is the dominant force on the ground state PES. But the molecules resulting from the latter mechanism should not be detectable in our experimental setup since the N – N repulsion force should lead to the molecule flying parallel to the surface. But in our measurements we detect molecules which desorb normal to the surface.

As mentioned above the repulsive force applied on the molecule (tilted) excites the molecule's translational and rotational DOF, which leads to the coupling of the two DOF of the desorbed NO molecules. In figure 4.9, evidence was presented illustrating a strong positive correlation between the translation and rotation. The positive correlation can be also explained by a classical theoretical model, called impulsive model, proposed by Zimmermann and Ho. It predicts a positive correlation between the mean translational energy and rotational energy and a narrowing of the Maxwell Boltzmann distribution as the rotational energy is increased [Zim95]. A positive correlation between translational and rotational DOF has been also observed previously for photodesorbing NO molecules from various surfaces.

Vibrational excitation of the desorbed NO molecules can be understood by assuming the NO dimer is excited into a state that is characterized by a different N – O bond length than its equilibrium bond length. The TNI desorption mechanism usually leads to highly vibrationally excited molecules, because the intramolecular equilibrium distances of the negative ion (here $(NO)_2^-$) are expected to be very different from those of the neutral. The excitation of the vibrational DOF is found strongly decoupled from the translation and rotation DOF, which suggests the motion of the molecules in the vibrational coordinate does not affect excitations of other DOF or vise versa. The decoupling also suggests a very different mechanism, as compared to the mechanism of translational and rotational excitations, is responsible for vibrational excitations.

The above mentioned models assume the distributions of the translational and rotational energies are due to the distribution of TNI lifetime. However, that may not be so. Rather, the distributions may mainly come from the range of distances on the ground state curve which comes from the fact that the Franck-Condon range of the initial molecule is first projected onto the TNI curve, which upon deexcitation is further projected onto the repulsive part of the ground state curve. There is no difference of these for different vibrational states, which are due to the stretching of all bonds in the TNI. Therefore, the vibration is non-correlated. The fact that such decoupling has also been found for NO monomer adsorbates with very different bond eliminates the need to ascribe it to the complications arising from the dimer-monomer transition. On the other hand the dimer – monomer transition will be important in the dynamics. Since the excitation start with a ground state dimer and end with a monomer desorption. At some point the excited dimer has to cross over onto the monomer PES.

As can be seen in Table 4.3, the energy available is not equally partitioned into the different DOF. For example, the majority of the availably energy goes to the translational excitation. The distribution of the available energy over the various DOF of the NO molecules is dictated by the detailed dynamics and better understanding needs theoretical calculations. But the extensive data presented here are a good basis for such calculations.

An unequal distribution of the final state DOF with a predominance of the translational energy was also observed from fs laser induced associative desorption of H from Ru (001) [Lun06]. And the authors concluded that the unequal partitioning in the product is due to a translational barrier on the ground state PES.

Since the size dependence of photodesorption dynamics is the central importance of this study, the next section will focus on the main mechanisms that may lead to the observed size dependent changes of NO desorption at three different excitation energies.

Effects of size and photon energy

The constancy of translational and internal energies of photodesorbed NO at 2.3 and 3.5 eV for all sizes suggests that essentially the same mechanism is operative throughout the size regime used in this study. Two points are noteworthy in connection with the constant final energy distributions at 2.3 and 3.5 eV. First, the TPD results in *Chapter 3* have shown a gradual change of the NO dimers' adsorption energy (decrease with decreasing *D*). The observed slight shift of adsorption energy, which suggests also a slight modification of the ground state PES, however, should not have any significant influence on the final state energy distributions of the photodesorbed NO molecules from Ag NPs.

The second point is that, at 3.5 eV in *p*-polarization, the Mie plasmon of the Ag NPs is excited. We have seen in *Chapter 3* that at this photon energy the photodesorption cross-section is enhanced up to 43 times, at *D* = ~5 nm, compared to the Ag (111) surface. Moreover, the nature of the size dependent change of the PCS is significantly different from the one found at 2.3 eV excitation (moderate enhancement, ~11 times compared to Ag (111), and highest at the smallest Ag NP size i.e., at *D* = 2.8 nm). However, the final energy distributions at these two photon energies (2.3 eV which is *off-plasmon resonance* and 3.5 eV which is *on-plasmon resonance*) are equal and show quite similar size dependence, i.e. essentially independence. We have done also similar measurements at equal photon energy, 3.5 eV but at different polarizations i.e., in *p*-polarization (*on plasmon resonance*) and *s*-polarization (*off-plasmon resonance*). The results show no difference in the final state energy distributions of the desorbed molecules. This observation suggests that the Mie plasmon excitation at 3.5 eV does not alter the photodesorption dynamics of NO throughout the Ag NP size. Therefore the effect of the plasmon is only an enhancement of the number of hot electrons participating in the desorption process which increases the desorption probability without changing the desorption mechanism. Apart from the plasmon excitation, one further conclusion that can be drawn from the observed similar final state energy distributions at two different photon energies is that the same energetically low lying transient negative ion state (NO dimer LUMO) is populated (or excitation occurs to a similar PES) regardless of the exciting photon energy. It seems reasonable, based on the above observations, to assume that the PESs and the life time, τ_r, of NO dimers are likely independent of D.

On the other hand, at 4.7 eV anomalous size dependent changes of translational and internal energies of the desorbed NO molecules are observed for small particles. Detailed analysis of these results showed the emergence of a new desorption channel with different dynamics that results in more energetic desorbates than the normal hot electron attachment TNI mechanism. In the following we focus on the dynamics of the photodesorption process giving rise to the fast channel. The origin of this new channel emerging at $h\nu$ = 4.7 eV should be connected with the higher excitation energy rather than a change or modification of PESs with particle size. We speculate about two mechanisms: the first likely mechanism is that this process is triggered by hot holes rather that hot electrons; and the second possible mechanism is a direct excitation of NO dimers, as will be briefly discussed in the following.

1. *d*-band hot hole mechanism (TPI mechanism):

If the incident photon energy is sufficient enough to excite electrons from the *d*-level to above the Fermi level of the substrate, hot holes can be created in the *d*-band of the substrate (see figure 4.12.**B** green upward arrows). If the adsorbate orbital has some hybridization with the *d*-electrons, production of holes in the *d*-state at the surface could lead to a transient positive ion (TPI) which can lead to desorption or reaction.

Why at 4.7 eV? At 4.7 eV photons it is possible to excite electrons i) from the Ag *s*-*p* state to above the vacuum level (see figure 4.12 **A**) or ii) from the Ag *d*-state to above the Fermi level (figure 4.12 **B**). In the following the significance of these two processes on the photochemistry of NO dimers adsorbed on Ag surfaces will be discussed.

On silver surfaces, the excitation of Ag *d*-electrons to above E_F occurs from around 3.9 eV on. Since the adsorption bond of NO dimers on Ag most likely involves some hybridization of Ag *d*-electrons with dimer $^1A_1$-states [Jig99], production of holes in the *d*-state at the surface could lead to a transient positive ion (TPI). It is more likely, therefore that the new excitation accessible at 4.7 eV is that from the Ag *d*-band to empty *sp*-states as schematically shown with a green vertical arrow in figure 4.12 **B**.

On the other hand excitation of the Ag NP surface with $h\nu$ = 4.7 eV which is well above the work function of Ag NPs, will also create photoholes that are localized around the Fermi level (see figure 4.12 **A**, green vertical arrow). However, the possibility of these hot holes to induce desorption is unlikely as they are energetically lower (localized around the Fermi level) than the LUMO level of NO dimers. Also, similar holes will be produced by hot electron scattering during the cooling of the hot electrons produced by 2.3 or 3.5 eV light. Only the hot electron distributions between the vacuum and Fermi level can induce desorption, in a similar way as at the lower photon energies, through the hot electron attachment TNI mechanism.

Hence, at 4.7 eV both electron and hole attachment to an adsorbate will happen which results in formation of TNI and TPI (transient positive ion) states, respectively. In both cases the adsorbate would be likely attracted to the surface by the image charge formed on the substrate Ag NPs [Ant80].

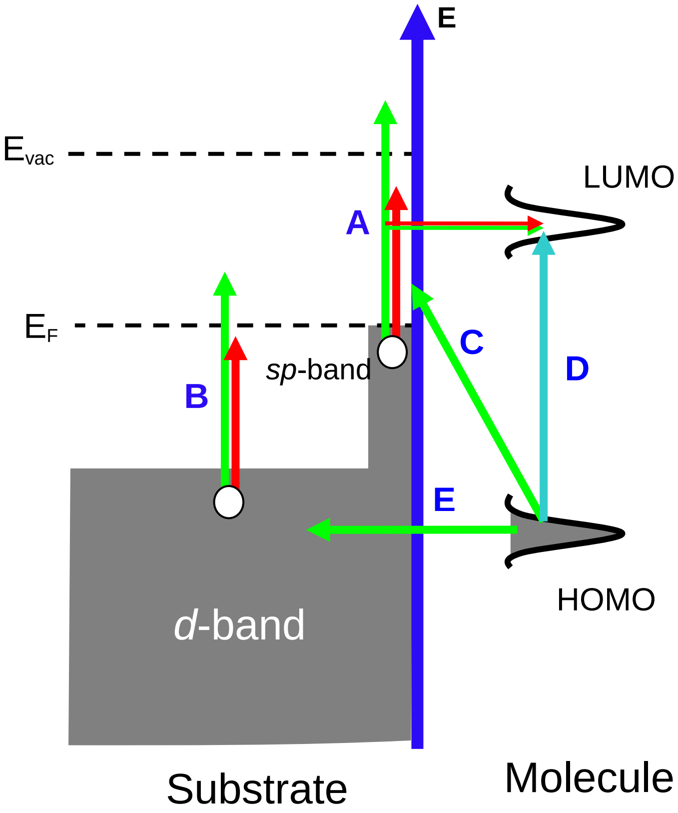

Figure 4.12.: Schematic view of the various photoexcitation mechanisms: **A**. excitations to the TNI state (electron transfer from *s-p* band of substrate to the LUMO of the adsorbate), in addition the excitation shown by a green vertical arrow can create a hole in the *s-p* band (see text). **B**. excitation of *d*-band electrons to below E_F (red) and to the empty *s-p* states above E_F (green). **C**. direct excitation from occupied adsorbate orbital to the empty *s-p* band of the substrate. **D.** direct excitation from HOMO to LUMO of the adsorbate. **E.** electron transfer from occupied adsorbate state to the *d*-hole created in the excitation mechanism **B** (green).

Why is the TPI mechanism dominant at smaller nanoparticle size? For $D \geq 6$ nm the translational and internal energies does not change with size, suggests that photodesorption of NO via the TPI is negligible for larger *D,* i.e. the TNI mechanism is normally dominant. However, for very small Ag NPs ($D < 6$ nm), the TPI mechanism may become more efficient due to the increasing probability of *d*-band holes to localize at the surface that increases with increasing surface to volume ratio (~1/R) of the Ag NPs.

How does the TPI mechanism lead to more energetic desorbates? We suggest the following qualitative argument as a plausible explanation for the new mechanism (TPI mechanism). The adsorbed NO dimer is excited by a charge transfer from the substrate to the transient ion state. The adsorbate transient ion state has a short life time of some 10^{-15} s or less, during which time it is either quenched to the neutral or dissociates to monomers on the excited potential energy surface. Once the ion (TNI or TPI) state is formed, it is attracted to its image charge, moves closer toward the surface, and thus has a surface-to-adsorbate distance that is shorter than that of the neutral. After back-transfer of the negative or positive charge of the NO dimer to the substrate Ag NPs, the neutral NO dimer (or the resulting monomers) which are displaced from their equilibrium position become accelerated and desorb with large kinetic energy. Cations are likely smaller species, so they are further accelerated and approach to the surface closer than the anions. As a result cationic molecules are further displaced from the ground state equilibrium position than the anions. Since the mass of cations and anions are not significantly different, and assuming the excited state PESs for TNI and TPI are dominated by the image attraction and therefore are roughly the same, then one can assume the cation approaches the surface closer, i.e., travels a longer distance in the excited state PES, up to the point of neutralization, where the molecule will fall onto the ground state potential at a closer and therefore energetically higher (and steeper) location. Therefore, this argument can explain the observed higher translational temperature of NO photodesorbed at $h\nu = 4.7$ eV.

However the above assumption of similar excited PES for both TNI and TPI states is probably a gross simplification. The TNI resonance is attributed to population of the π^* molecular orbital of the NO dimer which is involved in the adsorption bond formation in antibonding function. On the other hand, in the TPI mechanism, the Ag *d*-band electrons which are hybridized with the NO dimer's A_1 state are excited above E_F. Since *d*-band electrons are involved in the bonding with NO dimers, excitation of an electron from this band to the *s-p* band may lead to a weakening of the NO dimer adsorption bond and the excited state PES for the TPI and TNI may be quite different. On the other hand, the NO dimer A_1 state is also hybridized with the Ag *s-p* states. Therefore populating Ag *s-p* states is also expected to strengthen the NO dimer – Ag bond. For complicated systems of this sort more theoretical calculations are needed to unravel the consequences and implications of these ionic resonant states of NO dimers on the nature of the excited PES. Therefore, in our interpretation we use the lowest approximation, with the excited PES assumed similar for both ionic states and the major force governing the nuclear motion on these surfaces is the image charge formed on the metal substrate [Ant80].

Assuming the above suggested electron and hole transfer mechanisms to hold, the longer lifetime of the excited NO dimer may result in a highly rotationally excited molecules since the excitation of the rotational DOF is positively correlated to the excitation of translational DOF. As discussed above since the TPI mechanism leads to highly translationally excited NO molecules, the corresponding high rotational excitations are expected (impulsive model). Furthermore, $(NO)_2^+$ may have a different geometry as compared to the neutral NO dimer. In gas phase $(NO)_2^+$ favors a planar *trans*-C_{2h} geometry while the neutral NO dimers has *cis*-C_{2v} geometry [Str96]. Therefore, the high rotational temperature observed in the TPI mechanism could also be due to the very different adsorbate geometry in the TPI state compared to the ground state equilibrium geometry. The strong rotational–translational coupling observed also at 4.7 eV suggests that the electronically excited dimer state is in a different equilibrium configuration than the ground state. In the TPI mechanism, besides higher translational and rotational excitations a significantly higher vibrational excitation is also observed which suggests that in the excited state the N – O bond is considerably stretched or compressed compared to its ground state equilibrium length.

2. Direct excitation of NO dimer as a possible mechanism:

Another alternative mechanism which should be considered for the new channel at 4.7 eV is the direct excitation of NO dimer states to the empty *s*-*p* band, necessitating no *d*-hole transfer (see figure 4.12. **C**). Since the origin of the initial excitation of such a charge transfer (CT) process is an adsorbate valence orbital, the excitation may be localized to the adsorbate. Therefore, such a CT excitation can be considered as a direct or adsorbate localized excitation.

If we compared the “direct” CT with the TPI mechanisms presented above, there is no real difference between the two. In the former, an electron from the adsorbate orbital localized mainly on the dimer is excited into the *s*-*p* band of the NP (figure 4.12 **C**), and in the latter case the same NO dimer orbital is ionized by transferring an electron into the *d*-band hole which is created by exciting a *d*-electron into the *s*-*p* band (see figure 4.12 **E**). In both cases we create a hole in the adsorbate orbital and an electron localized in the *s*-*p* band; only the sequence is different. Hence a “direct” CT mechanism can also lead to a more energetic desorbates as the TPI mechanism.

The next question is, why would this “direct” excitation be strong for small particles? Relatively speaking the number of hot electrons, which are responsible for the TNI mechanism, decreases with the volume of the Ag NPs ($\sim 1/R^3$) while the number of adsorbed dimer molecules is proportional to the surface area ($\sim 1/R^2$) hence the relative strength of the direct excitation mechanism will increase with 1/R as for the TPI mechanism.

Another possible excitation mechanism is the fully localized direct excitation of electrons from the HOMO to LUMO orbitals of the NO dimer, similar to the gas phase excitation. Such direct excitation mechanism was suggested for NO desorption from multilayer NO dimer films on Ag (111) surface [Nat88], and monolayer NO dimers adsorbed on LiF (001) surfaces [Jac95]. However, as mentioned in *Chapter 3*, the cross sections of this direct HOMO-LUMO excitation is extremely low. Furthermore, 4.7 eV are most probably not enough for this excitation (in the isolated dimer it requires > 5 eV). However the photo excitation spectrum of an adsorbed molecule may be modified from that observed in the gas phase due to hybridization of molecular orbitals with those of the substrate. Even in physisorbed molecules, where such hybridization is negligible, screening at the surface could lead to a decrease of the HOMO-LUMO gap [Wat96]. Therefore, this mechanism is less probable, but we can not exclude it in principle.

All the above discussions are based on a generalized, qualitative picture without quantitative knowledge about the nature of the ground and excited state PES or the nature of quenching processes and lifetimes in the excited transient ion states. Therefore, theoretical calculations are needed to get detailed information on these points.

4.5. Summary

In summary, we have investigated the effect of particle size and photon energy, including at plasmon excitation, on the photodesorption dynamics of NO from NO dimers adsorbed on Ag NPs on alumina films on NiAl (110) substrates. Both rotationally and vibrationally hot molecules with temperatures high above the sample temperature are found for NO molecules photodesorbed at two different velocities, 950 m/s and 1500 m/s. The excitation mechanisms for translational and rotational DOF are coupled in the desorption process while the vibrational excitation is decoupled from the other excitations. Constant translational and internal energy distributions of photodesorbed NO molecules at $h\nu = 2.3$ and 3.5 eV excitations are observed throughout the Ag NP size. Furthermore the observed results are quite similar to those found for NO dimers on Ag (111) surfaces. This observation suggests that the accepted mechanism, TNI formation by hot electron attachment, persists throughout the NP size range for 2.3 and 3.5 eV. In addition, the plasmon excitation at 3.5 eV does not change the final state energy distributions of the desorbing NO molecules. Hence, plasmon excitation can increase the cross section via field enhancement but does not change the desorption dynamics. At 4.7 eV and smaller *D*, however, abnormally highly excited desorbates are observed which indicates contributions of a new mechanism. We argue that this consists in formation of hot holes in the adsorbate, either by excitation of *d*-band holes at the Ag NP surface and transfer into an adsorbate orbital, or by direct charge transfer excitation from the latter into the Ag NPs *s-p* band above E_F. This can lead to desorption via transient positive adsorbate ions. Another possible mechanism, direct NO dimer HOMO-LUMO excitation, is unlikely because 4.7 eV are probably not sufficient, and the expected cross sections are very small. The increasing contribution of these mechanisms with decreasing size can be explained by the relative increase of surface atoms (that increases localized *d*-holes at the surface) or the increasing number of NO dimers, in proportion to the surface area compared to the volume of the NPs. However, due to lack of information on the excited PES it is difficult to give a definite and quantitative interpretation of the observed mechanisms. We hope that this work will act as a good motivation for theoreticians.

Chapter 5

State-resolved-measurements of photodesorbed NO from Ag surfaces by femtosecond laser pulses

This chapter provides results concerning translational and internal energy distributions of NO molecules as they are desorbed from 8 nm Ag NPs or an Ag (111) surface by femtosecond (fs) laser pulses at *hν* = 3.1 eV (*p*-polarized) at fluences 0.08 and 0.72 mJ/cm^2. After reviewing the previous results found from the same system used here, the new results will be presented and discussed. The TOF distributions of the desorbed NO molecules are bimodal at lower *J”*, and for the fast component a strong coupling between translation and rotation is observed except for NO molecules desorbed from Ag NPs at fluence, ***F*** = 0.72 mJ/cm^2. Rotationally hot molecules are detected for molecules desorbed with a velocity of 950 m/s, which is a representative of the fast component. On the Ag (111) surface the results are independent of fluence and about equal to those found for nanosecond (ns) pulses. On the other hand on Ag NPs a slight decrease of T_t and T_{rot} are observed with increasing fluence. These results are compared with those obtained for the same system with ns laser pulses at *hν* = 3.5 eV and the possible desorption mechanisms are discussed.

Keywords: DIET, DIMET, friction model, Ag NPs, Ag (111), desorption dynamics

5.1. Introduction

Desorption of molecules on metal surfaces induced by ultrafast laser pulses has attracted much attention. Experimental studies of NO desorption from several metal surfaces have been reported using ultrashort laser pulses [Pry90, Bud93, Mis95, Bud88, Bud91]. Compared with the corresponding DIET process, the desorption process induced by short laser pulses was found to have a higher yield, `hotter' internal-state and translational energy distributions, and the yield scales as a power of the laser fluence, ***F***.

Two basic models have been applied to account for the phenomenon of femtosecond laser induced desorption, usually in higher ***F*** regions: DIMET i.e., adsorbate multiple excitation-deexcitation processes [Mis92, Gao95, Her98] and a frictional coupling scheme in which electrons flow back and forth between the metal substrate and a low lying adsorbate state with a single potential energy surface, PES [New91, Spr96]. These models assume that desorption is mediated by laser excited substrate electrons that are characterized by an electronic temperature $T_{el}(t)$ which could not be explained by a conventional thermal or photochemical desorption mechanism. Usually the lattice temperature rise is not sufficient to explain desorption, so that an electronic mechanism must be responsible. Then the coupling between the adsorbate degrees of freedom and the elevated substrate electron temperature before the latter equilibrates with the substrate phonons explains various experimental findings. There are also approaches that assume thermal desorption induced by high intensity fs laser pulses [Kwi05]. The DIMET/frictional heating process is observed when a high ***F*** fs laser is used for excitation of the surface. However, at lower fs laser ***F*** the normal DIET process may be still operative [Bus96].

Confined systems like thin films or nanoparticles may offer additional advantages. The electronic temperature can become very high [Glo08] and decay slowly [Zhd04] in metal NPs compared to their bulk counterparts. The increase of the electronic temperature in nanostructures can increase the desorption yield, P_{des} according to $P_{des}\ \alpha\ (\boldsymbol{F}/\mathrm{d})^n$ [Nes04]. A plasmon-enhanced fs laser induced thermal desorption of water from quartz-supported Ag clusters was also observed [Kwi05].

Previously the photodesorption cross section and translational temperature of photodesorbed NO from Ag (111) and 8 nm Ag NPs with 3.1 eV fs laser pulses in the ***F*** regime between 0.02 – 2 mJ/cm^2 have been studied by using a QMS [Kim09]. In the following the summary of the previous results from this system and the motivation for the current study are presented.

The results from these studies show a number of interesting features, among them: The photodesorption yield of NO is roughly linear with ***F*** (***F*** < 2 mJ/cm^2) for both Ag

(111) and Ag NPs. On Ag (111) surfaces: i) roughly linear fluence dependence of photodesorption cross section was observed ii) the derived desorption cross section was comparable to those found for the same adsorption system with nanosecond pulses at somewhat higher photon energy, 3.5 eV; and iii) the translational temperatures were independent of ***F*** and also did not change significantly as compared to the results found at *hν* = 3.5 eV and nanosecond laser pulses. All these results suggest that in the laser fluence applied in this system a similar mechanism as proposed for molecules photodesorbed with ns laser pulses at *hν* = 3.5 eV, i.e., a DIET process is operative. If we compare the above observations with other systems studied before; for example NO on Pd (111) [Pry90], the super-linear dependence of the desorption yield on ***F***, the desorption cross section with fs laser pulses (~10^{-18} cm^2) being 10^4 times higher than the one found in ns laser pulses (~10^{-22} cm^2), the increase of translational temperature at higher ***F***, these characteristics of the DIMET/ electronic friction process are not observed in the present system, on the Ag (111) surface.

On the other hand for 8-nm Ag NPs, the desorption cross section of NO was ~500 times higher than that found from the same system when ns laser pulses are used. The very high cross section observed from Ag NPs with fs laser excitations was almost independent of ***F*** and an increase of the translational temperature of NO from Ag NPs starting from ***F*** = ~1 mJ/cm^2 was observed. These observations were explained based on the DIMET/friction model.

The above observations motivated us to study the dynamics of fs laser induced NO desorption further by measuring the excitations of the other degrees of freedom of the desorbing molecules, to unravel the possible mechanisms that result in the extremely high cross sections which are observed even at very low ***F*** on Ag NPs, and the increase of T_t at higher ***F***, which are not there in the case of Ag (111). Due to the very low output intensity of our laser however, we are not able to measure at higher fluences. And therefore measurements are performed only at low fluence (below the fluence at which the increase of T_t was observed in the previous QMS study). The obtained results are compared with the behavior observed for nanosecond laser induced desorption for the same system.

5.2. Experimental

The (1+1) REMPI technique was implemented to measure the state resolved final state energy distributions of NO molecules from Ag (111) and Ag NPs following fs laser irradiation. The experimental setup and measurement procedures are the same as those for ns pulses presented in *Chapter 4*. In this chapter fs laser pulses of 110 fs duration FWHM were produced by a Ti-Saphire mode-locked laser pumped by a pulsed Nd: YLF laser (Merlin). The laser beam was incident on the sample with *p*-polarization and at an angle of 45 ° from the surface normal at a repetition rate of 50 Hz. The intensity profile of the beam on the sample surface is shown in figure 5.1.

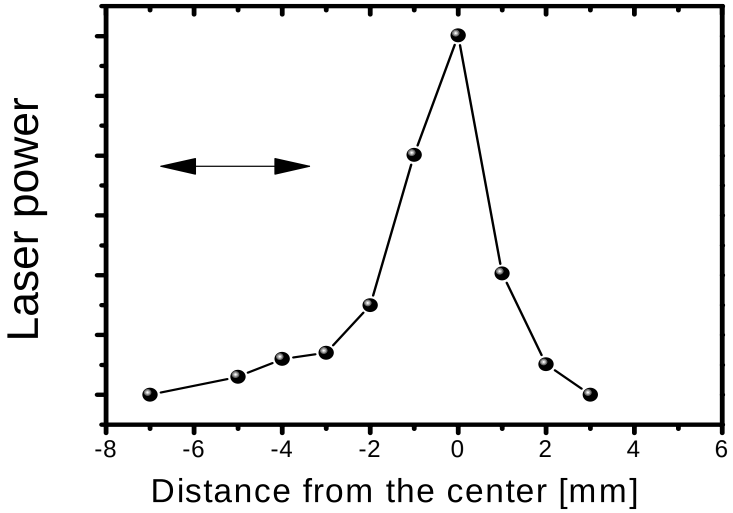

Figure 5.1.: Femtosecond laser beam intensity profile.

The maximum output intensity of our laser system was very low (output laser fluence, ***F*** ~ 0.08 mJ/cm^2), therefore our measurement was limited to lower laser fluence. A somewhat higher fluence, ***F*** = ~0.72 mJ/cm^2 was achieved by focusing the beam on the sample. Molecules desorbed along the surface normal were detected 28 mm away from the sample surface quantum selectively by a second laser (probe laser) as in *Chapter 4*. One of the difficulties in these measurements, especially the photodesorption measurements from Ag NPs, was to get a steady state adsorption/desorption equilibrium. As presented in the introduction the PCS of NO from Ag NPs caused by fs pulses is so high that the surface coverage is depleted quickly (a single laser pulse can desorb up to 50 % of the coverage even at very low laser fluence). To compensate the desorbed NO coverage we have to use a high NO background pressure (in the order of ~ 10^{-7}) and a longer adsorption time. Since the laser repetition rate is 50 Hz, opening the shutter for 1 second corresponds to irradiating the surface with 50 laser pulses but the desorption will be finished already in the first few (2 to 3) laser shots. The other laser pulses will not lead to any desorption signal, i.e., to 0 signal intensity. Therefore the average signal measured in 1 second shutter opening is very small.

The high background NO pressure together with the high transient NO desorption flux may perturb the final energy distribution of the desorbed molecules due to post-desorption collision (see section 5.4).

5.3. Results

In this section the results found from the state resolved measurements of photodesorbed NO from NO dimer-covered Ag surfaces (Ag (111) and 8 nm Ag NPs) induced by 3.1 eV (*p*-polarized) fs laser pulses are presented. The final state energy distributions of molecules desorbed by fs laser pulses are compared to those found for the same system by ns laser pulses. Moreover, the effect of the fs laser fluence on the final state energy distributions is presented.

Final state distributions

Rovibrationally resolved translational energy distributions of photodesorbed NO molecules induced by fs laser pulses from Ag NPs and Ag (111) surfaces were measured at two different laser fluences (0.08 and 0.72 mJ/cm^2). Figure 5.2 shows the rotational state dependence of the TOF spectra of NO molecules desorbed by 3.1 eV fs laser pulses at $\boldsymbol{F}$ = 0.08 mJ/cm^2 from NO dimer-covered 8-nm Ag NPs. As can be seen from the figure, the spectra shift to a faster pump-probe delay as the rotational state, *J”* is increased. The TOF spectra at lower *J”* are bimodal and the contribution of the slow component decreases with increasing *J”* and vanished at higher *J”* levels. The faster component shifts to the fast pump-probe delay and becomes narrower with increasing *J”*. The desorbed NO molecules from Ag (111) surfaces induced by fs laser at 3.1 eV and fluence 0.72 mJ/cm^2 show similar behavior (not shown). Similar features were also observed in the ns laser induced desorption results, which have been presented in *Chapter 4.*

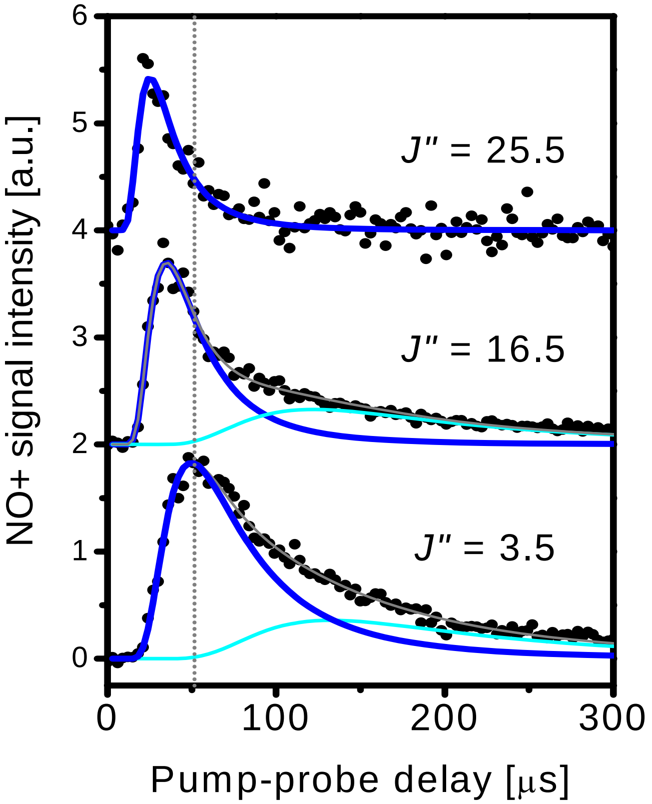

Figure 5.2.: TOF spectra of NO (v = 0, Ω = 1/2 and designated J" states) desorbed with 3.1 eV *p*-polarized fs laser pulses at fluence of 0.08 mJ/cm^2 from 8 nm Ag NPs.

Figure 5.3 shows a typical Boltzmann plot of photodesorbed NO (v = 0, pump-probe delay = 29 μs) from 8 nm Ag NPs induced by 3.1 eV femtosecond laser pulses at fluence 0.08 mJ/cm^2. As can be seen in the Boltzmann plot, it can be characterized by a straight line which gives a rotational temperature T_{rot} = 365 K. This value is smaller than the value found on the same particle size when ns laser pulses were used to desorb NO (~ 485 K at $h\nu$ = 3.5 eV). On the other hand, no significant difference on the rotational energy distributions of the desorbed NO molecules from the Ag (111) surface with nanosecond and femtosecond laser pulses was observed (T_{rot} = ~ 440 K for $h\nu$ = 3.5 eV ns laser pulses and T_{rot} = ~ 410 K for $h\nu$ = 3.1 eV fs laser pulses).

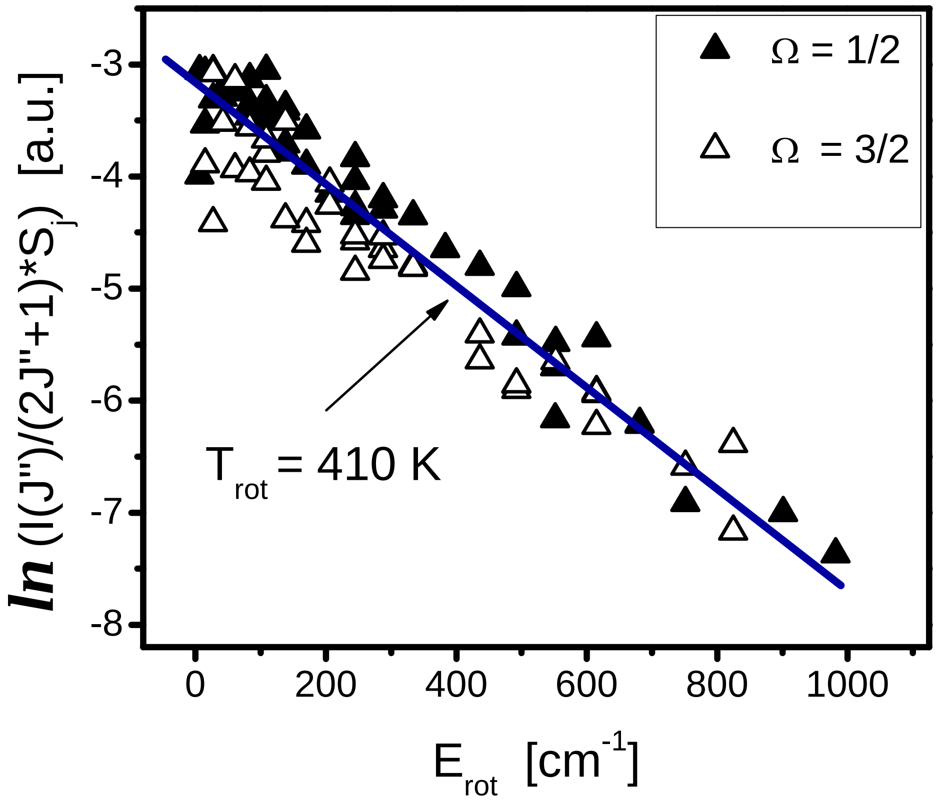

Figure 5.3.: Rotational distribution of NO ($v = 0$) desorbed with 3.1 eV *p*-polarized fs laser pulses from Ag (111) surface. The straight line fit represents the rotational Boltzmann distribution

To check the effect of ***F*** on the translational and rotational energy distributions of the desorbed NO, further measurements were conducted at the higher laser ***F*** obtained by focusing the beam on the sample. The results found at these two different laser fluencies, ***F*** = 0.08 mJ/cm^2 and three times focused beam (***F*** = ~0.72 mJ/cm^2) and the corresponding results found with hv = 3.5 eV ns laser desorption are summarized in Table 5.1. The translational temperatures are compared for J'' = 11.5 values (i.e., the T_t found by fitting the TOF spectra measured from photodesorbed NO in $v = 0$, $J'' = 11.5$, $\Omega = 1/2$ state, with *shifted* Maxwell Boltzmann function). The results clearly show that, translational temperatures of photodesorbed NO obtained with lower fluence (***F*** = 0.08 mJ/cm^2) femtosecond laser pulses are similar, within the experimental error, to those found with ns laser pulses. On the other hand, at ***F*** = 0.72 mJ/cm^2 the T$_t$ is smaller by more than 100 K compared to the results found on the same system but at lower fluence, ***F*** = 0.08 mJ/cm^2. The rotational distribution of photodesorbed NO from the Ag (111) surface is almost independent of ***F***. But on 8 nm Ag NPs, T$_{rot}$ of photodesorbed NO decreases from ~410 K at ***F*** = 0.08 mJ/cm^2 to ~300 K at ***F*** = ~ 0.72 mJ/cm^2.

Table 5.1: Summary of the translational and rotational temperature of NO desorbed with 3.1eV p-polarized fs laser pulses at ***F*** = 0.08 and 0.72 mJ/cm^2.

Substrate	*hv [eV]*	***F*** *(mJ/cm^2)*	*T_t^* [K]*	*T_{rot}^{**} [K]*
Ag (111)	3.1 (fs)	0.08	485	410
	3.5 (ns)	1.6	520	435
8 nm Ag NPs	3.1 (fs)	0.08	396	365
	3.1 (fs)	0.72	271	304
	3.5 (ns)	1.1	440	485

* The translational temperatures of photodesorbed NO in $v = 0$, $J'' = 11.5$ and $\Omega = 1/2$ state.

** The rotational temperature of photodesorbed NO ($v = 0$) with velocity of 950 m/s.

Figure 5.4 shows the translational-rotational correlations of fs laser desorbed NO from 8 nm Ag NPs and Ag (111) surfaces. For comparison the corresponding results measured by ns laser from the same system are shown (cross symbols). As can be seen from the results, at lower ***F*** a positive correlation, which is quite similar to the corresponding correlations found in ns laser measurements, are found. However, for ***F*** = 0.72 mJ/cm^2 there are only two data points at lower translational and rotational energies and therefore it is difficult to say more about the correlation (see figure 5.4, blue squares).

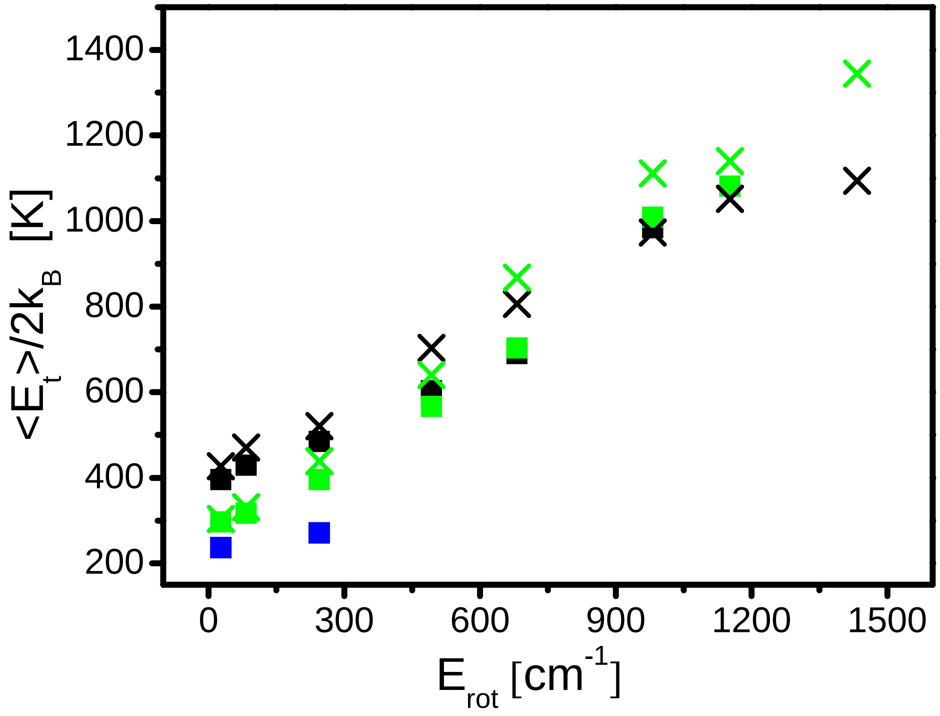

Figure 5.4.: Mean translational energy, plotted as a function of rotational energy of the particular rotational state probed, of NO desorbed with 3.1 eV fs laser pulses from Ag (111) (black squares), 8 nm Ag NPs at ***F*** = 0.08 mJ/cm^2 (green squares), and at ***F*** = 0.72 mJ/cm^2 (blue squares). The corresponding results found at 3.5 eV ns laser pulses from Ag (111) (black crosses), and 8 nm Ag NPs (green crosses) are also shown for comparison.

Due to poor signal to noise ratio of the REMPI spectra of photodesorbed NO molecules in the *v* = 1 state, it is very difficult to calculate the degree of vibrational excitations of photodesorbed NO induced by fs laser pulses from both Ag NPs and Ag (111) surfaces at both fluences. In other systems extremely high vibrational excitation of photodesorbed NO induced by femtosecond laser pulses from chemisorbed NO, ~2900 K in NO/Pd (111) [Bud93], ~3800 K in NO/NiO) [Eic98] is observed.

5.4. Discussion

On Ag (111) the translational and rotational energy distributions of photodesorbed NO and the correlation between them did not show significant changes for fs compared to ns laser excitations suggesting the basic nature of the excitation-deexcitation process did not change between the ns and fs laser desorption. Therefore, we expect the DIET model discussed in *Chapter 4* to be applicable also in fs laser desorption of NO from Ag (111) in the fluence range used in this study.

On the other hand the rotational energy of photodesorbed molecules by 3.1 eV fs laser pulses are found to be lower than the corresponding ones found at $h\nu$ = 3.5 eV ns laser pulses, but the T_t is not changed significantly. As mentioned in the introduction, in the same system the desorption cross section of NO from Ag NPs by 3.1 eV fs laser pulses is ~500 times higher than the corresponding result found with 3.5 eV ns laser pulses.

Now let's look first at the high cross section observed in the former study of this system by QMS. In the case of hot electron mediated femtochemistry, the confinement may have an influence on the T_{el}. According to previous study [Nes04] on thin films, lowering the film thickness may have a similar effect as increasing the fluence. In addition, in confined systems the electronic temperature is very high and cools down slowly [Zhd04, Glo08]. As a consequence, the hot electron mediated desorption depends sensitively on film thickness and the desorption probability is expected to scale $P_{des} \sim (F/d)^n$, where n is a film thickness dependent variable [Nes04]. The above properties suggested for thin films seem to be a general characteristic for confined systems and appear to apply also to NPs. Hence the observed high cross section in our system is likely to be achieved through multiple excitation (DIMET) processes. If the DIMET mechanism is the probable desorption mechanism for NO from Ag NPs, the next question is, why the translational and internal energies of the desorbed NO decrease for NPs when $\boldsymbol{F}$ is increased? In contradiction to the DIMET process which should result in highly excited desorbates [Bud93, Eic99, Kao93] our observation shows a decrease of translational and rotational temperatures with increasing $\boldsymbol{F}$. In fact a rapid decrease of the translational energy of desorbed O_2 induced by 3.1 eV 110 fs laser pulses from the O_2/Pt (111) system has been observed in the fluence range at which the crossover from single to multiple excitations is expected [Bus96]. Presumably our conditions might also correspond to the crossover from DIET to DIMET processes i.e., from the region where single excitations (DIET) are dominant to the region where multiple excitations become dominant.

Furthermore, in hot electron mediated desorption of NO induced by femtosecond laser pulses pronounced vibrational excitation is found [Pry90] which was explained based on a transient multiple population of the antibonding $2\pi^*$ orbital. In contrast, in the present system no detectable vibrationally excited NO molecules are found which lets us estimate that at most 1 % can desorb in the $v = 1$ state. Another model used to explain the fs laser induced desorption process is the friction model. In the limit of frictional energy transfer, only adsorbate levels near the Fermi level are populated instead of populating the adsorbate antibonding $2\pi^*$ orbital as in DIET/DIMET process. Therefore, the frictional model may result in a less vibrationally excited molecule if the available adsorbate resonance states near the Fermi level (if any) are not as strongly antibonding. However, the detailed dynamics of the desorption process depends on the 3D potential energy surface.

Another possibility for the observed decrease of final state energy distributions could be post-desorption collisions due to high density – in space and time – of desorbing NO. In addition, in fs laser measurements higher NO background pressures had to be used to avoid the quick depletion of NO dimers on the surface. Hence the post-desorption collisions among desorbates and with the background NO gas can perturb the measured energy distributions of the desorbed NO molecules [Bat87, Sim96].

In the following we roughly estimate the number of post-desorption collisions of the desorbing NO molecules: The pulse width of the fs laser used for desorption is ~110 fs. The density of the desorbing NO molecules in a 110 fs is similar to that of a three dimensional gas. For a typical velocity of about 950 m/s, the extent of the NO gas distribution at the end of the pulse duration/width is about 10^{-10} m from the surface. For about 50 % desorption (corresponds to desorption of ~200 NO molecules per nanoparticle per laser pulse [Kim09] which gives 2×10^{18} NO molecules/m^2), this results in NO gas density of about 2×10^{28} NO molecules/m^3. Assuming the collision cross section between NO molecules is constant at about 4×10^{-19} m^2 a mean free path of about ~10^{-10} m can be be derived from the above values. Since the distance between the sample and the ionization/detection point is 0.028 m, NO molecules will experience about ~10^7 collisions before reaching to the detection point. Such high number of collisions, ~10^7 collisions/NO could result in an adiabatic cooling of the desorbate analogous to a supersonic expansion [And65]. A large and correlated reduction in both the rotational and translational energies is also observed for NO molecules desorbing from NO dimer covered MgF_2 surface at 248 nm [Sim96].

Overall, unlike the other fs laser studies from various systems mentioned above in the fluence regime used in this study little evidence is observed for the role of DIMET/friction mechanisms except the large desorption cross section (~500 times higher than that found from the same system when ns laser pulses are used) found for desorbing molecules from Ag NPs in previous QMS measurements. This may be due to a large perturbance of the final energy distribution by multiple scattering of the desorbates.

5.5. Summary

In summary, we have studied fs laser induced desorption dynamics of NO from NO dimers adsorbed on Ag NPs and Ag (111) surfaces using a (1+1) REMPI detection technique. The translational and internal energy distributions and the observed T-R correlation of photodesorbed NO molecules from the Ag (111) surface suggests the accepted mechanism, TNI formation by hot electrons, is the probable mechanism also for fs desorption in the fluence regime used in this study. On the other hand on Ag NPs of mean diameter 8 nm on alumina film on NiAl (110) substrates, relative decreases of translational and rotational energies of desorbed molecules are observed which may be due to transition of a new mechanism (presumably DIMET/Friction) from the conventional desorption mechanism, DIET observed at $h\nu$ = 3.5 eV ns laser pulses. However, post-desorption collisions due to the high density in space and time, of NO could also account for the observed decrease of final state energy distributions.

Chapter 6

Summary and conclusions

The principal question of this work is focused on the particle size effects on the photochemistry of NO dimers adsorbed on alumina supported Ag NPs in the photon energy range between 2.3 and 4.7 eV, including the plasmon excitation at 3.5 eV. The experiments have been carried out under UHV conditions using mass-selected time-of-flight (MS-TOF), resonance-enhanced multiphoton photoionization (REMPI), and temperature programmed desorption (TPD) techniques. The main results and conclusions are summarized as follows.

At low temperature (< 77 K) NO is known to form a NO dimers on Ag (111) surfaces which upon heating or photon irradiation dissociates into monomers which partly desorb, or reacts to form N_2O and O. In our study on Ag NPs quite similar behavior was observed suggesting there is also dimerization of NO, and formation of the above mentioned products upon heating or photon irradiation. However the desorption peak temperatures of the reaction products were found to be lower on Ag NPs, and changing almost linearly with 1/R starting from the peak temperature found from the reference surface, Ag (111). This reduced interaction between NO dimers and the Ag NPs which scales with the inverse of the particle diameter (~surface to volume ratio) is discussed based on the electronic and geometrical nature of the size effects of the Ag NPs. Some of them are: the possible shift of the Ag *d*-band away from the Fermi level. Since the NO dimer's HOMO has some hybridization with the Ag *d*-electrons, this shift can weaken the adsorption energy. In addition, the reduction of the van der Waals dispersion forces (which sums over all the Ag atoms of the NP) with decreasing the Ag NP size is expected. Furthermore the size dependence of the ionization potential, possible changes of the surface structure, e.g., Ag-Ag bond contraction with decreasing size, and the geometrical confinement of the reactions on the nm scale are suggested as possible reasons for the observed size dependent desorption temperature of NO dimers and N_2O on Ag NPs.

We have also found clear size effects on the photochemistry of the adsorbed NO dimers on Ag NPs. For excitations off the plasmon resonance (photon energies of 2.3 and 4.7 eV), the photodesorption cross section (PCS) of NO increases roughly linearly with the surface to volume ratio (~1/R) of Ag NPs. This is explained by the confinement effect of hot electrons formed by the incoming photons which can lead to desorption via a transient negative ion state as on Ag (111). Since the sizes of the nanoparticles used in this study are much smaller than the mean free path of low energy electrons in Ag, the photogenerated hot electrons with in the volume of the Ag NPs ($\sim R^3$) can scatter with the surface ($\sim R^2$) several times. Such multiple scattering processes will increase the availability of hot electrons at the surface and correspondingly increase the desorption probability of the adsorbates which will then scale with the surface to volume ratio of the NP.

For excitation in the plasmon resonance (3.5 eV, *p*-polarized) a maximum enhancement of the PCS of NO (~43 times compared to the Ag (111) results) is found at the intermediate size of $D = \sim 5$ nm which then sharply decreases both with increasing and decreasing *D*. This peaked behavior is explained as due to the interplay of at least two opposing size effects. The rapid decrease of PCS at diameter above $D = \sim 5$ nm is attributed to the decreasing contribution of Landau damping with increasing *D,* while the steep decrease of PCS at diameter below ~5 nm is believed to be due to the reduction of the plasmon oscillator strength which scales with the total number of atoms in the NP.

Going beyond the macroscopic information; the detailed microscopic dynamics of the photoinduced process has been investigated. The results from the final state energy (translational, rotational, and vibrational) distributions in the desorbing NO molecules showed that the desorption process is non-thermal. This was found by measuring these energy distributions of the desorbing molecules at velocities 950 and 1500 m/s. In addition, the excitation mechanisms for translational and rotational degrees of freedom of these molecules are coupled in the desorption process while the vibrational excitation is decoupled from the other excitations.

Constant translational and internal energy distributions of photodesorbed NO molecules at $h\nu = 2.3$ and 3.5 eV excitations are found throughout the Ag NP size range. Furthermore the observed results are quite similar to those found for NO dimers on Ag (111) surfaces pointing that the accepted mechanism, TNI formation by hot electron attachment remains the most probable mechanism operating throughout the NP size range for 2.3 and 3.5 eV. From this result we suggest that the confinement of electrons and the PCS enhancement by plasmon excitation do not alter the individual desorption dynamics of NO, at least for $h\nu \leq 3.5$ eV.

At higher excitation photon energy (4.7 eV) and for small particles, however, a dramatic increase of both the translational and internal energies of the desorbed NO molecules are observed which suggests the emergence of a new mechanism. The first possibility is, the *d*-band hot hole mechanism. In this mechanism hot holes are formed by excitation of electrons from the Ag *d*-band to above the Fermi level. These hot holes can then attach to the adsorbate and excites it to a transient positive ion (TPI) state. Another path to the same excited molecule is the direct charge transfer (CT) mechanism. In this mechanism photon absorption can lead to hot holes in the adsorbate by direct excitation of electrons from the adsorbate (NO dimer) HOMO to the *s-p* orbitals above the Fermi level in the Ag NPs. Therefore, both processes can lead to desorption via a transient positive ion state of the adsorbate. The fact that this mechanism results in more energetic desorbates compared to the TNI mechanism can be explained by the fact that the molecules in the TPI state are more compact than in the TNI state, so that they can approach the surface closer and with higher velocity and therefore rebounce with a higher energy. The increasing contribution of these mechanisms with decreasing size is likely connected with the relative increase of surface atoms (which increases the contribution of localized *d*-holes at the surface) or the increasing number of NO dimers (which increases the direct CT mechanism), in proportion to the surface to volume ratio of the NPs.

References

[Ade98] M. Adelt, S. Nepijko, W. Drachsel, and H.-J. Freund. *Size-dependent luminescence of small palladium particles*. Chem. Phys. Lett. **291**, (1998) 425.

[Aes96] M. Aeschlimann, M. Bauer, S. Pawlik. *Competing nonradiative channels for hot electron induced surface photochemistry*, Chem. Phys. **205**, (1996) 127.

[Aes00] M. Aeschlimann, M. Bauer, S. Pawlik, R. Knorren, K. H. Bennemann. *Transport and dynamics of optically excited electrons in metals*, Appl. Phys. A **71**, (2000) 485.

[Aiy94] H. N. Aiyer, V. Vijayakrishnan, G. N. Subbanna, C. N. R. Rao. *Investgation of Pd clusters by the combined use of HREM, STM, high-energy spectroscopies and tunneling conductance measurements*. Surf. Sci. **313**, (1994) 392

[Ale88] M. A. Alexander, P. Andresen, R. Bacis, R. Bersohn, F. J. Comes, P. J. Dagdigian, R. N. Dixon, R. W. Field, G. W. Flynn, K.-H. Gericke, E. R. Grant, B. J. Howard, J. R. Huber, D. S. King, J. L. Kinsey, K. Kleinermanns, K. Kuchitsu, A. C. Luntz, A. J. McCattery, B. Pouilly, R. Vasudev, J. R. Wiesenfeld, C. Wittig, R. N. Zare. *A nomenclature for Λ – doublet levels in rotating linear molecules*. J. Chem. Phys. **89**, (1988) 1749.

[AlS94] K. Al-Shamery, I. Beauport, H.-J. Freund, H. Zacharias. *UV laser-induced desorption of CO from Cr2O3 (111). A fully quantum state resolved mapping of the desorbing species*. Chem. Phys. Letts. **222**, (1994) 107.

[AlS06] K. Al-Shamery. *Photochemistry at nanoparticulate surfaces*. J. Phys.: Condens. Matter **18**, (2006) S1581.

[And65] J. B. Anderson, and J. B. Fenn. *Velocity distributions in molecular beams from nozzle sources*. Phys fluids **8**, (1965) 780.

[Ant80] P. R. Antoniewicz. *Model for electron- and photon-stimulated desorption.* Phys. Rev. B **21**, (1980) 3811.

[Apa81] G. Apai, S.-T. Lee, and M. G. Mason. *Valence band formation in small silver clusters.* Solid State Communication **37**, (1981) 213.

[Avo89] Ph. Avouris, and R. Walkup. *Fundamental mechanisms of desorption and fragmentation induced by electronic transitions at surfaces*. Annu. Rev. Phys. Chem. **40**, (1989) 173.

[Bal07] B. Balamurugan, and T. Maruyama. *Size-modified d-bands and associated interband absorption of Ag nanoparticles*. J. Appl. Phys **102**, (2007) 034306.

[Bar86] C. E. Bartosch, N. S. Gluck, W. Ho, and Z. Ying. *Laser-surface-adsorbate interactions: Thermal versus photoelectronic excitation of Mo(CO)$_6$ on Si(111).* Phys. Rev. Letts. **57**, (1986) 1425.

[Bas01] C. Lopez-Bastiadas, J. A. Maytorena, and A. Liebsch. *Hot-electron dynamics at noble metal surfaces.* Phys. Rev. B **65**, (2001) 354171.

[Bat87] I. N. Natcha, R. R. Lucchese, and Y. Zeiri. *Effects of gas-phase collisions on particles rapidly desorbed from surfaces.* Physical Review B **36**, (1987) 4978.

[Bau99] M. Baumer, and H.-J. Freund. *Metal deposits on well-ordered oxide films*. Prog. Surf. Sci. **61** (1999) 127.

[Bau02] M. Baur, M. Aeschlimann. *Dynamics of excited electrons in metals, thinfilms, and nanostructures.* Journal of Electron Spectroscopy and Related Phenomena **124**, (2002) 225.

[Bau04] C. Baur, J.-P. Abid,, David Fermin, and H. H. Girault. *Ultrafast chemical interface scattering as an additional decay channel for nascent nonthermal electrons in small metal nanoparticles.* J. Chem. Phys. **120** (2004) 9302.

[Bau05] C. Bauer, J.-P. Abid, and H. Girault. *Size dependence investigations of hot electron cooling dynamics in metal/adsorbates nanoparticles.* Chem. Phys. **319**, (2005) 409.

[Ber52] C. R. Berry. *Electron diffraction from small crystals*. Phys. Rev. **88**, (1952) 596.

[Bil71] J. Billingsley, and A. B. Callear. *Investigation of the 2050 A system of the nitric oxide dimer.* J. Chem. Soci. Trans. Faraday Soc. **67**, (1971) 589.

[Bos02] J. Bosbach, C. Hendrich, F. Stietz, T. Vartanyan, and F. Trager. *Ultrafast dephasing of surface plasmon excitation in silver nanoparticles: Influence of particle size, shape, and chemical surrounding.* Phys. Rev. Letts. **25**, (2002) 257404.

[Bro95] W. A. Brown, P. Gardner, M. Perez Jigato, and D. A. King. *Characterization and orientation of adsorbed NO dimers on Ag(111) at low temperatures.* J. Chem. Phys. **102**, (1995) 7277.

[Bro95^a] W. A. Brown, P. Gardner, and D. A. King. *Very low temperature surface reaction: N$_2$O formation from NO dimers at 70 to 90 K on Ag (111).* J. Phys. Chem. **99,** (1995) 7065.

[Bro00] W. A. Brown, D. A. King. *NO chemisorption and reactions on metal surfaces: a new perspective.* J. Phys. Chem. B **104,** (2000) 2578.

[Bud88] F. Budde, A. V. Hamza, P. M. Ferm, G. Ertl, D. Weide, P. Anderesen, and H.-J. Freund. *Photodesorption of NO from Ni(100)-O.* Phys. Rev. Letts. **60**, (1988) 1518.

[Bud91] F. Budde, T. F. Heinz, M. M. T. Loy, J. A. Misewich, F. de Rougemont, and H. Zacharias. *Femtosecond time-resolved measurements of desorption*. Phys. Rev. Letts. **66**, (1991) 3024.

[Bud93] F. Budde, T. F. Heinz, A. Kalamarides, M. M. T. Loy, and J. A. Misewich. *Vibrational distributions in desorption induced by femtosecond laser pulses: coupling of adsorbate vibration to substrate electronic excitation.* Surf. Sci. **283**, (1993) 143.

[Bun88] S. A. Buntin, L. J. Richter, R. R. Cavanagh, and D. S. King. *Optically deriven surface reactions: evidence for the role of hot electrons.* Phys. Rev. Letts. **61**, (1988) 1321.

[Bun89] S. A. Buntin, L. J. Richter, D. S. King, and R. R. Cavanagh. *State-resolved evidence for hot carier driven surface reactions: Laser-induced desorption of NO from Pt(111)*. J. Chem. Phys. **91**, (1989) 6429.

[Bun93] S. A. Buntin, R. R. Cavanagh, and L. J. Richter. *Photodecomposition dynamics of Mo(CO)6/Si(111) 7x7: CO internal state and translational energy distributions*. J. Chem. Phys. **98**, (1993) 7651.

[Bus95] D. G. Busch, S. Gao, R. A. Pelak, M. F. Booth, W. Ho. *Femtosecond desorption dynamics probed by time-resolved velocity measurements*. Phys. Rev. Letts. **75**, (1995) 673.

[Bus96] D. G. Busch and W. Ho. *Direct observation of the crossover from single to multiple excitations in femtosecond surface photochemistry*. Phys. Rev. Letts. **77**, (1996) 1338.

[Cam97] C. T. Campbell. *Ultrathin metal films and particles on oxide surfaces: structural, electronica and chemisorptive properties*. Surf. Sci. Rep. **27**, (1997) 1.

[Car01] C. I. Carlisle, D. A. King. *Direct molecular imaging of NO monomers and dimers and s surface reaction on Ag {111}.* J. Phys. Chem. B **105**, (2001) 3886.

[Cav93] R. R. Cavanagh, D. S. King, J. C. Stephenson, and T. F. Heinz. *Dynamics of nonthermal reactions: Femtosecond surface chemistry.* J. Phys. Chem. **97**, (1993) 786.

[Che98] F. Chen, and H. Guo. *Influence of the ground-state potential on the product rotational/translational correlation in the photon-stimulated desorption of NO*. Chem. Phys. Letts. **286**, (1998) 205.

[Che06] M. Chen, and D. W. Goodman. *Catalytically active gold: from nanoparticles to ultrathin films.* Acc. Chem. Res. **39**, (2006) 739.

[Chu83] T. J. Chuang. *Laser-induced gas-surface interaction*. Surf. Sci. Rep. **3**, (1983) 1.

[Chu94] P. M. Chu, S. A. Buntin, L. J. Richter, and R. R. Cavanagh. *Photodecomposition of Mo(CO)6/Si(111): CO state-resolved evidence for excited state relaxation and quenching.* J. Chem. Phys. 101, (1994) 2929.

[Chu06] E. V. Chulkov, A. G. Borisov, J. P. Gauyacq, D. Sanchez-Portal, V. M. Silkin, V. P. Zhukov, and P. M. Echenique. *Electronic excitations in metals and at metal surfaces.* Chem. Rev. **106**, (2006) 4160.

[Cro62] C. R. Crowell, W. G. Spitzer, L. E. Howarth, and E. E. LaBate. *Attenuation length measurements of hot electrons in metal films.* Phys. Rev. **127**, (1962) 2006.

[Dai95] H.-L. Dai, and W. Ho (eds). *Laser spectroscopy and photochemistry on metal surfaces,* Vol. 5, World Scientific, Singapore, 1995.

[deJ90] A. M. de Jong, and J. W. Niemantsverdriet. *Thermal desorption analysis: comparative test of ten commonly applied procedures.* Surf. Sci. **233**, (1990) 355.

[Del95] S. Deliwala, R. J. Finlay, J. R. Goldman, T. H. Her, W. D. Mieher, E. Mazur. *Surface femtochemistry of O2 and CO on Pt (111)*. Chem. Phys. Letts. **242**, (1995) 617.

[Del99] N. Del Fatti, C. Flytzanis, F. Vallee. *Ultrafast induced electron-surface scattering in a confined metallic system.* Appl. Phys. B **68**, (1999) 433.

[Dra02] W. Drachsel, M. Adelt, N. Nilius, H.-J. Freund. *Cathodoluminescence of small silver particles on Al_2O3 / NiAl (110).* Journal of Electron Spectroscopy and Related Phenomena **122**, (2002) 239.

[Eas98] A. L. L. East. *The 16 valence electronic states of nitric oxide dimer $(NO)_2$*. J. Chem. Phys**.** **109**, (1998) 2185.

[Ech00] P. M. Echenique, J. M. Pitarke, E. V. Chulkov, A. Rubio. *Theory of inelastic lifetimes of low-energy electrons in metals*. Chem. Phys. **251**, (2000) 1.

[Ech04] P. M. Echenique, R. Berndt, E. V. Chulkov, Th. Fauster, A. Goldmann, and U. Hoefer. *Decay of electronic excitations at metal surfaces*. Surf. Sci. Rep. **52**, (2004) 219.

[Ehr61] G. Ehrlich. *Kinetics and experimental basis of flash desorption*. J. Appl. Phys. **32**, (1961) 4.

[Eic96] G. Eichhorn, M. Richter, K. Al-Shamery, H. Zacharias. *Vibrational population in femtosecond UV laser desorption of NO from NiO (100)*. Surf. Sci. **368**, (1996) 67.

[Eic98] G. Eichhorn, M. Richter, K. Al-Shamery, H. Zacharias. *Time-correlated laser desorption of NO from NiO (100) / Ni (100).* Chem. Phys. Letts. **289**, (1998) 367.

[Ell05] A. Ellis, M. Feher, and T. Wright. *Electronic and photoelectron spectroscopy. Fundamentals and case studies*. Cambridge University Press, Cambridge, 2005.

[End00] A. Endou, N. Ohashi, K. Yoshizawa, S. Takami, M. Kubo, A. Miyamato, and E. Broclawik. *Comparative investigation on the adsorption properties of precious metal clusters toward NO: A density functional study*. J. Phys. Chem. B **104**, (2000) 5110.

[Eve05] F. Evers, C. Rakete, K. Watanabe, D. Menzel, and H.-J. Freund. *Two-photon photoemission from silver nanoparticles on thin alumina films: Role of plasmon excitation.* Surf. Sci. **593**, (2005) 43.

[Eve06] F. Evers. *Comparative study of silver nanoparticles and silver (111) by means of femtosecond laser pulses*. Dissertation, FU Berlin 2006.

[Fau96] A. E. Faulhaber, B. A. Smith, J. K. Andersen, and J. Z. Zhang. *Femtosecond electronic relaxation dynamics in metal nano-particles: Effects of surface and size confinement.* Mol. Cryst. Liq. Cryst. **283**, (1996) 25.

[Fis10] H.-J. Fisher-Wolfarth, J. A. Farmer, J. M. Flores-Camacho, A. Genest, I. V. Yudanov, N. Roesch, C. T. Campbell, S. Schauermann, H.-J. Freund. *Particle size dependent heats of adsorption of CO on supported Pd nanoparticles as measured with a single crystal microcalorimeter*. Phys. Rev. B. *Rapid Communication*. accepted

[Fra90] R. Franchy, S. K. So, and W. So. *Photodesorption of NO on Ag (111) at 80 K.* Vacuum **41**, (1990) 284.

[Fri06] C. Frischkorn, and M. Wolf. *Femtochemistry at metal surfaces: Nonadiabatic reaction dynamics*. Chem. Rev. **106**, (2006) 4207.

[Fuk93] K. Fukutani, M.-B. Song, and Y. Murata. *Ultraviolet-laser-induced desorption of CO and NO from Pt surfaces*. Faraday Discuss. **96**, (1993) 105.

[Fuk93^a] K. Fucutani, A. Peremans, K. Mase, and Y. Murata. *Photo-stimulated desorption of NO from a Pt (001) surfaces*. Surf. Sci. **283**, (1993) 158.

[Fuk93^b] K. Fucutani, A. Peremans, K. Mase, and Y. Murata. *Photodesorption of NO from Pt (001) at $\lambda = 193, 248,$ and 352 nm.* Phys. Rev. B **47**, (1993-I) 4007.

[Gad90] J. W. Gadzuk, L. J. Richter, S. A. Buntin, D. S. King, and R. R. Cavanagh. *Laser-excited hot-electron induced desorption: a theoretical model applied to NO/Pt (111).* Surf. Sci. **235**, (1990) 317.

[Gao95] S. Gao, D. G. Busch, W. Ho. *Femtosecond dynamics of electron-vibrational heating and desorption.* Surf. Sci. **344**, (1995) L1252.

[Gar82] W. Garly, J. H. Miller, K. C. Smyth. *Resonantly enhanced two-photon photoionization of NO in an atmospheric flame*. J. Chem. Phys. **76**, (1982) 3483.

[Gar03] A. Garcia-Lekue, J. M. Pitarke, E. V. Chulkov, A. Liebsch, P. M. Echenique. *Role of occupied d bands in the dynamics of excited electrons and holes in Ag.* Phys. Rev. B **68**, (2003) 045103.

[Gat94] G. A. Gates, G. R. Darling, and S. Holloway. *A theoretical study of the vibrational excitation of NO/Ag (111).* J. Chem. Phys. **101**, (1994) 6281.

[Glo08] A. Gloskovskii, D. A. Valdaitsev, M. Cinchetti, S. A. Nepijko, J. Lange, M. Aeschlimann, M. Bauer, M. Klimenkov, L. V. Viduta, P. M. Tomchuk, and G. Schoenhense. *Electron emission from films of Ag and Au nanoparticles excited by a femtosecond pump-probe laser*. Phys. Rev. B **77**, (2008) 195427.

[Gui04] C. Guillon, P. Langot, N. Del Fatti, F. Vallee. *Ultrafast surface plasmon resonance Landau damping and electron kinetics in metal nanoparticles*. Proc. of SPIE **5352**, (2004) 65.

[Guo97] H. Guo, and F. Chen. *Dynamics of substrate mediated photodesorption: The role of the excited state potential*. Faraday Discuss. **108**, (1997) 309.

[Guo97^a] H. Guo, and L. Liu. *Perturbative treatements of photo-stimulated desorption and dissociation on metal surfaces induced by single and multiple electronic transitions*. Surf. Sci. **372**, (1997) 337.

[Guo99] H. Guo, P. Saalfrank, and T. Siedeman. *Theory of photoinduced surface reactions of admolecules*. Prog. in Sur. Sci. **62**, (1999) 239.

[Hal86] W. P. Halperin. *Quantum size effects in metal particles*. Rev. Mod. Phys. **58**, (1986) 533.

[Hal99] V. Halte, J.-Y. Bigot, B. Palpant, M. Broyer, B. Prevel, and A. Perez. *Size dependence of the energy relaxation in silver nanoparticles embedded in dielectric matrices.* Appl. Phys. Letts. **75**, (1999) 3799.

[Ham96] B. Hammer, Y. Morikawa, J. K. Nørskov. *CO chemisorption at metal surfaces and overlayers.* Phys. Rev. Letts. **76**, (1996) 2141.

[Har95] S. M. Harris, S. Holloway, and G. R. Darling. *Hot electron mediated photodesorption: A time-dependent approach applied to NO/Pt(111)*. J. Chem. Phys. **102**, (1995) 8235.

[Har95^a] S. M. Harris, S. Holloway, E. Hasselbrink. *A theoretical study of the photodesorption of NO/Pt (111).* Nuclear Instruments and Methods in Physics Research B **101**, (1995) 31.

[Has90] E. Hasselbrink. *Coupling of the rotational and translational degrees of freedom in molecular DIET: a classical trajectory study*. Chem. Phys. Letts. **170**, (1990) 329.

[Has90^a] E. Hasselbrink, S. Jakubith, S. Nettesheim, M. Wolf, A. Cassuto, and G. Ertl. *Cross sections and NO product state distributions resulting from substrate mediated photodissociation of NO_2 adsorbed on Pd (111)*. J. Chem. Phys. **92**, (1990) 3154.

[Has95] E. Hasselbrink, in, *Laser spectroscopy and photochemistry on Metal Surfaces*, eds. H.-L. Dai, W. Ho, Vol. 5, World Scientific, Singapore, 1995.

[Hei99] U. Heiz, A. Sanchez, S. Abbet, and W.-D. Schneider. *Catalytic oxydation of carbon monoxide on monodispersed platinum clusters: each atom counts*. J. Am. Chem. Sco. **121** (1999) 3214.

[Hen92] C. R. Henry, C. Chapon, C. Goyhenex, and R. Monot. *Size effects in the CO chemisorption on palladium clusters supported on magnesium oxide*. Surf. Sci. **272**, (1992) 283.

[Hen03] C. Hendrich, J. Bosbach, F. Stietz, F. Hubenthal, T. Vartanyan, and F. Traeger. *Chemical interface damping of surface plasmon excitation in metal nanoparticles: a study by persistent spectral hole burning*. Appl. Phys. B **76**, (2003) 869.

[Her50] G. Herzberg. *Molecular spectra and molecular structure I, Spectroscopy of diatomic molecules*, 2nd Edn. Van Nostrand Reinhold, New York, NY, 1950. and G. Herzberg, and J. W. T. Spinks. *Molecular spectra and molecular structure I. Spectra of diatomic molecules,* 2nd Edn. Van Nostrand Reinhold, New York, NY, 1950.

[Her98] T.-H. Her, R. J. Finlay, C. Wu, and E. Mazur. *Surface femtochemistry of $CO/O_2/Pt$ (111): The important of nonthermalized substrate electrons*. J. Chem. Phys. **108**, (1998) 8595.

[Hil01] A. Hilger, M. Tenfelde, U. Kreibig. *Silver nanoparticles deposited on dielectric surfaces.* Appl. Phys. B **73**, (2001) 361.

[Hog07] T. Hoger, D. Grimmer, H. Zacharias. *UV laser desorption of nitric oxide from semiconducting C_{60}/Cu(111)*. Appl. Phys. A **88**, (2007) 449.

[Hov98] H. Hoevel, B. Girmm, M. Pollmann, and B. Reihl. *Cluster-substrate interaction on a femtosecond time scale reviealed by a high-resolution photoemission study of the fermi-level onset*. Phys. Rev. Letts. **81**, (1998) 4608.

[Hov01] H. Hoevel. *Clusters on surfaces: high-resolution spectroscopy at low temperatures*. Appl. Phys. A **72**, (2001) 295.

[Hov04] H. Hoevel, I. Barke, H.-G. Boyen, P. Ziemann, M. G. Gamier, and P. Oelhafen. *Photon energy dependence of the dynamic final state effect for metal clusters at surfaces.* Phys. Rev. B **70**, (2004) 045424.

[Jac86] D. C. Jacobs, and R. N. Zare. *Reduction of 1 + 1 resonance enhancement MPI spectra to populations and alignment factors*. J. Chem. Phys. **85**, (1986) 5457.

[Jac95] R. C. Jackson, J. C. Polanyi, and P. Sjoeall. *Photodissociation dynamics of $(NO)_2$ on LiF(001): Charachterization of vibrationally excited NO fragments*. J. Chem. Phys. **102**, (1995) 6308.

[Jae91] R. M. Jaeger, H. Kuhlenbeck, H.-J. Freund, M. Wuttig, W. Hoffmann, R. Franchy, and H. Ibach. *Formation of well ordered aluminum oxide overlayer by oxidation of NiAl (110).* Surf. Sci. **259**, (1991) 235.

[Jig99] M. P. Jigato, D. A. King, A. Yoshimori. *The chemisorption of spin polarized NO on Ag (111)*. Chem. Phys. Letts. **300** (1999) 639.

[Jor92] J. Jortner. *Cluster size effects*. Z. Phys. D **24**, (1992) 247.

[Kam02] M. Kampling, K. Al-Shamery, H.-J. Freund, M. Wilde, K. Fukutani, and Y. Murata. *Surface photochemistry on confined systems: UV-laser induced photodesorption of NO from Pd-nanostructures on Al_2O_3*. Phys. Chem. Chem. Phys. **4**, (2002) 2629.

[Kel03] K. L. Kelly, E. Coronado, L. L. Zhao, and G. C. Schatz. *The optical properties of metal nanoparticles: the influence of size, shape, and dielectric environment*. J. Phys. Chem. B **107**, (2003) 668.

[Ken06] C. Kennerknecht, S. Dantscher, W. Pfeiffer, O. Autzen, C. Wesenberg, E. *Hasselbrink. Electron dynamics in a heterogeneous system: thin Ag films on Si(100)*. Surface Science **600**, (2006) 4269.

[Kid96] R. T. Kidd, S. R. Meech, D. Lennon. *Enhanced photodesorption of NO on roughened silver surfaces.* Chem. Phys. Letts. 262, (1996) 142.

[Kid99] R. T. Kidd, D. Lennon, and S. R. Meech. *Comparative study of the primary photochemical mechanisms of nitric oxide and carbonyl sulfide on Ag (111)*. J. Phys. Chem. B **103**, (1999) 7480.

[Kid00] R. T. Kidd, D. Lennon, and S. R. Meech. *Surface plasmon enhanced substrate mediated photochemistry on roughened silver.* J. Chem. Phys. **113**, (2000) 8276 .

[Kim02] C. M. Kim, C.-W. Yi, and D. W. Goodman. *Adsorption and reaction of NO on Cu (100): An infrared reflection absorption spectroscopic study at 25 K*. J. Phys. Chem. B **106**, (2002) 7065.

[Kim09] K. H. Kim. *Enhancement of photoinduced processes on supported Ag nanoparticles compared to a flat Ag surface*. Ph.D. thesis FU Berlin (2009).

[Kin75] D. A. King. *Thermal desorption from metal surfaces: A review.* Surf. Sci. **47**, (1975) 384.

[Kre85] U. Kreibig, and L. Genzel. *Optical absorption of small metallic particles*. Surf. Sci. **156**, (1985) 678.

[Kre95] U. Kreibig, and M. Vollmer. *Optical properties of Metal clusters*. Springer series in Material Science, Vol. 25 Springer-Verlag Berlin Heidelberg, 1995.

[Kre05] G. Kresse, M. Schmid, E. Napetschnig, M. Shishkin, L. Koehler, P. Varga. *Structure of the ultrathin aluminum oxide film on NiAl (110)*. Science **308**, (2005) 1440.

[Kre10] H.J. Kreuzer and D. Menzel, personal communication.

[Kul03] M. Kulawik, N. Nilius, H.-P. Rust, and H.-J. Freund. *Atomic structure of antiphase domain boundaries of a thin Al_2O_3 film on NiAl (110).* Phys. Rev. Lett. **91**, (2003) 256101.

[Kwi05] S. Kwiet, D. E. Starr, A. Grujic, M. Wolf, and A. Hotzel. *Femtosecond laser induced desorption of water from silver nanoparticles.* Appl. Phys. B **80**, (2005) 115.

[Lib94] J. Libuda, F. Winkelmann, M. Baeumer, H.-J. Freund, Th. Bertrams, H. Neddermeyer, K. Mueller. *Structure and defects of an ordered alumina film on NiAl (110)*. Surf. Sci. **318**, (1994) 61.

[Lie93] A. Liebsch. *Surface plasmon dispersion and size dependence of Mie resonance: Silver versus simple metals*. Physical Review B **48**, (1993) 11317.

[Lin06] C. D. Lindstrom, and X.-Y. Zhu. *Photoinduced electron transfer at molecule-metal interface.* Chem. Rev. **106**, (2006) 4281.

[Lin07] C.-M. Lin, T.-L. Hung, Y.-H. Huang, K.-T. Wu, M.-T. Tang, C.-H. Lee, C. T. Chen, and Y. Y. Chen. *Size-dependent lattice structure of palladium studied by x-ray absorption spectroscopy*. Phys. Rev. B **75**, (2007) 125426.

[Lud93] A. Ludviksson, C. Huang, H. J. Jaensch, and R. M. Martin. *Isotopic studies of the interaction of NO on silver surfaces*. Surf. Sci. **284**, (1993) 328.

[Lun06] A. C. Luntz, M. Persson, S. Wagner, C. Frischkorn, and M. Wolf. *Femtosecond laser induced associative desorption of H_2 from Ru (0001): Comparision of "first principles" theory with experiment.* J. Chem. Phys. **124**, (2006) 244702.

[Mai07] S. A. Maier. *Plasmonic: Fundamental and applications*. Springer, New York, NY, 2007.

[Mal82] W. G. Mallard, J. H. Miller, and K. C. Smyth. *Resonantly enhanced two-photon photoionization of NO an atmospheric flame*. J. Chem. Phys. **76**, (1982) 3482.

[ManDy] Sirah Cobra-Stretch dye laser user's manual

[ManYg] Quanta-Ray Lab-series: Pulsed Nd:YAG Lasers, preliminary user's manual

[Mas75] J. Mason. *The dimeric nitrogen oxides. Part I. Electronic absorption of the nitrogen oxide dimer, and comparision of observed and calculated spectra for dinitrogen dioxide, trioxide, and teraoxide.* J. Chem. Sos., Dalton Trans. (1975) 19.

[Mas91] K. Mase, S. Mizuno, Y. Achiba, and Y. Murata. *Photostimulated desorption of NO on Pt (001) studied with a multiphoton ionization technique*. Surf. Sci. **242**, (1991) 444.

[Mas92] K. Mase, K. Fukutani, and Y. Murata. *Adsorption state selectivity of ultravioleta-laser-stimulated desorption of NO chemisorbed on Pt (001) at 80 K studied by (1+1)-resonance-enhanced multiphoton ionization*. J. Chem. Phys. **96**, (1992) 5523.

[Mas96] R. I. Masel. *Principle of adsorption and reaction on solid surfaces*. Wiley, New York, NY, 1996.

[Mat05] V. E. Matulis, O. A. Ivashkevich, V. S. Gurin. *Interaction of nitric oxide and nitric oxide dimer with silver clusters*. Computing Letters (CoLe) **1**, (2005) 253 .

[Men64] D. Menzel, R. Gomer. *Desorption from metal surfaces by low-energy electrons*. J. Chem. Phys. **41**, (1964) 3311.

[Men75] D. Menzel in: *Interactions on Metal Surfaces,* ed. R. Gomer, Topics in Applied Physics series, Vol. 4, Springer-Verlag Berlin, Heidelberg, New York, 1975.

[Men94] M. Menges, B. Baumeister, K. Al-Shamery, H.-J. Freund, C. Fischer, and P. Andresen. *Dynamical studies of UV-laser-induced NO-desorption from the polar NiO (111) versus the nonpolar NiO (100) surfaces*. J. Chem. Phys. **101**, (1994) 3318.

[Mer03] M. Merschdorf, W. Pfeiffer, S. Voll, and G. Gerber. *Electron gas cooling in Ag nanoparticles on graphite.* Phys. Rev. B **68**, (2003) 155416.

[Mis92] J. A. Misewich, T. F. Heinz, and D. M. Newns. *Desorption induced by multiple electronic transitions.* Phys. Rev. Letts. **68**, (1992) 3737.

[Mis95] J. A. Misewich, T. F. Heinz, P. Weigand, and A. Kalamarides, in *laser spectroscopy and photochemistry on metal surfaces*, eds. H.-L. Dai and W. Ho, advanced series in physical chemistry series, Vol. 5, world scientific, Singapor, 1995.

[Mol02] R. A. Molina, D. Weinmann, and R. A. Jalabert. *Oscillatory size dependence of the surface plasmon linewidth in metallic nanoparticles*. Phys. Rev. B **65**, (2002) 155427.

[Mol03] R. A. Molina, D. Weinmann, and R. A. Jalabert. *Oscillatory behaviour and enhancement of the surface plasmon linewidth in embedded noble metal nanoparticles.* Eur. Phys. J. D **24**, (2003) 127.

[Mul92] Th. Mull, B. Baumeister, M. Menges, H.-J. Freund, D. Weide, C. Fischer, and P. Andresen. *Bimodal velocity distributions after ultraviolet-laser-induced desorption of NO from oxide surfaces. Experiments and results of model calculations.* J. Chem. Phys. **96**, (1992) 7108.

[Mur95] Y. Murata, and K. Fukatani, in *laser spectroscopy and photochemistry on metal surfaces*, eds. H.-L. Dai and W. Ho, advances in physical chemistry series, Vol. 5, world scientific, Singapore, (1995).

[Mus06] O. L. Muskens, N. D. Fatti, and F. Valle'e. *Femtosecond response of a single metal nanoparticle.* Nano Letters **6**, (2006) 552.

[Myl95] K. B. Myli, S. R. Coon, V. H. Grassian. *Photon-induced reactions of aromatics adsorbed on rough and smooth silver surfaces*. J. Phys. Chem. **99**, (1995) 16407.

[Nak06] H. Nakamura, and K. Yamashita. *Theoretical study of the photodesorption mechanism of nitric oxide on a Ag (111) surface: A nonequilibrium Green's function approach to hot-electron tunneling*. J. Chem. Phys. **125**, (2006) 084708.

[Nar04] R. Narayanan, and M. El-Sayed. *Size-dependent catalytic activity of platinum nanoparticles in colloidal solution.* Nano Letters **4**, (2004) 1343.

[Nat88] W. C. Natzle, D. Padowitz, and S. J. Sibener. *Ultraviolet laser photodesorption of NO from condensed films: Translational and internal energy distributions*. J. Chem. Phys. **88**, (1988) 7975.

[Neg08] C. F. A. Negre, and C. G. Sa'nchez. *Atomistic structure dependence of the collective excitation in metal nanoparticles*. J. Chem. Phys. **129**, (2008) 034710.

[Nes04] M. Nest, and P. Saalfrank. *Enhancement of femtosecond-laser-induced molecular desorption by thin metal films*. Phys. Rev. B **69**, (2004) 235405.

[New91] D. M. News, T. F. Heinz, and J. A. Misewich. *Desorption by femtosecond laser pulses: An electron-hole effect?* Prog. Theor. Phys. Suppl. **106**, (1991) 411.

[Nie07] J. W. Niemantsverdriet. *Spectroscopy in catalysis An introduction, 3rd ed.*, Wiley-VCH Ver GMbH and Co. KGA, 2007.

[Nil00] N. Nilius, N. Ernst, H.-J. Freund. *Photon emission spectroscopy of individual oxide-supported silver clusters in the STM*. Phys. Rev. Lett. **84**, (2000) 3994.

[Pal92] R. E. Palmer, and P. J. Rous. *Resonances in electron scattering by molecules on surfaces*. Rev. Mod. Phys. **64**, (1992) 383.

[Paw97] S. Pawlik, M. Bauer, and M. Aeschlimann. *Lifetime difference of photoexcited electrons between intraband and interband transitions*. Surf. Sci. **377-379**, (1997) 206.

[Per93] A. Peremans, K. Fukutani, K. Mase, and Y. Murata. *UV photodesorption of CO from Pt (001) at 193 nm investigated by state-selective detection*. Surf. Sci. **283**, (1993) 189.

[Pet97] H. Petek, and S. Ogawa. *Femtosecond time-resolved two-photon photoemission studies of electron dynamics in metals*. Prog. Surf. Sci. **56**, (1997) 239.

[Pry90] J. A. Prybyla, T. F. Heinz, J. A. Misewich, M. M. T. Loy, and J. H. Glownia. *Desorption induced by femtosecond laser pulses.* Phys. Rev. Lett. **64**, (1990) 1537.

[Rak03] C. Rakete. Photoemission *und photodesorption von NO auf NiO und silberclustern mit femtosekunden-laserpulsen*. FU Berlin 2003.

[Rao92] C. N. R. Rao, V. Vijayakrishnan, A. K. Santra, and M. W. J. Prins. *Dependence of the reactivity of Ag and Ni clusters deposited on solid substrates on the cluster size*. Angew. Chem. Int. Ed. Engl. **31**, (1992) 1062.

[Rao02] C. N. R. Rao, G. U. Kulkarni, P. J. Thomas, and P. P. Edwards. *Size-dependent chemistry: Properties of nanocrystals.* Chem. Eur. J. **8**, (2002) 29.

[Rei04] P.-G. Reinhard, E. Suraud. *Introduction to cluster dynamics*. Wiley-VCH, Weinheim, (2004).

[Red62] P. A. Redhead. *Themal desorption of gases*. Vacuum **12**, (1962) 203.

[Red64] P. A. Redhead. *Interaction of Slow Electrons with Chemisorbed Oxygen.* Can. J. Phys. **42**, (1964) 886.

[Req05] J. Requejo-Isidro, R. del Coso, J. Solis, J. Gonzalo, and C. N. Afonso. *Role of surface-to-volume ratio of metal nanoparticles in optical properties of Cu:Al_2O_3 nanocomposite films*. Appl. Phys. Letts. **86**, (2005) 193104.

[Ric88] L. J. Richter, S. A. Buntin, R. R. Cavanagh, and D. S. King. *Non-Boltznamm rotational and inverted spin-orbit state distributions for laser-induced desorption of NO from Pt (111)*. J. Chem. Phys. **89** (1988) 5344.

[Ric91] L. J. Richter, S. A. Buntin, D. S. King, and R. R. Cavanagh. *Constraints on the use of polarization and angle-of-incidence to characterize surface photoreactions.* Chem. Phys. Letts. **186**, (1991) 423.

[Ric92] L. J. Richter, S. A. Buntin, D. S. King, and R. R. Cavanagh. *State-resolved studies of the laser-induced desorption of NO from Si (111): Low coverage results.* J. Chem. Phys. **96** (1992) 2324.

[Rod90] J. A. Rodriguez. *The adsorption of nitric oxide, pyridine, and sulfur dioxide on silver: a quantum-chemical study.* Surf. Sci. **226**, (1990) 101.

[San05] E. E. Santiso, A. M. George, C. H. Turner, M. K. Kostov, K. E. Gubbins, M. B.-Nardelli, M. S.-Bartkowiak. *Adsorption and catalysis the effect of confinement on chemical reactions.* Appl. Surf. Sci. **252**, (2005) 766.

[Saa06] P. Saalfrank, M. Nest, I. Andrianov, T. Klamroth, D. Kroener, and S. Beyvers. *Quantum dynamics of laser-induced desorption from metal and semiconductor surfaces, and related phenomena*. J. Phys.: Condens. Matter **18**, (2006) S1425.

[Sch06] M. Schnippering, M. Carrara, A. Foelske, R. Koetz, and D. J. Fermin. *Electronic properties of Ag nanoparticle arrays. A Kelvin probe and high resolution XPS study*. Phys. Chem. Chem. Phys. **9**, (2007) 725.

[Sch07] T. Schalow, B. Brandt, D. E. Starr, M. Laurin, S. K. Shaikhutdinov, S. Schauermann, J. Libuda, and H.-J. Freund. *Particle size dependent adsorption and reaction kinetics on reduced and partially oxidized Pd nanoparticles.* Phys. Chem. Chem. Phys. **9**, (2007) 1347.

[Sei91] M. Seidl, K.-H. Meiwes-Broer, M. Brack. *Finite-size effects in ionization potentials and electron affinities of metal clusters.* J. Chem. Phys. **95**, (1991) 1295.

[Sim96] C.J.S.M. Simpson, P.T. Griffiths, J.M. Curry, M. Towrie. *The photolysis of NO dimers, adsorbed on an MgF_2 surface, at 248 nm.* Chem. Phys. Letts. **250**, (1996) 342.

[So89] S. K. So, R. Franchy, and W. Ho. *The adsorption and reactions of NO on Ag (111) at 80 K.* J. Chem. Phys. **91**, (1989) 5701.

[So91] S. K. So, R. Franchy, and W. Ho. *Photodesorption of NO from Ag (111) and Cu (111)*. J. Chem. Phys. **95**, (1991) 1385.

[Spr96] C. Springer, M. Head-Gordon. *Simulations of the femtosecond laser-induced desorption of CO from Cu (100) at 0.5 ML coverage*. Chem. Phys. **205**, (1996) 73.

[Sti99] F. Stietz, and F. Traeger. *Surface plasmons in nanoclusters: elementary electronic excitations and thier applications.* Philosophical Magazine B 79, (1999) 1281.

[Sti00] F. Stietz, J. Bosbach, T. Wenzel, T. Vartanyan, A. Goldmann, and F. Traeger. *Decay times of surface plasmon excitation in metal nanoparticles by persistent spectral hole burning*. Phys. Rev. Lett. **84**, (2000) 5644.

[Str96] L. M. Struck, L. J. Richter, S. A. Buntin, R. R. Cavanagh, and J. C. Stephenson. *Femtosecond laser-induced desorption of CO from Cu (100): Comparison of theory and experiment*. Phys. Rev. Letts. **77**, (1996) 4576.

[Tig93] J. Tiggesbaeumker, L. Koeller, K.-H. Meiwes-Broer, and A. Liebsch. *Blue shift of the Mie plasma frequency in Ag clusters and particles.* Phys. Rev. A **48**, (1993) R1749.

[Val98] M. Valden, X. Lai, and D. W. Goodman. *Onset of catalytic activity of gold clusters on titania with the appearance of nonmetallic properties*. Science **281**, (1998) 1647.

[Vij02] V. Vijayakrishna, A. Chainani, D. D. Sarma, and C. N. R. Rao. *Metal-insulator transitions in metal clusters: a high-energy spectroscopy study of palladium and silver clusters.* J. Phys. Chem. **96**, (1992) 8679.

[Voi00] C. Voisin, D. Christofilos, N. Del Fatti, F. Valle’e, B. Pre’vel, E. Cottancin, J. Lerme’, M. Pellarin, and M. Broyer. *Size-dependent electron-electron interactions in metal nanoparticles.* Phys. Rev. Letts. **85**, (2000) 2200.

[Voi01] C. Voisin, D. Christofilos, N. Del Fatti, and F. Valle'e. *Femtosecond surface plasmon resonance dynamics and electron-electron interactions in silver nanoparticles.* Eur. Phys. J. D **16,** (2001) 139.

[Voi04] C. Voisin, D. Christofilos, P. A. Loukakos, N. Del Fatti, F. Valle'e, J. Lerme', M. Gaudry, E. Cottancin, M. Pellarin, and M. Broyer. *Ultrafast electron-electron scattering and energy exchanges in noble-metal nanoparticles*. Phys. Rev. B **69**, (2004) 195416.

[Wat96] K. Watanabe, K. Sawabe, and Y. Matsumoto. *Adsorbate-localized excitation in surface photochemistry: Methane on Pt (111)*. Phys. Rev. Letts. **76**, (1996) 1751.

[Wat99] K. Watanabe, Y. Matsumoto, M. Kampling, K. Al-Shamery, and H.-J. Freund. *Photochemistry of methane on Pd/Al_2O_3 model catalyst: Control of photochemistry on transition metal surfaces.* Angew. Chem. Int. Ed. **38**, (1999) 2192.

[Wat06] K. Watanabe, D. Menzel, N. Nilius, and H.-J. Freund. *Photochemistry on metal nanoparticles*. Chem. Rev. **106**, (2006) 4301.

[Wat07] K Watanabe, K.H. Kim, D. Menzel, and H.-J. Freund. *Hyperthermal chaotic photodesorption of Xe from alumina-supported Ag NPs: plasmonic coupling and plasmon-induced desorption*. Phys. Rev. Letts. **99**, (2007) 225501.

[Wei93] F. Weik, A. de Meijere, and E. Hasselbrink. *Wavelength dependence of the photochemistry of O_2 on Pd (111) and the role of cascades*. J. Chem. Phys. **99** (1993) 682.

[Wer89] G. K. Wertheim. *Electronic structure of metal clusters*. Z. Phys. D **12**, (1989) 319.

[Wet05] K. Wettergren, B. Kasemo, and D. Chakarov. *Photodesorption of NO from graphite (0001) surface mediated by silver clusters*. Surf. Sci. **593**, (2005) 235.

[Wil99] M. Wilde, O. Seiferth, K. Al-Scamery, and H.-J. Freund. *Ultraviolet-laser induced desorption of NO from the Cr_2O_3(0001) surface: Involvement of a precursor state?* J. Chem. Phys. **111**, (1999) 1158.

[Yin90] Z. C. Yin, and W. Ho. *Thermoinduced and photoinduced reactions of NO on Si (111)7x7. III. Photoreaction mechanisms*. J. Chem. Phys. **93**, (1990) 9089.

[Yin91] Z. C. Ying, and W. Ho. *Photodissociation of adsorbed $Mo(CO)_6$ induced by direct photoexcitation and hot electron attachement. II. Physical mechanisms*. J. Chem. Phys. **94,** (1991) 5701.

[Yud08] I. V. Yudanov, M. Metzner, A. Genest, and N. Roesch. *Size-dependence of adsorption properties of metal nanoparticles: A density functional study on palladium nanoparticles*. J. Phys. Chem. C **112**, (2008) 20269.

[Zha07] Z. Zhang, Q. Fu, H. Zhang, Y. Li, Y. Yao, D. Tan, and X. Bao. *Enhanced methanol dissociation on nanostructured 2D Al overlayer*. J. Phys. Chem. C **111**, (2007) 13524.

[Zhd04] V. P. Zhdanov, and B. Kasemo. *Specifics of substrate-mediated photo-induced chemical processes on supported nm-sized metal particles*. J. Phys.: Condens. Matter **16**, (2004) 7131.

[Zhd07] V. P. Zhdanov, and B. Kasemo. *Efficiency of the plasmon-mediated enhancement of photoexcitation of adsorbate on nm-sized metal particles*. Chem. Phys. Letts. **443**, (2007) 132.

[Zho91] X.-L. Zhou, X.-Y. Zhu, and J. M. White. *Photochemistry at adsorbate/metal interfaces.* Surf. Sci. Rep. **13**, (1991) 73.

[Zim94] F. M. Zimmermann, and W. Ho. *Velocity distributions of photochemically desorbed molecules.* J. Chem. Phys. **100**, (1994) 7700.

[Zim94^a] F. M. Zimmermann, and W. Ho. *Rotational and spin-orbit distributions of photochemically desorbed molecules*. Phys. Rev. Letts. **72**, (1994) 1295.

[Zim94^b] F. M. Zimmermann, and W. Ho. *Rotational-Translational correlations in photochemically desorbed molecules*. J. Chem. Phys. **101**, (1994) 5313.

[Zim95] F. M. Zimmermann, and W. Ho. *State resolved studies of photochemical dynamics at surfaces*. Surf. Sci. Rep. **22,** (1995) 127.

[Zim97] F. M. Zimmermann. *Vibrational excitation dynamics in photodesorption*. Surf. Sci. **390**, (1997) 174.

Publications

- Daniel Mulugeta, Ki Hyun Kim, Kazuo Watanabe, Dietrich Menzel, Hans-Joachim Freund. *Size Effects in Thermal and Photochemistry of* $(NO)_2$ *on Ag Nanoparticles*. Phys. Rev. Lett. **101**, (2008) 146103.

In preparation:

- Daniel Mulugeta, Kazuo Watanabe, Dietrich Menzel, Hans-Joachim Freund. *State-resolved investigation of the photodesorption dynamics of NO from* $(NO)_2$ *on Ag (111) surface.* In preparation.
- Daniel Mulugeta, Kazuo Watanabe, Dietrich Menzel, Hans-Joachim Freund. *Particle size dependent desorption dynamics of NO from alumina supported Ag nanoparticles*. In preparation

Acknowledgments

I would like to express my sincere gratitude to Prof. Dr. Hans-Joachim Freund for giving me this wonderful opportunity to work in his group under his supervision and for helping me grow up. I thank him for his patience, kindness and generosity.

I would like to convey my deepest appreciation to Prof. Kazuo Watanabe for both his scientific and personal guidance. His dedication towards research, encouragement and support is unmatched and I have been grateful to be part of his research group. His guidance, friendship, and willingness to help are invaluable and deeply appreciated. He has demonstrated to me the type of researcher I hope to become.

This thesis would certainly have been inconceivable without the direction and assistance of Prof. Dr. Dietrich Menzel. Specially, Prof. Dr. Menzel is thanked for his guidance in the write-up of this thesis and providing helpful feedback. He has never hesitated to offer explanations and generous advice. He always made me think independently and offered help in every possible way when needed. He has always come with extremely splendid ideas and been so fast to respond (even during weekends and holydays) whenever I had troubles and needed suggestions. The many suggestions he made helped to steer me in the right direction. I cannot express enough thanks for his contribution to this document.

I would like to thank Prof. Dr. Martin Wolf for serving as my second supervisor. Additionally, I thank him for giving me the opportunity to present and discuss the results of my work with him and his group members. I have benefited from the many fruitful discussions.

I would like also thank my colleagues Walter Wachsmann and Dr. Ki Hyun Kim for their active cooperation. Specially, Walter Wachsmann is thanked for helping me in sample preparations and on time liquid Helium ordering and delivering.

I would like to express my deep gratefulness to all those who have helped, encouraged, and supported me during my stay at FHI. I must make particular mention of my gratitude to Georg Simon, Dr. Matthew Brown, Klaus Peter Vogelgesang for their kindness and friendly approach. Specially, I thank George for translating my English abstract to German and for his fruitful discussion about alumina film on a NiAl substrate.

I would like to thank Dr. Rau Eva-Maria and Aleme Beyene for their help since the first day I arrived in Germany. I can not thank enough for their support throughout my studies.

Finally, I would like to extend my warmest appreciation to my parents and friends for their encouragement. Above all, I am grateful to my friend, Sarah, for her constant love, *challenge*, care and above all her *patience*.

Curriculum Vitea

For reasons of data protection, the Curriculum vitae is not published in the online version